DC Fault-ride-through Analysis of Multi-terminal DC systems considering Grid-following and Grid-forming Converter Control

PhD Thesis

Jesús Horacio Castellanos Aguirre

Power Electronics Drives & Energy Conversion (PEDEC)

Electronic & Electrical Engineering

University of Strathclyde, Glasgow

September 26, 2026

This thesis is the result of the author's original research. It has been composed by the author and has not been previously submitted for examination which has led to the award of a degree.

The copyright of this thesis belongs to the author under the terms of the United Kingdom Copyright Acts as qualified by University of Strathclyde Regulation 3.50. Due acknowledgement must always be made of the use of any material contained in, or derived from, this thesis.

Abstract

The accelerating global transition toward sustainable energy is driving a rapid structural shift in power networks, replacing conventional synchronous generation with power electronics-interfaced resources. High-Voltage Direct Current (HVDC) systems, particularly those using Modular Multilevel Converters (MMCs), have emerged as a key solution for long-distance bulk power transmission and the integration of large-scale offshore wind farms (OWFs). As these infrastructures evolve from simple point-to-point topologies into complex Multi-Terminal DC (MTDC) networks, maintaining operational stability, under resilience and reliability (R&R) principles, during severe direct current contingencies represents a critical engineering challenge.

This thesis presents a comprehensive investigation into the DC Fault Ride-Through (FRT) performance of meshed MTDC networks. To address these complexities, an exemplary minimum-meshed bipolar MMC-MTDC grid is used. This MTDC grid architecture integrates offshore wind generation while interconnecting two asynchronous bulk AC power systems. Utilizing detailed Electromagnetic Transient (EMT)-type simulations, this work identifies, characterizes, and mitigates the complex transient phenomena and cross-layer control interactions that manifest across distinct stages of the DC FRT sequence. The core of the analysis evaluates the interdependencies between two primary converter control paradigms - GFL and GFM control strategies — and fundamental DC grid protection philosophies, with a specific emphasis on non-selective and partially selective schemes.

Under a non-selective protection strategy, where a fault causes a temporary system-wide shutdown and converter blocking, the thesis characterizes system behavior under low voltage stiffness conditions with a Short Circuit Ratio of 1.5. It evaluates and com-

pares two distinct recovery strategies: a joint Vdc-P droop control and a single-station temporary Vdc-master controller. The analysis reveals a critical control interaction mechanism between the MMC control loops during restoration, for which an a decoupling mechanism is proposed as a solution to the identified issues. Following, the integration of GFM control is investigated via the Virtual Synchronous Machine (VSM) approach featuring an outer Vdc-P droop layer. This configuration exposes a fundamental control conflict when an MMC must simultaneously deliver inertial support to the AC network and voltage regulation to the DC grid. A perturbation propagation mechanism is identified and characterized. A decoupling mitigation strategy is implemented, successfully enabling the safe operation of GFM as the sole paradigm regulating the MTDC network voltage.

Transitioning to a partially selective philosophy, the DC network is segmented into distinct fault separation zones using DC reactors (DCRs) and circuit breakers. This thesis develops a generic open-loop Control and Protection (C&P) coordination sequence that accounts for the electrical interdependencies of line inductors sizing and converter continuous operation. The work systematically maps typical transient phenomena and uncovers detrimental control loop interactions that jeopardize stability when converters operate in GFL and GFM control modes. Finally, it proposes a fundamental mitigation solution to decouple conflicting AC and DC power dynamics of the MMC originating from the control architecture designed to provide AC and DC grid services.

The outcomes of this research contribute to a clearer technical roadmap and design framework for achieving stable, secure, and resilient fault ride-through operation in future hybrid AC/DC power systems.

Contents

Abstract **ii**

List of Figures **vii**

List of Abbreviations **xii**

List of Symbols **xv**

Acknowledgements **xvii**

1 Introduction **1**

1.1 Project background 1

1.2 Modern power systems 5

1.2.1 Transmission and generation 6

1.2.2 Dynamic loads and storage 6

1.3 MTDC systems control and protection challenges 7

1.4 Research Challenges, Gaps and Objectives 8

1.4.1 Research Questions, Objectives of the Thesis and Scientific Contributions 9

1.5 Outline of the work 11

1.6 List of Publications 12

1.7 Contributions to project deliverables 13

2 AC/DC hybrid system model and hypothesis of work **15**

2.1 Chapter introduction 15

2.2 The AC/DC hybrid system 16
2.2.1 The AC/DC hybrid system architecture 16
2.2.2 AC and DC grids' services 18
2.3 MMC characteristics 20
2.3.1 MMC physical arrangement 20
2.3.2 Arm averaged-value model 22
2.4 MMC control and protection 23
2.4.1 MMCs' control philosophy 23
2.4.2 MMC control architecture and control strategies 26
2.4.3 MMC internal protection 31
2.5 MTDC protection 33
2.5.1 DC faults 34
2.5.2 DC switching devices 35
2.5.3 DC protection philosophies 36
2.5.4 Generic DC protection sequence along system DC FRT 40
2.6 Summary 43

3 DC FRT considering non-selective protection strategy 45
3.1 Chapter introduction 45
3.2 System DC FRT with GFL control 45
3.2.1 HVDC system under consideration 46
3.2.2 Study methodology 47
3.2.3 Reference scenario 50
3.3 Interconnection to a weak AC grid and the MTDC grid re-energization . 56
3.3.1 Re-energization strategies 58
3.3.2 Re-energization strategies comparison 60
3.3.3 Smooth re-energization with a Vdc-master controller 63
3.4 Introduction to the GFM response 67
3.4.1 Expected voltage source dynamic behavior 67
3.4.2 MMC AC side response under DC FRT 68
3.5 Summary 72

4 MTDC voltage regulation by VSM-based GFM control 75

4.1 Chapter introduction . . . 75

4.2 GFM in Vdc-P droop mode integration analysis . . . 76

4.2.1 Control architecture analysis . . . 76

4.2.2 Study methodology . . . 78

4.3 Simulation model . . . 78

4.4 DC FRT with GFL & GFM . . . 80

4.4.1 Fault clearing . . . 80

4.4.2 Restoration process . . . 83

4.4.3 Perturbation propagation mechanism . . . 85

4.5 DC FRT with GFM in Vdc-P droop as the sole strategy regulating DC voltage . . . 88

4.5.1 Fault clearing . . . 89

4.5.2 Restoration process . . . 90

4.5.3 Comparison of applying a short temporary stop for the three cases 91

4.5.4 Use of one AC system to regulate the MTDC grid energy . . . 97

4.6 Summary . . . 103

5 DC FRT with partially selective protection 106

5.1 Chapter introduction . . . 106

5.2 Implementation of the partially selective protection strategy . . . 107

5.2.1 Main protection parameters interdependencies . . . 109

5.2.2 DCRs sizing . . . 110

5.2.3 DC FRT C&P coordination . . . 115

5.3 Reference case scenario – GFL control . . . 118

5.4 Integration of GFM control with a partially selective protection . . . 122

5.4.1 GFM control only in station S_1 . . . 122

5.4.2 GFM oscillatory behaviour . . . 124

5.4.3 GFM control in both stations S1 and S2 . . . 125

5.5 Summary . . . 129

6 Concluding remarks and perspective **132**

6.1 Conclusions 132

6.2 Future work 135

A Appendix A: VSM characteristic equation derivation **137**

A.0.1 Setting P_{ac}^{*} equal to zero 137

A.0.2 Setting $\tilde{\omega}_g$ equal to zero 140

References **144**

List of Figures

1.1 AC-DC system for OWF grid access - schematic [14] 2
1.2 HVDC PLUS® MMC technology - valve hall [15] 3
1.3 Exemplary MTDC system integration in bulk AC system [22] 4
1.4 European power systems' evolution [24] 5

2.1 AC-DC system single line diagram 17
2.2 MMC representation with simplified submodules. 21
2.3 MMC with averaged value model arm representation. 22
2.4 MMC cascaded control architecture. 27
2.5 Phase-Locked Loop (PLL) block diagram [53, 81]. 28
2.6 Phase-Locked Loop (PLL) operation example. 28
2.7 GFL cascaded control architecture. 29
2.8 GFM cascaded control architecture. 30
2.9 VSM AC power control block diagram [88]. 30
2.10 Virtual impedance current limiter implementation [82]. 32
2.11 Fault current interruption process and timings [34] 37
2.12 DCCB based non-selective protection strategy single line diagram 38
2.13 Partially selective protection strategy single line diagram 39
2.14 Fully selective protection strategy single line diagram 40
2.15 Resilience trapezoid: conceptual phases related to resilience of a power system [116]. 41
2.16 DC FRT flow diagram. 42
2.17 DC FRT flow diagram. 43

List of Figures

3.1 AC-DC system single line diagram with a DCCB-based non-selective protection scheme 46
3.2 DC FRT C&P generic sequence with a DCCB-based non-selective protection strategy. 48
3.3 MMC GFL control architecture, where the dedicated control to perform the DC FRT is highlighted. 49
3.4 Dedicated de-blocking energy control - detailed view. 49
3.5 Dedicated de-blocking voltage control - detailed view. 50
3.6 MTDC system faulty pole DC voltage profiles measured at the converter terminals- reference case 51
3.7 MTDC system fault transient DC voltage and active power profiles - reference case 51
3.8 MTDC healthy pole active power profiles - reference case 53
3.9 MTDC faulty pole internal energy profiles - reference case 54
3.10 MTDC healthy pole reactive power profiles and AC voltage amplitude at the PoC- reference case 55
3.11 MTDC healthy pole reactive power profiles and AC voltage amplitude at the PoC- reference case zoom-in 56
3.12 GFL AC cascading control loop and reconfiguration during DC-FRT operation. 58
3.13 GFL DC cascading control loop and reconfiguration during DC-FRT operation. 59
3.14 PoC Vac magnitude, S_2 faulty pole DC voltage and active power profiles - re-energization strategies comparison 61
3.15 S_2 faulty pole DC voltage, internal energy, active power and PoC AC voltage amplitude 65
3.16 MMC control interaction mechanism and perturbation propagation. . . 65
3.17 Internal energy control PI coefficients management during restoration process. 66
3.18 S_2 faulty pole DC voltage and internal energy with proposed solution . 66

3.19 S_2 faulty pole DC voltage profiles - GFM introduction 70
3.20 S_2 healthy pole active and reactive power profiles - GFM introduction . 71

4.1 MMC GFM control architecture, where the dedicated control to perform the DC FRT is highlighted. 77
4.2 GFM integration as the sole strategy regulating the MTDC voltage . . . 78
4.3 MTDC faulty and healthy poles Vdc profiles - with GFL & GFM 81
4.4 MTDC faulty and healthy poles Vdc profiles - with GFL & GFM 82
4.5 MTDC faulty and healthy poles Vdc profiles - with GFL & GFM 84
4.6 S_1 healthy pole in GFM during fault transient 86
4.7 S_2 healthy pole in GFL during fault transient 86
4.8 Control interaction and perturbation propagation mechanism with GFM and GFL 88
4.9 S1 and S2 fault transient detailed view - only with GFM 89
4.10 S1 and S2 restoration detailed view - only with GFM 91
4.11 First and second scenarios comparison - same C&P sequence 92
4.12 Switching from GFL strategy to GFM 93
4.13 Scenario 1 alternative restorations for a short temporary stop 94
4.14 Scenario 1 alternative restorations for a short temporary stop 96
4.15 Control interaction and perturbation propagation mechanism with GFM and AC side internal energy regulation 99
4.16 MMC GFM control architecture, where the dedicated control to perform the DC FRT is highlighted. 100
4.17 Perturbation propagation 101
4.18 Faulty pole DC voltage, active power and internal energy profiles 102

5.1 MTDC system single line diagram with partially selective segmentation 108
5.2 Interdepence between system-level protection parameters considering MMC continuous operation [99] 110
5.3 DCRs sizing methodology 111
5.4 Fault test at FSZ1 112

5.5 Fault test at FSZ2 . . . 113
5.6 Fault test at FSZ3 A . . . 114
5.7 Fault test at FSZ3 B . . . 114
5.8 DC FRT C&P sequence for a fault in FDZ3 . . . 119
5.9 Fault current neutralization in FSZ 3 . . . 119
5.10 Offshore DC FRT overview . . . 121
5.11 MTDC Vdc & Pac . . . 121
5.12 Positive pole MTDC Vdc & Pac for different energy control rise times. a) $t_r = 800$ ms b) $t_r = 200$ ms, c) $t_r = 130$ ms and d) $t_r = 30$ ms . . . 123
5.13 MTDC Vdc & Pac with 1 station in GFM and low damping . . . 124
5.14 MTDC Vdc & Pac with 1 station in GFM and proper damping . . . 125
5.15 S_1 and S_2 (+) pole Pac & Pdc with both stations in GFM and different damping coefficients . . . 126
5.16 MTDC Vdc & Pac with 2 stations in GFM . . . 128

A.1 P^*_{ac} set to zero - Step 1 . . . 138
A.2 P^*_{ac} set to zero - Step 2 . . . 138
A.3 P^*_{ac} set to zero - Step 3 . . . 138
A.4 P^*_{ac} set to zero - Step 4 . . . 139
A.5 P^*_{ac} set to zero - Step 5 . . . 139
A.6 $\tilde{\omega}_g$ set to zero - Step 1 . . . 140
A.7 $\tilde{\omega}_g$ set to zero - Step 2 . . . 140
A.8 $\tilde{\omega}_g$ set to zero - Step 2.1 . . . 140
A.9 $\tilde{\omega}_g$ set to zero - Step 3 . . . 141

List of Abbreviations

ACCB	AC Circuit Breaker
AVM	Averaged-Value Model
C&P	Control and Protection
CAPEX	Capital Expenditure
CSA	Current Saturation Algorithm
DBS	Dynamic Braking System
DCCB	DC Circuit Breaker
DCR	DC Reactor
DD	Dedicated De-blocking
DDEC	Dedicated De-blocking Energy Controller
DDVC	Dedicated De-blocking DC Voltage Control
DMR	Dedicated Metallic Return
DP	Dynamic Phasors
EM	Electromagnetic
EMT	Electromagnetic Transient
FCR	Frequency Containment Reserves
FRR	Frequency Restoration Reserves
FRT	Fault Ride-Through
FSD	Fault Suppression Device

List of Abbreviations

FSZ	Fault Separation Zone
GFL	Grid-Following
GFM	Grid-Forming
HBSM	Half-Bridge Submodule
HPFF	High-Pressure Fluid-Filled
HPOF	High-Pressure Oil-Filled
HVDC	High-Voltage Direct Current
IBR	Inverter-Based Resource
IGBT	Insulated-Gate Bipolar Transistor
IR	Inertial Response
LVRT	Low Voltage Ride-Through
MMC	Modular Multilevel Converter
MRTB	Metallic Return Transfer Breaker
MTDC	Multi-Terminal Direct Current
OPEX	Operational Expenditure
OWF	Offshore Wind Farm
PCC	Point of Common Coupling
PDT	Phasor Domain Transient
PLL	Phase-Locked Loop
PoC	Point of Connection
POD	Power Oscillation Damping
PPM	Power Park Module
R&R	Resilience and Reliability

List of Abbreviations

RCS	Residual Current Switch
RES	Renewable Energy Sources
RMS	Root Mean Square
RoCoF	Rate of Change of Frequency
SCFF	Self-Contained Fluid-Filled
SCOF	Self-Contained Oil-Filled
TIV	Transient Interruption Voltage
TSO	Transmission System Operator
UFLS	Under-Frequency Load Shedding
VSC	Voltage Source Converter
VSM	Virtual Synchronous Machine
XLPE	Cross-Linked Polyethylene

List of Symbols

C_{eq}^{vc}	Equivalent capacitance for virtual capacitor control
C_{Σ}^{Wtot}	Aggregated capacitance (DC grid + virtual capacitor)
$G_{idc}(s)$	Transfer function of inner current control (DC side)
$G_{ig,dq}(s)$	Transfer function of inner current control (AC side)
H	Inertia constant of VSM (s)
I_{AC}, I_{DC}	AC and DC components of arm current
I_{arm}	Arm current (p.u.)
k_d	Damping coefficient of VSM
k_p^{Wtot}, k_i^{Wtot}	Proportional and integral gains of energy controller
k_{vc}	Virtual capacitor coefficient
m_v	Voltage droop coefficient
P_{ac}	Measured active power at converter AC side (p.u.)
P_{ac}^*	Active power reference
Q	Measured reactive power (p.u.)
Q^*	Reactive power reference
SCR	Short Circuit Ratio
t_r	Rise time (s)
v_{abc}^{Δ}	Difference voltage reference (AC control)
v_{abc}^{Σ}	Sum voltage reference (DC control)
v_{Δ}	Modulated converter AC voltage (p.u.)
$V_{d,drop}^*$	AC voltage reference with droop
$V_{dc}^{n,u}$, $V_{dc}^{n,l}$	Upper and lower arm voltages of phase n (p.u.)

V_{dc}^{*}	Nominal DC voltage reference
V_g	Voltage at converter PoC (p.u.)
$\tilde{\omega}_g$	Grid frequency estimated by PLL (rad/s)
ω_{vsm}	Computed frequency by VSM (rad/s)
ω_{vsm0}	Nominal VSM frequency (rad/s)
W_{tot}	Total internal energy of MMC (p.u.)
W_{tot}^{n}	Total internal energy of leg n (p.u.)
W_{vc}^{*}	Virtual capacitor energy reference
X_{eq}	Equivalent impedance between PoC and submodules
$Z_{virtual}$	Virtual impedance for current limiting

Acknowledgements

I would like to acknowledge Professor Lie Xu. Without his support, as of the first month of the industrial PhD endeavour, almost three years ago, this work would never have seen the light of day. It was a true honor and privilege to work with you, Lie, and, at the same time, a lucky strike. Despite the remote supervision and the near-complete absence of simulation models review, your experienced and knowledgeable vision helped me gain fundamental understanding of my work and the purpose of the research project. As well, I would like to thank the entire PEDEC team, and in particular, Agustí Egea, Oswing Ashwood, Ning Yang, and Irene Masenge, as well as professors and staff members of the University of Strathclyde, including Olimpo Anaya Lara, David Campos Gaona, Elaine Black, Sarah Doherty, Michelle Maclean, Paul Murray, and Fiona Edler.

I would also like to thank Hubert De La Grandiere for his trust in me to deliver this thesis, and for the opportunity to be part of one of the most modern and innovative organizations in the world, SuperGrid Institute—one of the seven French Institutes for Energy Transition (ITE) based in Villeurbanne, a growing player in the energy transition, and a collaborator of society in 'La Métropole de Lyon'. To the leader of the Supergrid Architecture and Systems programme, Jean-Baptiste Heyberger - despite your arrival during the second year of the industrial PhD - a big thank you for changing the dynamics, helping us to improve and make the most of our work. Important thanks to Abdelkrim Benchaib for being my manager during this period, and being there from the first interview to the very last day. Thanks also to all the programme colleagues: Ahmed Zama, for bringing technical rigour to the studies, analyses and delineating further development lines; thanks to Filipe Perez, despite all the delays to

progress with the thesis and main studies, your coordination in the project, tips to use Microsoft apps and discounts have been quite helpful; to Kosei Shinoda, for always providing interesting perspectives and nice scientific references; Boussaad Ismail, for bringing a laugh in every encounter, and sharing time to enjoy; Baptieste Perreyon, for your kindness and good spirit; Lucas Molina, irmão; Hind Bekkouri and Gianni Bakhos, for the coffees and welcoming; Seddik Bacha for encouraging me to move towards my destination, Nicolas Barla for those very nice discussions on politics, Daniel Gomez, parce, Valentin Mathieu. Another very big thanks to Eric Courbon for all your IT support along the PhD.

A very important thanks to all outside daily work within the company: Georges Bustos, Claire Billaz, Audreay Dieudonne, for those incredible randonées; Audrey Casas, Samuel Tiercelin, Mamadou Djan, Anotine Perez, Philip Fabre, Nadine Majeri, Isabelle Najarre, Clarisse Martin, Vincent Liebart, Amjad Mouhaidali, Victor Petit, Titouan Abiad, Minh-Phong, Piotr Dworakowski, Jing Dai, Damien Decq, Adriana Campos, Charles Sarra, Gwénaël Marquezin, Vincent Léger, Lucie Goulmont, Sandra Dias Cascail and Perrine Bougenet.

An outstanding thanks to all the football team players: Loïc Leclere, José Aguilar, Benhur Zolett, Maxim Oliva, Mor Diop, Sidlawende Ouoba, Sanjiv Kumar, Zakarya Abdesselam, Florian Lesage, Edouard Bonnin, et encore Jean-Baptiste.

A special thanks to all the participants in the HVDC-wise project, but in particular Florent Morel, Karim Karoiui, Ben Marshall, Idun Deildokk, Mathaios Panteli, Colin Foote, Alex Stefanov, Keith Bell, Callum Henderson, Sarah Anhaus, Murial Krüger, Peter Jan Randewijk, Robert Dimitrovski, Lars Osterkamp, Willem Leterme and Paul McNamara.

Another special thanks to the GE Vernova colleagues with whom I took -really helpful- weekly yoga sessions: Marcus Schober, Solène Laurent, Celine Boulot, Julien Beauchet, Sandrine Bregeon, Julian Dampne, Nicolas Lamboray, Nicolas Magnan, Hugo Marchal, Jose Isaac, Thierry Martinez, Giusepe Natale, Valery Pennecot.

Thanks to all CIGRE NGN colleagues with whom nice collaborations were possible: Matthieu Dalstein, Marine Moyroud, Camille Berdou, Pierre Courdereau, El-Mehdi

Karmani, Alexia Venet, Ibtissem Sidhoum, Sameh Betamony. And CIGRE members: Philippe Lienhart, Philippe Adam, Paul Leemans, Li Yang, Jonathan Roulot, Enrico Carlini, Mark Waldrin, Javier Iglesias, Dechao Kong, Sébastien Dennetière and John Stuart Finn.

This contribution to public knowledge has been built on the shoulders of giants; therefore, I would like to express my gratitude to the professors and mentors who gave me a hand and provided the foundation for further progress in my research endeavours, whether in a classroom, office, laboratory, garden, carpool, or through their published work: Lie Xu, Hubert De La Grandiere, Jean-Baptiste Heyberger, Dirk Van Hertem, Xavier Guillaud, Geraint Chaffey, Willem Leterme, Gilles Chaspiere, Fortunato Villella, Didier Wiot, Peter Van Meirhaeghe, Markus Berger, Luiggi Vanfretti, William D'haeseleer, Manuel Barragan-Villarejo, Jose Maria Maza, Juan Manuel Mauricio, Thibault Prevost, Oriol Gomis-Bellmunt, Francisco Gonzalez-Longatt, Ruth Vazquez Sabariego, Geert Deconinck, Johan Driesen, Jef Beerten, Koenraad Van Reusel, Lieve Helsen, Federico Méndez Lavielle, Eva Adnan Kanso, Marco Antonio Reyes Huesca, Francisco Solorio, Rick Loenders, Mian Wang, Simon Nagels, Hakan Ergun, Mudar Abedrabbo, among others.

My most special thank you: to my grandmother, Maria Teresa Morales Hernandez. Thanks to my family, Rita Aguirre Morales, Octavio and Francisco Castellanos Aguirre, Juan Francisco Castellanos Romero. Pepe, Ricardo, Javier, Reina, Ramón, Abel, Martín, Fidel and Arturo Aguirre Morales. Julio, Arturo, Teresa and Sara Luz Castellanos Romero. To Alitzel Bruno Solís for being there and making every moment a dream. To my friends Joel Wiki Macias, Victor Wektor Sierra, Francisco Pinto, Flor Elena Rivera, Vincent Lechappe, Cas Bex, Sayed Sadegh Mousavi, and those with whom I remain in contact.

Chapter 1

Introduction

1.1 Project background

Global climate and energy challenges are currently accelerating the energy transition on a worldwide scale [1], [2], [3], [4], [5], [6], [7], [8], [9], [10]. When navigating national policy decisions, the "energy trilemma", i.e., balancing the integration of cleaner energy sources, security of supply, and affordability, remains a primary focal point. As a leading region in the world, the European Union has set targets to reach climate-neutrality by 2050, outlined in the European Green Deal, and formalized in the European Climate Law. Most urgent milestone is the intermediate target of a 55% reduction of greenhouse gas emissions by 2030, followed by a 90% by 2040, with respect to 1990 levels[11], [12].

To this end, power systems development and renewable energy sources (RES) are becoming core instruments in the energy transition. Reducing dependence on fossil fuels, particularly oil and gas, has made the development and integration of these assets a strategic priority. For European nations with coastlines, offshore wind power has become a cornerstone solution, e.g., the UK [13] or Germany [14], providing a clean, cost-effective, and reliable energy source, by giving grid access to OWFs as depicted in Figure 1.1 [4], [5], [6].

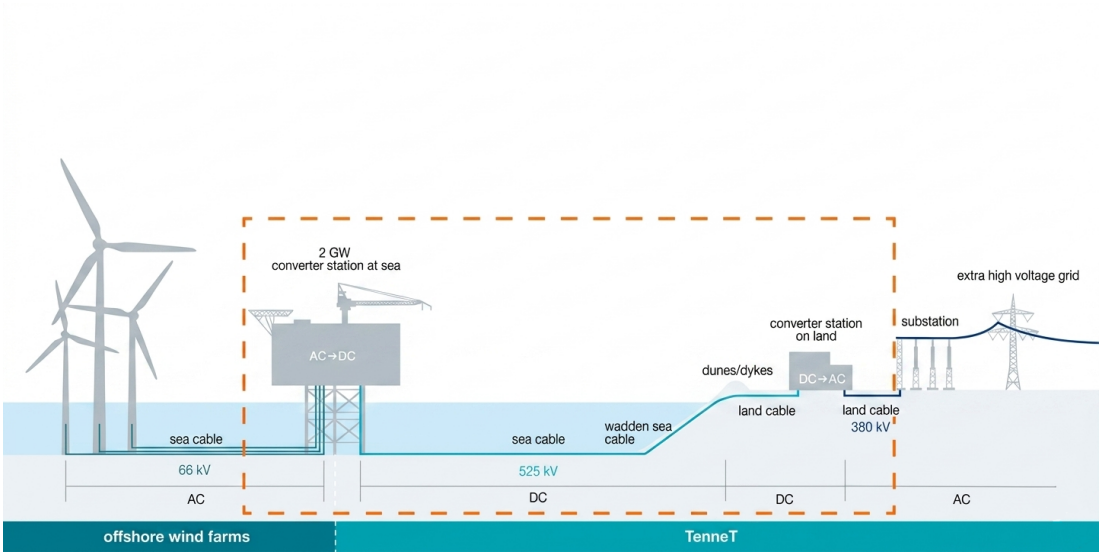


Figure 1.1: AC-DC system for OWF grid access - schematic [14]

To support this transition, Voltage Sourced Converter-based High Voltage Direct Current (VSC-HVDC) systems have emerged as the premier solution for reinforcing and developing bulk AC systems, an exemplary valve hall of a VSC-HVDC system is depicted in Figure 1.2 [15]. These systems are uniquely suited for high-capacity and efficient, long-distance transmission via both overhead lines and subsea cables, with reduced electromagnetic (EM) field issues [16], [17].

Technically, VSC-HVDC systems offer superior performance through the independent and rapid controllability of active and reactive power. This capability facilitates the interconnection of asynchronous grids and enables essential AC system services, including frequency control, Power Oscillation Damping (POD), and dynamic voltage support [18]. Therefore, VSC-HVDC systems enhance overall system stability while needing a reduced geographic right-of-way and compact footprint of their converter stations.

Beyond stability advantages, the interconnection of disparate bidding zones, power systems, and control areas is increasingly important for society [19], [20]. These interconnections drive social welfare by fostering robust power trade and reducing grid congestion, ultimately ensuring that energy remains affordable and efficiently distributed across borders.



Figure 1.2: HVDC PLUS® MMC technology - valve hall [15]

In this context, public funding, channeled through the European Union's Horizon Europe program under agreement 101075424 and the UK Research and Innovation (UKRI) funding under the UK government's Horizon Europe funding guarantee [grant numbers 10041877 and 10051113], the HVDC-wise project was established. A collaborative initiative involving Transmission System Operators (TSOs), universities, and research institutes across the United Kingdom and the European Union, coordinated by SuperGrid Institute [21]. The project is dedicated to deepening the collective understanding of the technical challenges and operational implications associated with integrating Multi-Terminal HVDC (MTDC) systems within, and as interconnections between, bulk AC power grids, for both power exchange and offshore wind power integration, as shown with a conceptual illustration in Figure 1.3 [22].

The primary objective of this project is the development of tools and methodologies required to successfully deploy MTDC grids. To ensure a comprehensive evaluation, the project's research scope encompasses several critical layers of analysis:

- Static Studies: focusing on techno-economic feasibility and system adequacy
- Dynamic Studies: utilizing Phasor Domain transient (PDT) or Root Mean Square

(RMS), dynamic phasors (DP), and Electromagnetic Transient (EMT) simulations to assess system behavior under various conditions

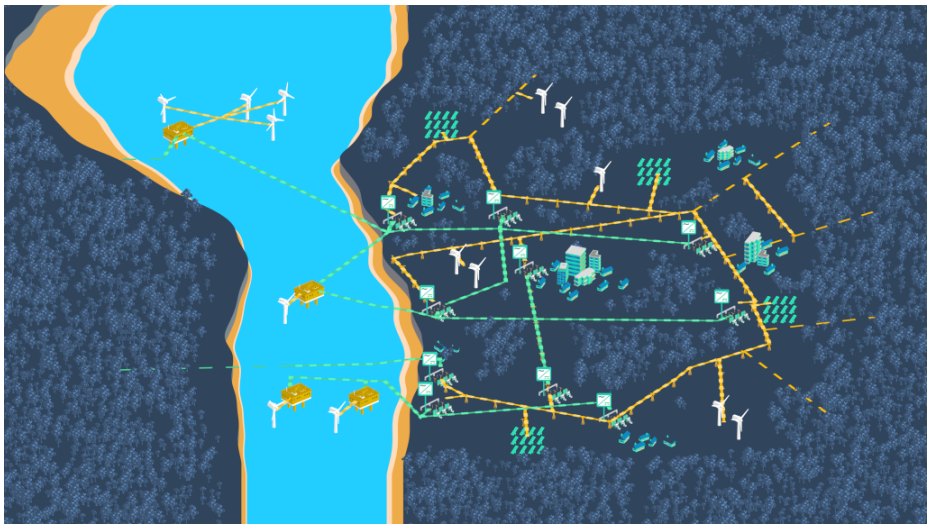


Figure 1.3: Exemplary MTDC system integration in bulk AC system [22]

This thesis provides a contribution to the domain of EMT-type studies by investigating the impact of a large disturbance: a DC fault within an MTDC network. Although simplified, the system under analysis represents a hybrid AC/DC power system architecture that integrates large-scale offshore wind generation while facilitating the interconnection of two asynchronous bulk AC systems. Having several layers of complexity, the analysis requires proper handling of the system modelling to identify and address characteristic phenomena along the system operation throughout the DC FRT.

The research involves a comprehensive revision of system-wide behavior under two primary control paradigms, namely, grid-following (GFL) and grid-forming (GFM), in conjunction with fundamental protection philosophies, giving emphasis to the non-selective and partially selective philosophies. A central objective of this work is to identify and characterize "typical" transient phenomena that manifest across the entire system during each distinct stage of the DC Fault Ride-Through (FRT) process and their implication at MMC and system-level.

Furthermore, the study analyzes how coordinated control and protection (C&P)

can preserve system stability and facilitate secure and efficient system restoration. By examining the different interactions and interdependencies across the hybrid system, the thesis seeks to define minimum requirements for a resilient MTDC grid capable of handling DC-side contingencies without compromising the integrity of the connected AC systems.

1.2 Modern power systems

Climate change impacts have led to the decarbonization of power systems around the globe, a process known as the energy transition. As an ongoing process, it is reshaping bulk power systems: power transmission, generation and demand are updating with more power electronics, as conceptually illustrated in Figure 1.4. The massive penetration of converters in power grids is taking the overall system behavior to a new paradigm, where grid strength and local inertia can be compromised due to the operational characteristics of converter- interfaced resources [23]. On the load side, new behaviors are appearing with the interconnection of data centers, flexible hydrogen production and electric vehicles (EVs). Together, new generation and consumption behaviors are challenging in new ways the power system stability [24], [25].



Figure 1.4: European power systems' evolution [24]

1.2.1 Transmission and generation

The energy transition is reshaping the power system on two main fronts. First, conventional AC power sources using synchronous generators are being largely replaced by inverter-based resources (IBRs)—primarily PV solar and wind power. The natural fluctuation of these IBRs increases the need for operational flexibility. Second, the transmission infrastructure is being upgraded through the widespread commissioning of High-Voltage Direct Current (HVDC) systems. HVDC systems distinguish in terms of bulk power transmission for long distances, submarine interconnections, and power flow controllability, integrating high voltage hybrid AC/DC systems [26].

At transmission level, DC system topologies become increasingly complex, evolving from point-to-point monopole configurations toward multi-terminal (MT) systems with bipolar converter stations [27]. This expansion is expected to lead to meshed MTDC networks, which provide redundant power flow paths in the event of an N-1 DC contingency, thereby enhancing overall system resilience and reliability (R&R).

Furthermore, as offshore wind farms (OWFs) grid connections have evolved, HVDC systems are now converging to a standardized configuration: bipole stations with half-bridge MMCs rated at ± 525 kV 2 GW [14], [28]. The standardization of these systems brings several advantages. On the one hand, it allows for easier scaling of components' production, and economies of scale, on the other, it brings design and operational advantages, as these keep a shared basis across different projects, accelerating familiarity with this kind of systems and projects' execution time[28]

1.2.2 Dynamic loads and storage

Hydrogen production has emerged as a critical flexible load, utilizing a fast-response grid-connected converter to operate across a wide power range. Its primary role is to serve as a versatile energy vector, producing green fuel for various downstream applications [29], [30]. Data centers are similarly reshaping electricity demand profiles, though their complex grid interactions and systemic implications remain an active research area [31]. In addition to these dynamic loads, the increased adoption of EVs and heat pumps by society is reshaping consumption profiles [24]. Concurrently, Battery Energy

Storage Systems (BESS) are gaining prominence in modern power systems, designed to provide essential ancillary services, such as inertial and voltage support [32].

1.3 MTDC systems control and protection challenges

Ensuring system safety and stable operation, together with R&R, is essential. This becomes particularly important when power systems' layout modified, and their operating conditions change, especially with the integration of new technologies [25]. The lack of voltage stiffness takes notorious relevance, as IBR and other power converters regularly operate with the GFL strategy, that relies on the AC grid voltage behavior, posing operational challenges for control of HVDC converters. Therefore, these structural changes necessitate a fundamental reassessment of how control strategies participate in sustaining stability in increasingly complex networks.

On the DC side, fast voltage regulation is a fundamental design aspect, which, a priori, does not bring foreseeable issues to the GFL strategy; nonetheless, when utilizing the GFM strategy, delivering both AC and DC services appears as a challenging task, as, on the one hand, energy is used to deliver frequency support to the AC system, and, on the other hand, deliver voltage regulation support to the DC grid. Thus, although in principle, this analysis might suggest an impasse in managing these competing priorities, the extended use of GFM in MTDC systems has not been fully described and understood when implemented in conjunction with GFL strategy or as the sole strategy regulating DC voltage.

On the MTDC system protection side, a theoretical framework has been developed in recent years. However, while the underlying principles of reliability, speed, and sensitivity remain constant, the implementation in DC grids is fundamentally different due to the lack of natural current zero-crossings and the extremely low impedance of DC networks. These factors necessitate protection schemes that can respond within milliseconds to prevent catastrophic damage to sensitive power electronic components.

Similar to the approach taken in AC systems, design of DC protection strategies is based on established protection philosophies. These protection philosophies are dis-

tinguished by their level of selectivity, namely: fully selective, partially selective, and non-selective [33], [34]. Each strategy defines the extent to which a fault can propagate through the system and how the resulting fault current is managed using circuit breakers, current limiters, and switches. Consequently, the choice of a protection strategy is primarily driven by the acceptable level of fault impact on the hybrid system operation and the associated costs.

Despite the maturity of these protection philosophies, a low-hanging fruit remains unaddressed in research: coordination of C&P actions to delineate open-loop control sequences has not been comprehensively addressed when utilizing different protection philosophies in the presence of a DC fault. Challenges from an integrated electronic and electric perspective, coming from the intertwined development of C&P that impose new system dynamics, have not been clearly identified and addressed, as GFM strategy remains an open frontier for MTDC systems studies. This thesis aims to bridge this gap: it will investigate the cross-layer interactions between GFM strategy with other MMC control loops and different DC protection philosophies, contributing to the development of a clearer roadmap for the stable and resilient operation of future hybrid AC/DC systems.

1.4 Research Challenges, Gaps and Objectives

The progression from Sections 1.1 to 1.3 establishes the technical context motivating this research. Section 1.1 highlighted the growing deployment of HVDC technology and the emerging role of MTDC systems as key infrastructure for offshore wind integration and the interconnection of asynchronous AC systems. Section 1.2 showed that modern power systems are evolving toward converter-dominated architectures, where decreasing grid strength and inertia create new operational challenges for system stability, thereby motivating the adoption of GFM control strategies. Finally, Section 1.3 identified the main challenges associated with MTDC system control and protection during large disturbances, particularly DC faults. Together, these sections reveal several research challenges and knowledge gaps that remain insufficiently addressed in the existing literature and motivate the work presented in this thesis.

The literature review reveals that significant progress has been achieved in three areas independently: MTDC control, DC protection strategies, and GFM converter control. However, future MTDC grids are expected to operate through the combined application of these technologies. Consequently, understanding their interactions under large disturbances becomes increasingly important. While previous studies have addressed individual aspects of these topics, a comprehensive EMT-level assessment of the interactions between converter control strategies and protection philosophies throughout the complete DC fault ride-through sequence is still lacking. This limitation becomes particularly relevant for future converter-dominated power systems where GFM control is expected to play an increasing role.

Consequently, several gaps remain regarding the coordinated operation of MTDC systems during DC fault ride-through. First, the majority of existing studies focus either on protection system design or converter control performance separately, whereas the interaction between control and protection actions across the complete DC FRT sequence has received less attention. Second, the increasing interest in GFM control introduces new dynamic interactions between AC and DC systems that are not yet fully understood, particularly when GFM control is combined with conventional GFL converters within hybrid AC/DC systems. Third, the influence of different protection philosophies, namely non-selective and partially selective approaches, on these interactions and on the overall DC FRT capability of MTDC systems has not been comprehensively characterized. Finally, while GFM control is expected to provide enhanced support to weak AC systems, its implications for DC voltage regulation and coordination with MTDC protection schemes remain an open research question.

1.4.1 Research Questions, Objectives of the Thesis and Scientific Contributions

To address these gaps, this thesis focuses on the DC fault ride-through performance of meshed MTDC systems and investigates the interaction between converter control strategies and protection philosophies. The research is guided by the following questions:

- What are the characteristic phenomena that appear during the different stages of DC fault ride-through in MTDC systems?
- How do GFL and GFM converter control strategies influence system performance during fault clearing and restoration?
- How do different protection philosophies affect converter behaviour, system stability and MTDC restoration?
- What control interaction mechanisms emerge between AC and DC control objectives during DC FRT?
- Which coordinated control and protection solutions can mitigate these interactions and enable resilient operation of future hybrid AC/DC systems?

Based on these research questions, the objectives of this thesis are formulated as follows

- Identify and characterize key or typical phenomena of the system dynamic performance throughout DC fault ride-through of AC-DC systems when using a non-selective protection strategy with GFL as reference control, followed by GFM control
- Identify and characterize key or typical phenomena of the system dynamic performance throughout DC fault ride-through of AC-DC systems when using a partially selective protection strategy with GFL as reference control, followed by GFM control
- Identify system-wise issues and requirements to perform proper DC FRT in the proposed use cases and propose new design options (e.g. new protection sequences taking advantages of new technological devices, or new coordinated control algorithms to increase the DC fault ride-through of the entire system, etc.)
- To perform validation on off-line simulation experiments with the aim to test the proposed/selected design features and to confirm the main findings

The scientific contributions of this thesis are the following:

- Generic DC FRT C&P sequencing further development to maintain system safe operation and stability when using a non-selective and partially selective protection strategies. Proposition of minimum coordinated C&P actions to perform system-wise DC FRT
- Characterization of the system dynamic performance with a reference control throughout DC FRT with generic non-selective and partially selective protection strategies
- Characterization of control interaction mechanisms throughout the DC FRT that might jeopardize the system stability when facing a weak grid
- Characterization of control interaction mechanisms throughout the DC FRT that might jeopardize the system stability when using GFM with generic non-selective and partially selective protection strategies
- Proposition of mitigation solutions to decouple control interactions and enable the use of GFM control as the sole control strategy regulating the DC system voltage

1.5 Outline of the work

The chapters of this thesis are structured to progressively build the analysis from fundamental concepts toward increasingly complex control and protection scenarios. he chapters of this thesis are structured to progressively build the analysis from fundamental concepts toward increasingly complex control and protection scenarios.

Chapter 2 establishes the theoretical and modelling foundations of the work by defining the hybrid AC/DC system architecture, MMC modelling assumptions, control strategies, protection philosophies, and the general DC FRT framework. These concepts constitute the basis for all subsequent investigations.

Building on this foundation, **Chapter 3** introduces the DC FRT analysis using a non-selective protection philosophy and GFL control as a reference case. This chap-

ter establishes the baseline understanding of the system behaviour during DC faults, identifies characteristic transient phenomena, and reveals the first control interaction mechanisms under weak-grid conditions.

Using the observations and methodologies developed in Chapter 3, **Chapter 4** extends the analysis to the integration of GFM control. The chapter progressively increases the participation of GFM converters in MTDC voltage regulation, enabling the identification of additional AC/DC control interactions and their implications for system stability. The mitigation measures proposed in this chapter form the basis for the subsequent studies.

Chapter 5 then applies the methodologies and conclusions obtained in Chapters 3 and 4 to a more advanced protection framework based on the partially selective philosophy. The chapter demonstrates how changes in the DC electrical circuit imposed by the protection strategy affect converter dynamics and control interactions, and it evaluates the feasibility of extending GFM control as the sole strategy regulating DC voltage under these new operating conditions.

Finally, **Chapter 6** consolidates the findings obtained throughout the thesis, relates them to the research objectives introduced in Chapter 1, and summarizes the contributions derived from the successive analyses conducted in Chapters 3, 4, and 5. While in **Appendix A**, the derivation of the characteristic equation of the GFM approach used in this thesis is demonstrated.

1.6 List of Publications

Part of the work developed throughout the industrial PhD period resulted in the following publications:

- J. Castellanos, F. Perez, A. Zama, A. Benchaib, and L. Xu. "DC grid re-energization Analysis during DC fault ride-through of bipolar MTDC systems with energy-based MMC control in grid-following". In IET Conference Proceedings CP963 (Vol. 2025, No. 44, pp. 83-88). Stevenage, UK: The Institution of Engineering and Technology. (Invited by the Editor-in-Chief of the gold open

access journal IET Power Electronics to contribute an extended journal article based on original conference proceedings.)

- J. Castellanos, F. Perez, A. Zama, A. Benchaib, and L. Xu. "Assessment of Grid-Forming MMC Energy-Based Control during DC Fault Ride-Through in MTDC Systems". Submitted to IEEE Transactions on Power Delivery, 2026.(Going through a second review process).

- J. Castellanos, F. Perez, A. Zama, A. Benchaib, and L. Xu. "DC FRT Analysis and Disturbance Propagation of Grid-Forming HVDC Converters in Future MTDC Systems" ID: 11951. B4 DC Systems and Power Electronics PS3 New Technologies and Concepts of DC and FACTS enabling energy transition. Paris CIGRE Session 2026

- F. Perez, J. Castellanos, J. C. Gonzalez Torres, A. Benchaib, and L. Xu, "Contributions to DC fault ride-through in MTDC meshed grids with MMC stations in grid-forming control considering impacts on AC system stability". 22nd IET International Conference on AC and DC Power Transmission, 2025.

1.7 Contributions to project deliverables

Part of the work developed throughout the industrial PhD period resulted in the following project deliverables' subsections:

I HVDC-wise project Deliverable 3.3 Protection Concepts for AC/DC architectures - DC Fault-Ride Through Analysis. 2024.

II HVDC-wise project Deliverable 7.3 Use Case 3 DC Protection Aspects. 2026.

Chapter 2

AC/DC hybrid system model and hypothesis of work

2.1 Chapter introduction

This chapter introduces the core concepts of the thesis that will be adopted and used for the following chapters. It starts with an overview of AC/DC systems to provide context, followed by a review of key HVDC system architectures. The specific base architecture used for all subsequent studies is then defined. The characteristics of the proposed hybrid AC/DC system are analyzed to identify its most critical operational requirements. This analysis underscores the relevance of the core research problem addressed in this work.

To establish the necessary technical background, this chapter then delves into two foundational areas for HVDC system operation: MMC control and DC grid protection. To better understand the MMC control aspects, key characteristics of the MMC hardware components and control philosophies are detailed. The development of DC protection considering the impact on interconnected AC systems is introduced. This is followed by the review of DC protection philosophies for primary protection, highlighting the main characteristics of each philosophy. Given the wide range of possible protection strategies, the reviewed cases serve as representative examples of potential approaches for MTDC systems. Once the main C&P characteristics are reviewed, a

DC FRT flow diagram is presented, outlining the essential steps of the DC FRT process and its relationship with the system resilience level. The chapter concludes with a summary of the hypotheses taken in this work, and how the presented concepts will be used throughout the thesis.

2.2 The AC/DC hybrid system

2.2.1 The AC/DC hybrid system architecture

Potential hybrid AC/DC system architectures have been analyzed in [35], considering their level of embedment, overhead line/cable connection topologies, converter station configurations, and key technological components such as breakers and energy storage devices. For environmental compliance [36], [37], HVDC systems with offshore stations typically require a dedicated metallic return (DMR). The DMR provides a ground connection for the converter's neutral point, establishing a zero-voltage reference [38].

For purposes of this research, a minimum meshed DC grid in a bipolar configuration has been identified as a representative architecture, as depicted in Figure 2.1. Bipolar configuration presents a small cost difference with respect to the monopolar configurations, because cable costs largely dominate the overall system capital expenditure (CAPEX). HVDC cables require specialized manufacturing, with high-grade insulation, and the use of particular vessels and skilled workers, making the maritime installation rather expensive; their cost scales linearly with distance. Several HVDC cable types are available in the market, such as self-contained oil-filled and self-contained fluid-filled (SCOF and SCFF) cables, high-pressure oil-filled/high-pressure fluid-filled (HPOF and HPFF) cables, where the fluid can be either oil or gas, and Cross-Linked Polyethylene (XLPE). Most recent projects have a tendency to use XLPE cables [14]. Some cables may include optical fibers for communications, cable temperature monitoring and fault location requirements [39], [40], [41], [42], [43], [44], [45], [46]. Converter redundancy of bipolar systems offers significantly higher reliability; if one pole fails, the system can still transmit 50% of its rated power using the remaining pole [47], [48]. Thus, for large-scale power integration, the increased reliability often justifies the marginal

increase in station CAPEX. Moreover, this generic topology facilitates the restoration of pre-fault power flows following a DC fault within the ring network, representing a potential key advantage over other architectures based on radial topologies.

In this work, DC FRT for a hybrid system based on an MTDC grid is analyzed. The defined MTDC grid constitutes a minimum mesh with four terminals in a bipolar configuration, interconnecting two asynchronous AC grids and two offshore wind farms (OWFs), as depicted in Figure 2.1. This generic yet representative architecture captures key characteristics that enable the investigation of critical phenomena—within both the interconnected AC systems and the DC grid itself—during DC FRT events. It thus provides a suitable platform for testing converter control and protection schemes for future hybrid AC/DC systems.

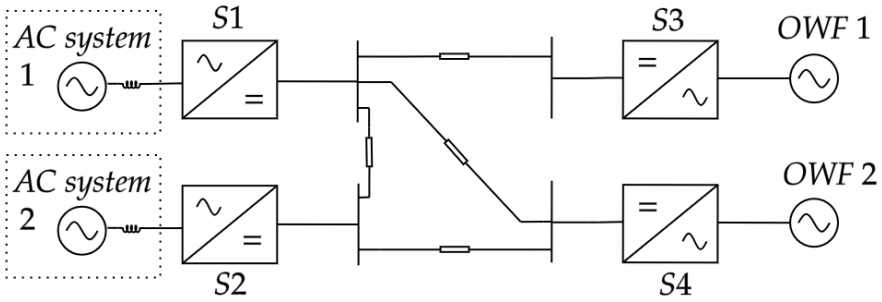


Figure 2.1: AC-DC system single line diagram

Asynchronous systems 1 and 2 can be modeled at varying levels of detail, depending on the study focus. A simplified representation is sufficient for analyses centered on MTDC operation and dynamics, whereas a more detailed model is necessary to accurately capture interactions with and impacts on the interconnected AC grids. For simplified AC grid representation, Thévenin equivalent impedances will be employed. Specific details of protection elements, such as DCCBs or line inductors, will be defined according to the requirements of each protection strategy under investigation.

Given that the study focus is on control implementation at the onshore Stations 1 and 2, the OWFs and the offshore HVDC stations are modelled in a simplified manner. These elements are represented as either voltage sources or controlled current sources, interfaced to the MTDC grid via GFL converters in active power mode (P-mode)

or voltage/frequency (V/f) control, respectively. The system main parameters are depicted in Tables 2.1 and 2.2.

Table 2.1: MMC parameters

Parameter	**Value**
S_{nom}	1000 MVA
V_{ac}	400 kV
V_{dc}	525 kV
Transformer	0.001+0.18j pu
Arm inductance	0.15j pu
Conduction losses per SM	0.001 Ω
Submodules per arm	400
MMC Electrostatic constant	0.04 s

Table 2.2: Cable data

Parameter	**Type/Value**
Model	Single core
Core conductor radius	0.032 [m]
Metallic sheath inner radius	0.0569 [m]
Metallic sheath outer radius	0.0582 [m]
Conductor resistivity	2.83 e-8 [Ohm-m]
Conductor relative permeability	1
Insulator relative permeability	1
Insulator relative permittivity	2.5
Insulator loss factor	0.0004
Model	Wideband
Number of decades	10
Points per decade	20
Minimum frequency	0.01 [Hz]
DC frequency	0 [Hz]

2.2.2 AC and DC grids' services

Both AC and DC grids require specific services from power converters. As fewer synchronous generators and more IBRs —typically operating in GFL mode- are integrated in power systems, overall AC grid voltage stiffness decreases. This weakens the grid strength and heightens the need for a stable voltage reference and dynamic voltage

control services. Under weak grid conditions, disturbances can be more easily amplified, potentially leading to cascading events and inappropriate protection activations, as exemplified by recent events such as the Iberian peninsula blackout [49].

Simultaneously, as synchronous generators are phased out or relegated by the merit order [50], overall system inertia decreases. This reduction leads to a faster rate of change of frequency (RoCoF) following a power imbalance. Such imbalances can arise from unforeseen events, such as a sudden drop in solar PV or wind power generation, or from abrupt load changes—for example, significant shifts in data centres' consumption [51].

A higher RoCoF places greater stress on power system equipment, accelerating degradation and risking serious damage. It can also trigger RoCoF-based protection, potentially initiating cascading trip events. Furthermore, the shortened response window for primary controls of conventional generators—such as speed governors—can compromise their ability to provide effective frequency regulation. If the frequency deviation is not adequately contained, it may reach levels that activate under-frequency load shedding (UFLS) schemes [52], [53]. Consequently, inertial support emerges as a critical primary service required by AC systems.

Power converters are capable of providing both voltage support and inertial response when equipped with a suitably designed control strategy. In low grid stiffness conditions, however, the GFL control strategy has inherent limitations during transients due to its current-source behavior and reliance on an external phase-angle reference, which is typically obtained from a phase-locked loop (PLL). During grid disturbances, this dependency can lead to degraded converter performance as the PLL struggles to maintain synchronization, resulting in complex oscillatory behavior at the AC point of connection (PoC). This fundamental characteristic limits the effectiveness of GFL control, even when enhanced with dedicated AC service loops in its outer control layers [54], [55], [56], [57]. In contrast, the GFM strategy—specifically in the virtual synchronous machine (VSM) approach—is recognized as better suited to deliver these grid services. This is due to its inherent voltage-source behavior and its ability to provide emulated inertia [58].

On the DC side, proper DC voltage regulation is essential, which is typically managed with a master-slave coordination in point-to-point DC systems. Yet, for MTDC grids, the voltage regulation role is expected to be performed by a coordinated action from different converters, e.g., by means of DC voltage – active power (Vdc-P) droops [59], [60]. By setting the droop coefficient, each converter can participate in this role.

Consequently, power converters are expected to provide these combined AC and DC services. One approach is the joint implementation of a GFM strategy, specifically a VSM control, alongside Vdc-P droop control. However, simultaneously fulfilling AC and DC service requirements and maintaining the MMC energy level for operational integrity can present conflicting control objectives. The inherent energy storage of the converter's submodules —potentially augmented by an external reservoir— provides a buffer for the associated power exchanges. Consequently, an energy-based control strategy appears adequate to regulate the MMC's internal energy, prevent limit violations, and enable the delivery of required services within finite energy constraints [61], [62].

Therefore, this research analyzes a VSM integrated energy-based MMC control strategy, operating in Vdc-P droop mode during DC FRT of a hybrid AC/DC system. The converter must thereby manage the distinct dynamic demands of the AC and DC grids, functioning as a finite-energy buffer to support overall system stability.

2.3 MMC characteristics

The following section presents the fundamental MMC operating characteristics and the associated control strategies. Key aspects discussed include the converter's internal energy dynamics, voltage regulation principles, physical limits governing its output current, and consequently, the required protection for the MMC.

2.3.1 MMC physical arrangement

Figure 2.2 shows a basic 3-phase MMC configuration, having an inductance per arm and two arms per phase. The use of numerous submodules (SMs) per arm, from dozens to several hundred in high-voltage applications, synthesizes a multilevel voltage waveform

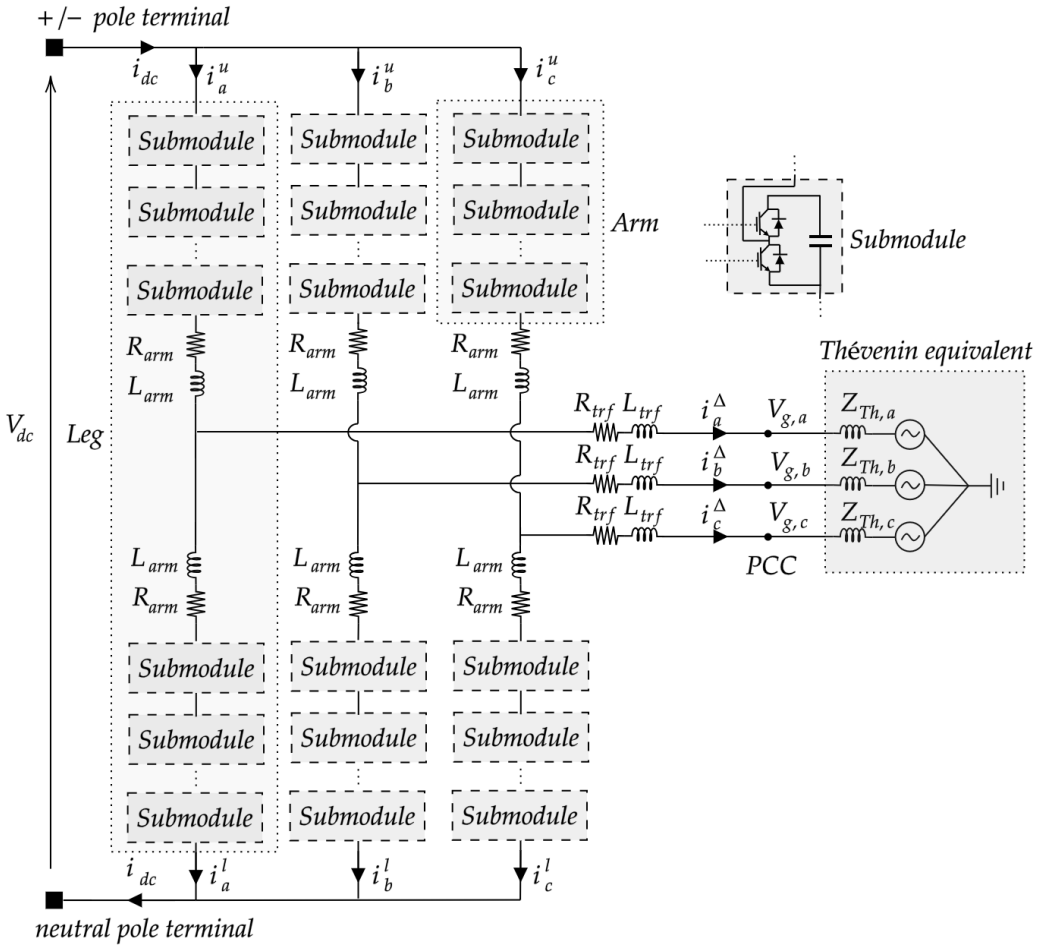


Figure 2.2: MMC representation with simplified submodules.

with minimal harmonic distortion and high-frequency noise [61], [63], [64].

Among the various submodule topologies explored, the half-bridge submodule (HBSM) is predominantly used in HVDC systems [64], as it offers an optimal balance between performance, power losses, and cost. As shown in Figure 2.2, the HBSM comprises two insulated-gate bipolar transistors (IGBTs) with antiparallel freewheeling diodes and one capacitor. This topology provides independent control of active and reactive power, enabling full four-quadrant operation [65]. The MMC control is implemented by commanding the IGBTs to either insert their submodule capacitor into the arm current path or bypass it, thereby generating the desired multilevel output voltage.

Typical MMC control system is composed of a high-level and low-level control [66], [67], [68]. The high-level control fulfills the system-level control objectives, delivering

arm voltage references to the low-level control. The low-level control is responsible for inserting or bypassing specific submodule capacitors to satisfy high-level control objectives. By integrating switching modulation techniques with submodule balancing algorithms, it ensures safe and efficient operation while maintaining balanced voltage levels across all converter arms [69], [70].

2.3.2 Arm averaged-value model

In the context of the system-level studies aimed for this thesis, the details of the submodules switching and balancing are not of interest. Therefore, the arm Averaged-Value Model (AVM) is used. This model assumes that every submodule in the arm is well balanced, while considers the energy transferred between the AC and DC grids. Thus, it is suitable for the purposes of this thesis [71]. A representation of the MMC model used in this research effort and its interconnection with the AC grids is presented in Figure 2.3.

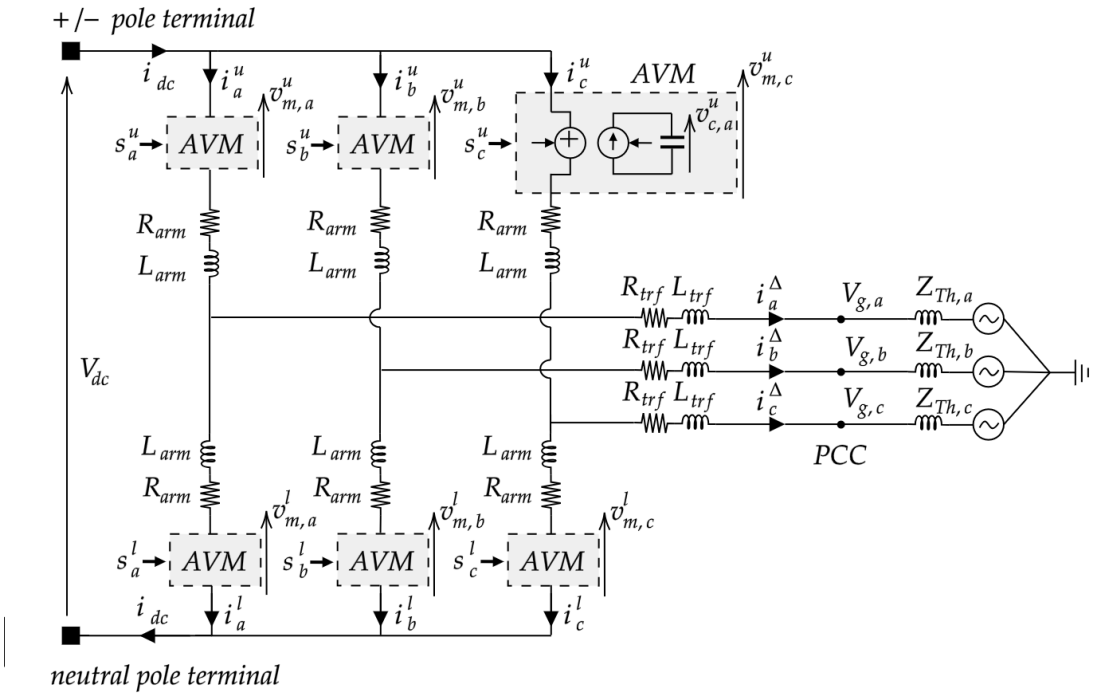


Figure 2.3: MMC with averaged value model arm representation.

2.4 MMC control and protection

Energy stored in the MMC submodules acts as an energy buffer between AC and DC sides, in contrast with other kinds of voltage source converters (VSCs) [65]. The characteristics of the MMC valves, namely the IGBTs' voltage and current ratings, restrict the operating ranges of the whole converter during normal operation and transient events. To protect submodule integrity during large disturbances, when currents exceed submodules' protective levels, dedicated protection measures are activated. In the case of a DC fault, the switching elements could be jeopardized by the high fault current [34], [72]. To address this, MMC protection systems operate to safeguard the submodules by blocking the IGBTs in the submodules and triggering appropriately rated unidirectional switches, thereby bypassing the submodules. Accordingly, this section provides a brief review of MMC control philosophies, primary strategies, and submodule protection.

2.4.1 MMCs' control philosophy

MMCs control strategies can be based on two main control philosophies, namely, the non-energy-based control and energy-based control. The non-energy-based MMC control is an adoption of earlier control of legacy power converters, i.e., two- and three-level VSCs, which do not have energy storage capacity. The VSC DC-link capacitor fluctuates with the DC system voltage following the expected voltage level from the VSCs' higher-level control commands [65], [73]. On the other hand, the development of the energy-based control philosophy addresses issues found in the non-energy-based control, based on the degrees of freedom and state variables available in the MMC architecture [61], [68], [74], [75], [76], [77].

a) Non-energy-based control

Control architectures for two- and three-level VSCs with no inherent energy storage capability have been developed to manage the main converter outputs, namely, its active, reactive power output and DC voltage. In contrast, MMC has capacitors as part

of each submodule; this configuration can result in circulating currents flowing among the converters arms if their charging levels are not properly balanced. Minimizing these currents can reduce the distortion of the arms' currents and capacitor voltage ripples, improving voltage signal quality [61], [78]. Therefore, the non-energy-based control capacitors' charging state or MMC internal energy level is left without explicit control.

b) Energy-based control

The purpose of energy-based control is to maintain the total energy in the MMC submodule capacitors to a desired level, enabling the proper switching and converter operation. This control gives the command to absorb or release power from the MMC in order to balance (or compensate) dynamic variations or steady-state oscillations in the converter submodule capacitors [75], [79]. The per unit MMC total or internal energy is calculated as given by (2.1) and (2.2). Where W_{tot} is the MMC total or internal energy, W_{tot}^{n} is the n leg total or internal energy, lastly, $V_{dc}^{n,u}$ and $V_{dc}^{n,l}$ upper and lower arm voltages per n phase, respectively. Based on system operating conditions, the power converter's internal energy can be regulated by the AC or DC grids [61]. Thus, the energy-based control ensures the converter sustains a safe operating internal energy level, which, in coordination with DC voltage control, allows the power converter to participate in the overall DC system energy regulation.

$$W_{tot} = \frac{W_{tot}^{1} + W_{tot}^{2} + W_{tot}^{3}}{3} \tag{2.1}$$

$$W_{tot}^{n} = \frac{V_{dc}^{n,u2} + V_{dc}^{n,l^2}}{2}, for \quad n = 1, 2, 3 \tag{2.2}$$

In addition to the regulation of overall MMC internal energy, it is important to maintain a balanced voltage and energy states among the converter phase legs, and its upper and lower arms. For this objective, a dedicated control is typically implemented to maintain energy balance among the three converter legs, referred to as horizontal energy control; while another control is used to balance the upper and lower arms at each converter leg, referred to as vertical energy control [80].

In this thesis, the DC side is selected to regulate the MMC internal energy under

normal operation, as in a classic energy-based control scheme [75]. Furthermore, as GFM control is required to support AC network, the use of the DC system to regulate the MMC internal energy represents the most suitable alternative. Therefore, the higher-level of the DC cascading control is composed of the total energy controller, the horizontal and vertical balancing control, and the feedforward of the droop or power reference.

c) Virtual capacitor control and DC voltage control enhancement

The virtual capacitor principle enables a virtual expansion of the MMC energy storage [81]. This is achieved by providing a dynamic reference to the internal energy controller, which incorporates a virtual energy buffer proportional to the difference between the DC voltage and a desired reference level. In its most general approach, given by (2.3); this control method uses an equivalent capacitance, C_{eq}^{vc}, which accounts for the converter capacitive elements and a certain part of the DC grid, thus considers the power required to manage this equivalent capacitance. The virtual capacitor coefficient k_{vc} scales the buffering effect of the aggregated capacitance, increasing or reducing the sensitivity to DC voltage variations from the nominal value, V_{dc}^{*}. To take advantage of this feature and simplify the analysis, coefficients C_{eq} and k_{vc} are set to 1. In this manner, this control approach couples the converter energy level to the grid's DC voltage state, expanding the DC system energy storage and its stability region. Furthermore, it is well acknowledged that the virtual capacitor principle improves the converter response during DC transient events (see [75], [82], [83]). However, its performance under large disturbances has not yet been fully assessed.

$$W_{vc}^{*} = W_{tot}^{*} - C_{eq}^{vc}\, k_{vc}(V_{dc}^{*\,2} - V_{dc}^{2}) \tag{2.3}$$

The closed-loop transfer function of the energy control is presented in (2.4). Its tuning is obtained by means of comparison of its characteristic polynomial, with the second-order system characteristic equation, defining the desired response time and damping. C_{Σ}^{Wtot} represents the aggregated capacitance of the DC grid and the virtual capacitor, k_{p}^{Wtot} is the proportional gain, and k_{i}^{Wtot} is the integral gain of the controller

[83].

$$G_{Wtot}(s) = \frac{W_{tot}}{W^*_{tot}} = \frac{2k_p^{Wtot}s + 2k_i^{Wtot}}{C_\Sigma^{Wtot}s^2 + 2k_p^{Wtot}s + 2k_i^{Wtot}} \tag{2.4}$$

2.4.2 MMC control architecture and control strategies

The state and control variables of the converter, in conjunction with the voltages of the interconnected AC and DC systems, are used to deliver the desired output power and grid services to both sides of the converter [79]. As previously highlighted, the high-level control architecture is the most relevant from a system-level perspective, as it computes and provides the required modulation indices or control variables to the low-level control in order to achieve the desired power output and grid services. In the cascaded high-level control architecture of the MMC, these control variables serve as the key confluence point. Their mathematical definitions are provided in (2.5) and (2.6) [82]; where v^{Δ}_{abc} is the difference voltage reference, and v^{Σ}_{abc} is the sum voltage reference, used to control the AC side and DC side converter voltages and deliver corresponding output currents.

$$v^{\Delta}_{abc} \stackrel{def}{=} \frac{-v^u_{m,abc} + v^l_{m,abc}}{2} \tag{2.5}$$

$$v^{\Sigma}_{abc} \stackrel{def}{=} \frac{v^u_{m,abc} + v^l_{m,abc}}{2} \tag{2.6}$$

a) MMC high-level control architecture

The expected services to be studied in this work include the power exchange between AC and DC systems, inertial and voltage support for the AC system, and DC voltage regulation. To this end, the used control architecture is depicted in Figure 2.4 and further detailed in the following subsections. As the control philosophy is considered to be energy-based, the DC voltage regulation is integrated in the architecture and is channelled to both the AC and DC cascaded loops. The DC cascaded control is mainly composed by the controllers regulating the MMC energy, as in a classic energy-based control scheme [75]. While the main part of the AC cascaded control is defined based

on the given AC side control strategies, namely, GFL or GFM.

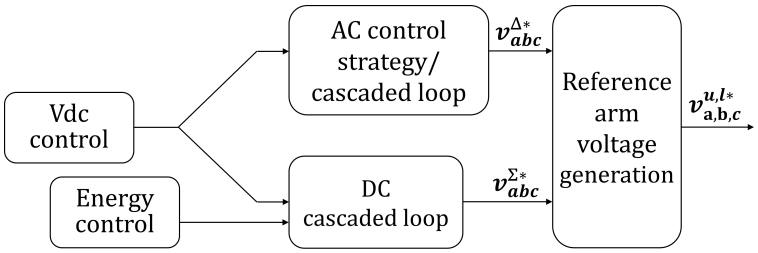


Figure 2.4: MMC cascaded control architecture.

b) GFL control strategy

This control strategy is the most commonly implemented in power converters interconnected to the transmission grid. This control leads the power converter to have a current source behavior, as it follows the grid voltage phase angle by locking the measured voltage q-component to zero: this creates a synchronous reference frame which allows the alignment of the current phase with the grid voltage in order to inject or absorb a desired amount of power.

Voltage angle at the PoC is estimated by the PLL, the block diagram of which is presented in Figure 2.5. Typically, a rate limiter and a second-order low-pass (LP) filter are employed to improve the PLL response during fast dynamic events. During a phase jump or large disturbance, a rate limiter prevents the PLL from attempting to track the change instantly, ensuring that the frequency and angle change at a physically manageable rate for the converter. Simultaneously, the LP filter attenuates high-order harmonics (e.g., 5th and 7th) or high-frequency oscillations in the grid voltage. This signal processing is particularly critical for the effective decoupling of the d- and q-axis components within the inner current control loop [55], [84], [85], [86].

Significant power disturbances, e.g., sudden loss of load or generation, can lead to voltage oscillations at the AC PoC. These oscillations will cause the power converter to inject power with the estimation of the varying voltage angle, while the voltage q component will not be zero anymore, as depicted in Figure 2.6. In the case of a weak grid condition, i.e., a short circuit ratio (SCR) < 3 [53], - characterized by a low voltage

stiffness at the PoC - the injection of power with a fast varying angle can enhance the oscillations and take the converter operation closer to stability margins [56].

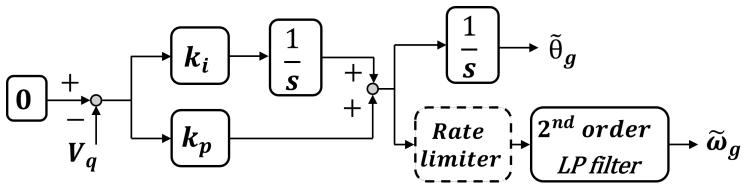


Figure 2.5: Phase-Locked Loop (PLL) block diagram [53, 81].

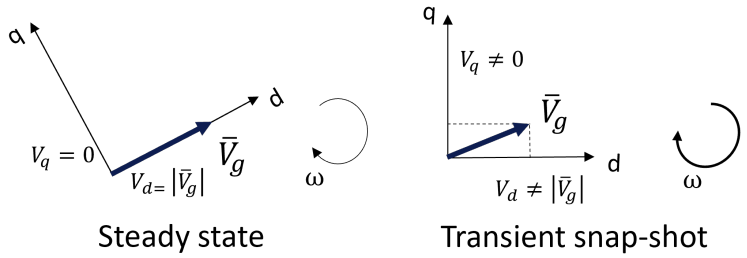


Figure 2.6: Phase-Locked Loop (PLL) operation example.

The high-level control architecture of the MMC, employing a GFL strategy under normal operating conditions, is illustrated in Figure 2.7. In this configuration, both the Vdc-P droop and P-control modes share the same cascaded control structure. As highlighted before, since the converter control is energy-based, either the power or droop reference is feedforward to the DC cascading control loop to avoid undesired actions of the energy control and keep a balance between the converter AC and DC power flows.

Within the DC reference aggregation block, the Vdc-P droop and total energy control references are distributed evenly to each converter leg. These are subsequently summed with the horizontal and vertical energy controllers' references to form the sum current references for each phase, i^{Σ}_{abc}. Both the AC and DC control loops use an inner-current controller to give the difference, v^{Δ}_{abc}, and sum, v^{Σ}_{abc}, voltage references, respectively [82]. The transfer functions of these controllers are given by equations (2.7) and (2.8) [86], [87]. The rise time of the current control loops is on the order of

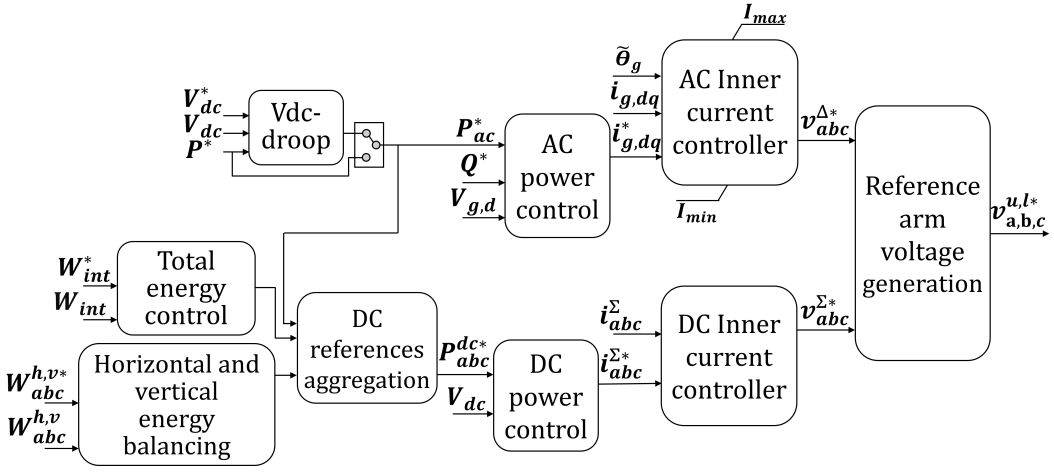


Figure 2.7: GFL cascaded control architecture.

10^{-3} s. The time constant of the energy controller is on the order of 10^{-2} s.

$$G_{ig,dq}(s) = \frac{i_{g,dq}}{i^*_{g,dq}} = \frac{1 + \frac{k_p^{i_{g,dq}}}{k_i^{i_{g,dq}}} s}{\frac{L_{eq}^{ac}}{k_i^{i_{g,dq}}} s^2 + \frac{k_p^{i_{g,dq}} + R_{eq}^{ac}}{k_i^{i_{g,dq}}} s + 1} \tag{2.7}$$

$$G_{idc}(s) = \frac{i_{dc}}{i^*_{dc}} = \frac{1 + \frac{k_p^{i_{dc}}}{k_i^{i_{dc}}} s}{\frac{L_{eq}^{dc}}{k_i^{i_{dc}}} s^2 + \frac{k_p^{i_{dc}} + R_{eq}^{dc}}{k_i^{i_{dc}}} s + 1} \tag{2.8}$$

c) GFM control strategy

The fundamental characteristic of GFM control is the voltage source behavior behind an impedance [88]. From the various GFM control approaches [89], [90], the VSM approach is adopted in this research study. The MMC high-level control architecture with the GFM strategy is presented in Figure 2.8, and its control block diagram is shown in Figure 2.9 [91], from which its characteristic equation (2.9) is obtained, as presented in Annex A. In (2.9), H is the inertia constant, k_d is the damping coefficient, ω_{vsm0} is the nominal VSM frequency, v_Δ is the modulated converter AC voltage, V_g is the voltage at the converter PoC, and X_{eq} the equivalent impedance between the PoC and the converter submodules.

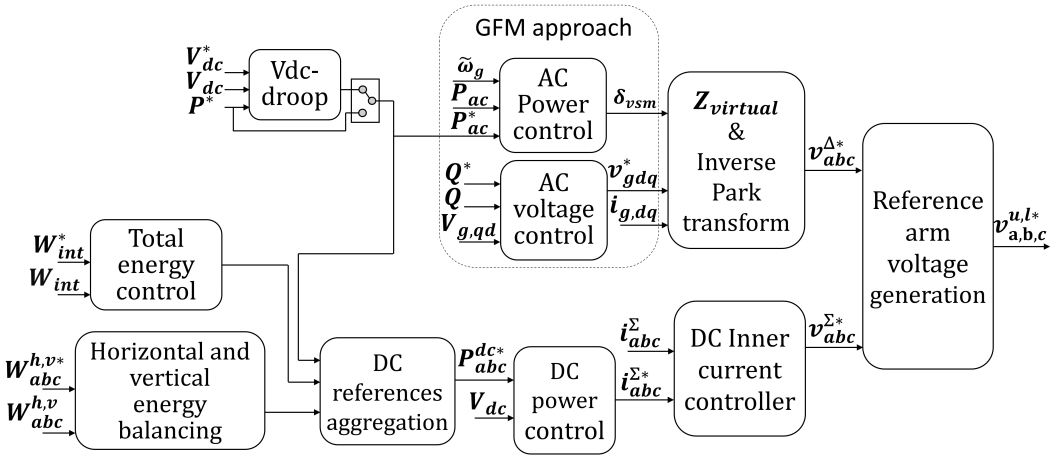


Figure 2.8: GFM cascaded control architecture.

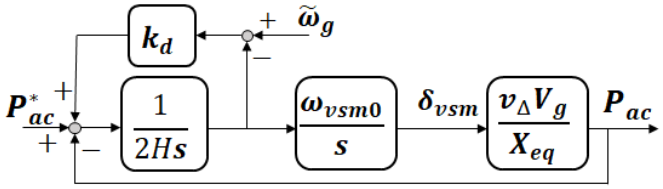


Figure 2.9: VSM AC power control block diagram [88].

$$s^2 + \frac{k_d}{2H}s + \frac{\omega_{vsm0}\ v_\Delta V_g}{2HX_{eq}} = 0 \tag{2.9}$$

The swing equation is emulated in (2.10). k_d can be tuned to meet desired dynamic responses, while H should meet the interconnected AC grid needs. The voltage angle is obtained by the integral of (2.10), where P_{ac} is the measured power in the converter, P^*_{ac} is the power reference, $\dot{\omega}_{vsm}$ is the computed frequency by the VSM, and $\tilde{\omega}_g$ is the grid frequency estimated by a PLL. The voltage amplitude is obtained by a Q-Vac droop as given by (2.11), where V^*_d is the AC voltage magnitude reference, m_v is the voltage droop coefficient, Q^* is the reactive power reference and Q is the measured power.

$$\dot{\omega}_{vsm} = \frac{1}{2H}[P^*_{ac} - P_{ac} - k_d(\omega_{vsm} - \tilde{\omega}_g)] \tag{2.10}$$

$$V^*_{d,droop} = V^*_d + m_v(Q - Q^*) \tag{2.11}$$

As described above, the AC Power control performance can be specified for desired transient requirements. Nonetheless, the control tuning is defined based on the required dynamic support of the power converter response along the different operating conditions of the interconnected AC system; and it is restricted according to the time scale of the cascading control structure and available energy reservoir. Furthermore, the inertia constant will have implications on the converter and DC system, as the AC system support relies on these two subsystems due to control and physical interdependencies. Therefore, the requested inertia will bound quantities of the VSM standard parameters: the dynamic response of the power converter and, intrinsically, the following disturbance propagation from the converter to the DC system.

2.4.3 MMC internal protection

a) Converter current limiters

In contrast with synchronous machines, MMCs use IGBTs in their submodules to synthesise the desired output electrical signals, which have a limited overcurrent capability [64], [92]. Therefore, current limiters are embedded in the MMC control to manage the converter current output and avoid any possible damage to the power electronics devices.

In the GFL control strategy, it is common practice to use current limiters for each current component reference, allowing the prioritization of reactive or active current injection [85], [93], [94]. In these studies, the structure of the dynamic limiter implemented is given in 2.12 and 2.13, when giving priority to the AC current q-axis component.

$$| i^*_{q,sat} | = min(I_{max}, | i^*_q |) \tag{2.12}$$

$$| i^*_{d,sat} | = min(\sqrt{{I_{max}}^2 - {i^*_{q,sat}}^2}, | i^*_{d,sat} |) \tag{2.13}$$

In the case of the GFM strategy, the implementation of such a dynamic limiter would not be straight forward, as this limiter implies the use of a current reference, which is not inherent in the GFM cascaded control structure, see Figure 2.8. Thus,

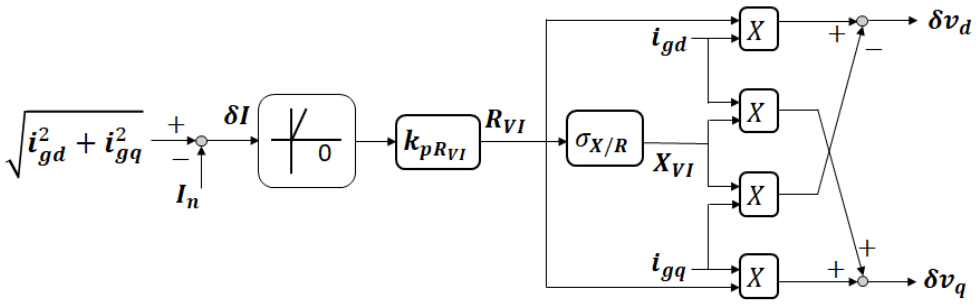


Figure 2.10: Virtual impedance current limiter implementation [82].

a modification of this cascaded control can be done for the integration of this current limiter in the GFM case, e.g., the current saturation algortithm (CSA) [85]. Yet, this approach loses the voltage source behavior of the power converter while activated.

A potential solution to this problem is the use of a virtual impedance, $Z_{virtual}$, which causes a virtual voltage drop in the AC cascading control when the defined current threshold is exceeded, as described in [85], [95]. This current limiter, depicted in Figure 2.10, has the advantage of maintaining the converter voltage source behaviour of the control strategy while activated, in contrast with other approaches [96]. The virtual voltage drop generated by the virtual impedance is then applied to the AC voltage d- and q-axis components when a defined current threshold is exceeded. The implementation of this limiter is given by (2.14), (2.15), (2.18) and (2.17).

$$X_{Z_{virtual}} = \begin{cases} k_{pR_{VI}}\, \sigma_{X/R} & \text{if } \delta\, I > 0 \\ 0 & \text{if } \delta I > 0 \end{cases} \tag{2.14}$$

$$R_{Z_{virtual}} = \frac{X_{Z_{virtual}}}{\sigma_{X/R}} \tag{2.15}$$

$$\delta v_d = R_{Z_{virtual}} i_{gd} - X_{Z_{virtual}} i_{gq} \tag{2.16}$$

$$\delta v_d = R_{Z_{virtual}} i_{gd} + X_{Z_{virtual}} i_{gq} \tag{2.17}$$

It is important to highlight that these current limiters are based on the AC current;

nonetheless, the current flowing through each of the MMC arms is composed of both AC and DC components, as given in (2.18), and identified in Figure 2.2. Therefore, these current limiters might be compromised in cases where the DC component has a significant increase together with the AC component. Yet, these issues are out of the scope of this research work, but could be further explored in future studies.

$$I_{arm} = \frac{I_{AC}}{2} + \frac{I_{DC}}{3} \tag{2.18}$$

b) Blocking functions

HBSM has no current-blocking capabilities; therefore, the protection of HBSM-based converter valves is implemented in practice by bypassing the entire submodule using thyristors and/or vacuum breakers via specific MMC protection functions, resulting in diode-rectifier behavior [97], [98], [99].

Therefore, internal protection mechanisms are integral to the MMC architecture, safeguarding the converter against operational threats such as overcurrent-driven failure [77]. In addition, different conditions may also lead to MMC blocking, such as under- or over-voltage conditions. Nevertheless, the main state of the MMC to be monitored is the arm current, and therefore, the over-current protection function is utilized in this research work.

2.5 MTDC protection

The core objectives of DC protection align with those of AC protection: to ensure reliable and secure system operation during contingencies or component failures. These objectives aim to minimize fault impact and component stress while guaranteeing human safety. Primary protection system requirements include reliability, sensitivity, robustness, selectivity, speed, and stability [100], [101], [102]. MTDC systems introduce greater protection complexity compared to point-to-point links. With more elements involved, the impact of an MTDC malfunction can propagate to the interconnected AC systems. Among various DC system disturbances, fault handling and ride-through

constitute a primary contingency, making DC fault protection a central challenge.

From the AC system perspective, the impact of any DC contingency must remain within acceptable margins and comply with existing requirements. In particular, the permanent loss of active power must comply with Frequency Restoration Reserves (FRR) of the corresponding bidding zone, e.g., 3 GW in mainland Europe, or 1.8 GW in the GB. Thus, DC protection strategies must be developed to meet these requirements [102].

2.5.1 DC faults

DC faults present unique characteristics that impose significant constraints on protection strategy design. The dynamic behavior of the DC fault current creates two primary challenges. First, the low inherent inductance of DC transmission systems results in an extremely rapid rate of current rise. Second, the DC fault current lacks a natural zero-crossing point [34]. The former challenge poses a direct risk to converter switching elements, which have limited overcurrent capability compared to synchronous generators. To protect these components, submodules are typically bypassed when arm currents exceed a predefined threshold—generally no more than twice the nominal continuous rating [103]. The latter challenge necessitates the use of fault suppression devices (FSDs), also known as DCCBs, to actively interrupt and suppress the fault current.

Different types of DC faults can occur, each with distinct impacts on the hybrid system. In particular, AC system stability—encompassing transient, frequency, and voltage stability—can be jeopardized. This is due to the temporary or permanent loss of active power infeed and reactive power support from the HVDC system, depending on factors such as fault type, location, DC grid topology, busbar redundancy, and the protection scheme. The outcomes generally fall into two main categories: a temporary or a permanent interruption of power supply, corresponding respectively to a temporary block or permanent blocking of the MMC converters. These potential conditions, categorized in Table 2.3, along with their estimated probabilities in Table 2.4, can serve as criteria for dimensioning frequency containment reserves (FCR) and FRR [104].

Table 2.3: Type of faults and failure rates [104]

Type of faults	Failure Rate
Line fault	3.5 f/100y/100km
Active fault on a DC breaker	1.5 f/100y
Busbar fault	0.74 f/100y/bay
Line fault + DC breaker failure	2*10-4 occ/100y/100km
Spurious Trip	1.4 occ/100y
Sympathetic Trip	1*10-4 occ/100y/100km
Busbar fault + DC breaker failure	1*10-4 occ/100y
Converter failure	3 occ/1y

Table 2.4: AC system criteria depending on fault probability [104]

Fault probability	AC systems criteria
High ($\sim 10^2$ occ/100y)	TS$\leq$ 1 WG (150m ms)/ PS $\leq$ 1 GW
Low ($\sim 10^0 - 10^1$ occ/100y)	TS$\leq$ 3 WG (150m ms)/ PS $\leq$ 2 GW
Very low ($\sim 10^{-3} - 10^{-4}$ occ/100y)	TS$\leq$ 3 WG (150m ms)/ PS $\leq$ 3 GW

2.5.2 DC switching devices

Two primary switching components are considered for DC protection: circuit breakers (recently termed fault separation devices, FSDs), which can interrupt fault currents; and residual current switches (RCS), capable of breaking small currents (on the order of a few amperes) and making current capability (under load) [102], [105], [106]. These components are used, in coordination with specific control actions, to define distinct protection strategies.

Regarding DCCBs, several technological concepts have been developed for DC systems: mechanical, solid-state (pure power electronic), and hybrid. Mechanical DCCBs consist of three main elements: a mechanical switch in parallel with a dissipation element or surge arrester capable of generating a transient interruption voltage (TIV), and a resonant circuit to force a current zero-crossing. This type of breaker offers very low conduction losses. Solid- state breakers replace the mechanical switch and resonant circuit entirely with power electronic switches. Hybrid breakers combine a mechanical path for low-loss steady-state conduction with a power electronic branch for rapid current interruption, thereby leveraging the advantages of both technologies [34], [105],

[107], [108], [109], [110].

Several designs have progressed to the prototyping, testing, and commercialization stages. For instance, within the PROMOTioN project [111], a mechanical circuit breaker prototype by Mitsubishi Electric, rated for 160–200 kV, achieved current interruption with a peak current of 16 kA and an opening time of 7 ms. A hybrid prototype tested by Hitachi ABB was rated for 350 kV and 20 kA fault current interruption with an opening time of 3 ms. A third mechanical DCCB prototype by SCiBreak was rated for 80 kV and a breaking current of 12 kA, with an operating time of 2 ms [34], [109]. The operational sequence of a DCCB is illustrated in Figure 2.11. More recently, a hybrid DCCB has been announced as an important technological achievement by two major companies, Siemens Energy and Mitsubishi Electric, integrating the advantages of fast-acting power electronics and low losses of mechanical DCCBs [112], [113].

For bipolar converter stations, a medium-voltage DC circuit breaker—also referred to as a metallic return transfer breaker (MRTB)—is used to transfer the neutral path current to a redundant conductor when operating the station in a monopolar configuration. This allows the station to be reconfigured without de-energizing the DC system. Beyond this primary function, this mature technology can also serve as a medium-voltage DCCB for the DMR and other applications [114], [115].

2.5.3 DC protection philosophies

Similar to AC protection [116], DC protection strategies are designed according to overarching protection philosophies. These philosophies are defined by the degree of selectivity achievable within the DC system, categorized as fully selective, partially selective, or non-selective [33], [34]. Each philosophy permits a different degree of fault impact propagation and employs a distinct set of protection components, such as DCCBs, passive fault current limiters, and switches. Consequently, the permissible fault impact [102] and associated costs serve as primary guidelines for defining a specific protection strategy.

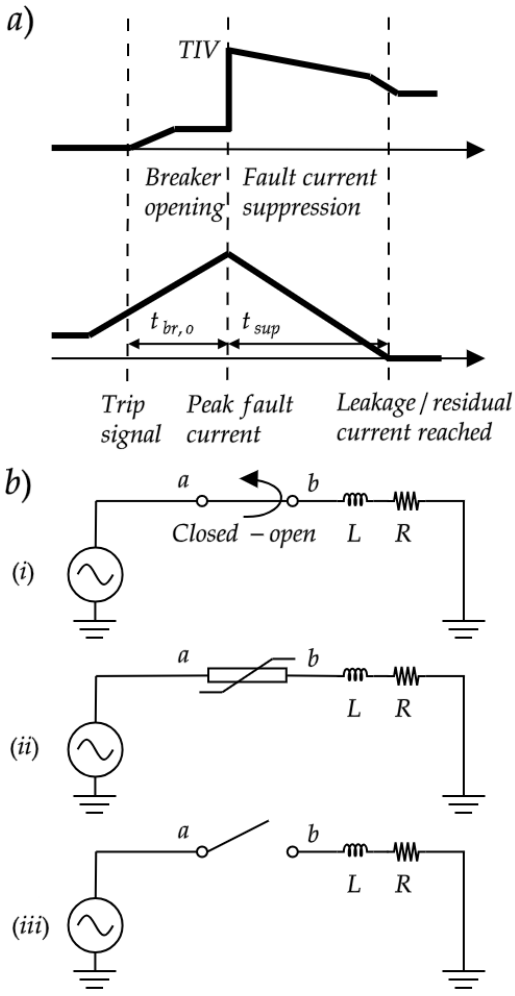


Figure 2.11: Fault current interruption process and timings [34]

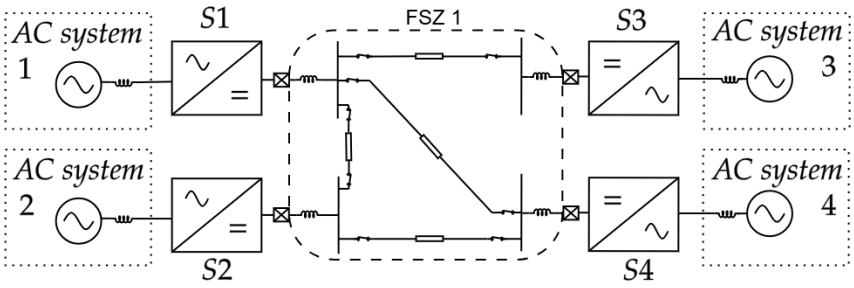


Figure 2.12: DCCB based non-selective protection strategy single line diagram

a) Non-selectvie protection philosophy

In the non-selective protection philosophy, the entire DC system is treated as a single protection or fault separation zone (FSZ) [35], [102]. Under this approach, a DC fault leads to the complete disconnection of the DC system, resulting in temporary power interruption and converter blocking. While point-to-point HVDC systems normally rely on AC circuit breakers (ACCBs), MTDC systems may employ DCCBs or fault-blocking converters to achieve system protection [117].

In practice, a solution combining DCCBs and ACCBs might be considered, as temporary blocking of MMCs is acceptable. This approach reduces costs by minimizing the reliance on DCCBs. Nevertheless, a protection scheme based exclusively on DCCBs can help to understand the MMC responses along the DC FRT, for example, control interactions, the propagation of disturbances between asynchronous AC networks and the DC system, and the resulting DC fault FRT performance, as depicted in Figure 2.12. Therefore, analyzing such a scheme is worthwhile to fully understand these impacts.

b) Partially selective protection philosophy

This protection philosophy separates the DC system into at least two FSZs. This way, the fault impact is mainly contained within one FSZ, preventing its further propagation across the entire system. Main criteria for establishing the FSZ includes: DCCB rating and fault current level at a given node, converter prioritization based on the relevance of its interconnected AC system, geographical characteristics, transmission system operator's (TSO's) control areas, DC grid topology characteristics, e.g., line length, or

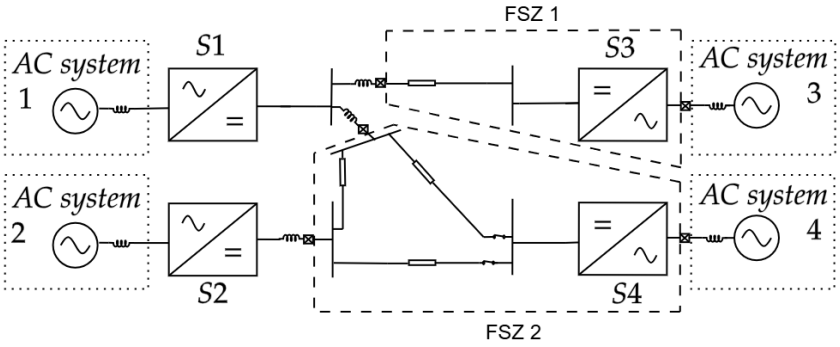


Figure 2.13: Partially selective protection strategy single line diagram

branch sections, and fault probability.

To reduce the DC fault impact on power converters generally requires the use of current-limiting devices, such as DC reactors (DCRs), which increase capital expenditure (CAPEX) and, due to their resistive losses, also contribute to operational expenditure (OPEX). In addition, each FSZ can itself be subdivided into nested fault isolation zones [30]. DC switches, ACCBs, or lower rating DCCBs can be used to develop proper fault clearing strategies for each isolation zone [102], [105], [118]. An illustration of DC system segmentation under this philosophy is presented in Figure 2.13.

c) Fully selective protection philosophy

In the fully selective protection philosophy, an FSZ is assigned to each individual transmission component, i.e., line or node, thereby minimizing the overall fault impact by largely confining disturbances within the affected zone. However, this high degree of selectivity requires a large number of main DCCBs and associated DCRs, making it the most expensive protection solution.An illustration of DC system segmentation under this philosophy is presented in Figure 2.14.

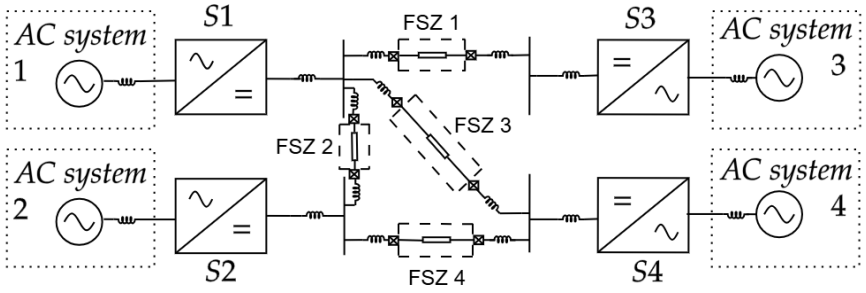


Figure 2.14: Fully selective protection strategy single line diagram

2.5.4 Generic DC protection sequence along system DC FRT

For the hybrid AC/DC system to achieve fault ride-through, the protection strategy must be closely coordinated with specific converter control actions. This coordination is essential to maintain both converter and grid operation within stability and safety operational margins throughout the fault sequence. The goal of this sequenced response is to enhance overall system resilience—that is, the system's ability to anticipate fault propagation, absorb or dissipate the disturbance, and rapidly recover to normal operation [26].

a) System resilience

The behavior of the system sequenced response towards the DC fault disturbance can be described from a high-level perspective by the resilience trapezoid in Figure 2.15, and thoroughly described in [119]. Each phase of the trapezoid emphasizes specific requirements for power system design and operation. During the pre-disturbance resilient state, studies should be conducted to identify potential event locations and assess their severity. These studies enable TSOs to plan, design, and operate the system proactively, allowing for preventive actions and the establishment of grid configurations capable of managing anticipated events effectively.

During Phase I (Disturbance Progress), the system's robustness, withstand capability, and redundancy determine the extent of the impact, defining a specific level of resilience degradation. Advanced monitoring, distributed energy storage, and appro-

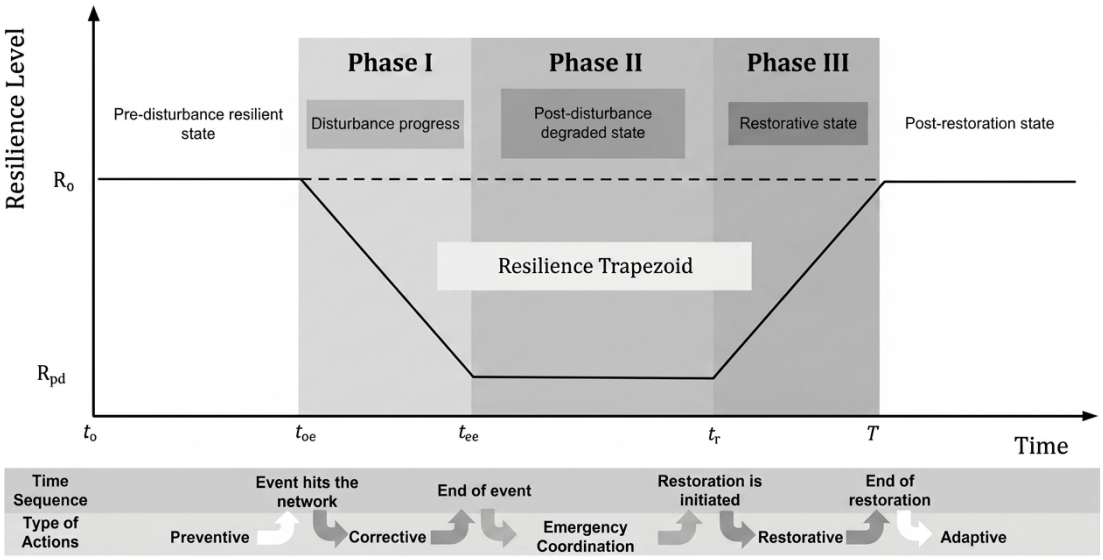


Figure 2.15: Resilience trapezoid: conceptual phases related to resilience of a power system [116].

priate protection strategies provide the operational flexibility needed to reduce the rate of this degradation.

In Phase II (Post-Disturbance Degraded State), impact assessment, prioritization, and preparedness measures facilitate the rapid identification of critical components, thereby accelerating the initiation of the restoration process. The objective is to minimize the duration of this stage.

Phase III (Restorative State) must be capable of restoring service to affected customers and rebuilding damaged infrastructure, requiring sufficient operational and infrastructural resilience. Actions in this phase include re-energizing transmission and distribution lines, repairing or replacing damaged components, restarting generation units, re-synchronizing network areas, and restoring load. The objective here is to have the smoothest restoration, avoiding the generation of a new perturbation in the system. The resilience cycle concludes with the Post-Restoration State. Here, the overall event impact and network performance are analyzed to identify system weaknesses and limitations. This analysis informs improvements to system design and operation for future events.

b) System DC FRT operation

While control strategies can enhance resilience, the extent, severity, and duration of a DC fault's adverse impact are primarily determined by the chosen protection strategy. Consequently, the system's degraded, restorative, and post-restoration states are fundamentally bounded by this choice. As established, the fully selective protection strategy minimizes overall system impact by ensuring rapid fault separation and confining the disturbance to the faulted unit. In comparison, partially selective strategies result in a larger impact, though its extent is limited by the definition of FSZs. The non-selective strategy, conversely, leads to the most significant impact, causing greater system degradation and prolonging the adverse operational condition.

Therefore, the chosen protection strategy directly determines the extent of the fault's impact on the system, and consequently, the achievable level of system resilience. In addition to the protection scheme, the control strategy of the HVDC converters critically influences the system's preparedness for potential disturbances. Therefore, the proper coordination of C&P strategies across all system operating conditions is essential for achieving a secure, pre-disturbance resilient state.

While the required coordination of C&P strategies varies with the selected protection approach, the overall DC FRT operation for the system will follow the general process outlined in the flow diagram of Figure 2.16 [93], [101], [120], [121]. To further detail the DC FRT operation and be able to start any study of this research, the following methodology is proposed, as depicted in Figure 2.17. An initial basic understanding of the issue is developed by defining a purpose. This is followed by the first analysis of the study core. With this basis, a test is designed, and a corresponding simulation model is developed. After running the simulation, the results obtained are processed and assessed; if results are satisfactory, findings and conclusions are drawn.

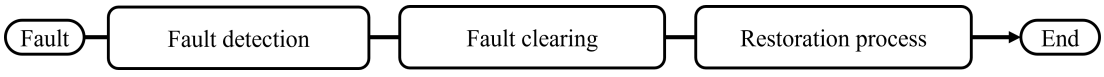


Figure 2.16: DC FRT flow diagram.

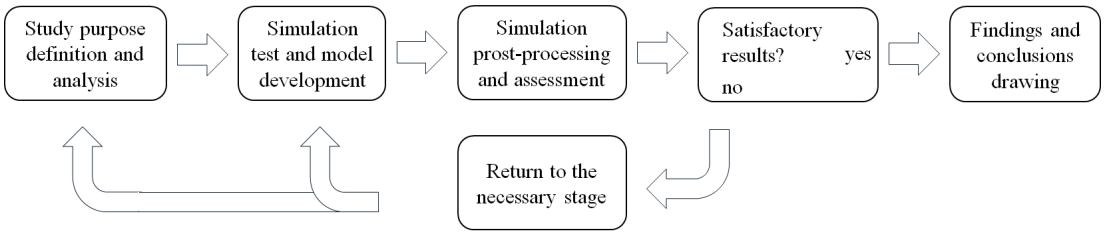


Figure 2.17: DC FRT flow diagram.

2.6 Summary

This chapter has presented the main concepts utilized in the rest of the thesis and outlined several hypotheses for the use of the presented concepts. It establishes the assumed hybrid AC/DC system models, hardware traits, and control frameworks that underpin the subsequent research in the thesis. It specifically bridges the two key design areas of DC systems, i.e., MMC control strategies and MTDC grid protection philosophies, building toward a comprehensive DC FRT methodology analysis.

The base hybrid AC/DC system architecture utilized throughout the work is considered to be a minimum mesh with bipolar configuration. Since the main focus of the studies is on the onshore stations, the OWFs representation in the developed simulation models is simplified, using a voltage source or current source representation. The MMC model is simplified in its arm representation, by means of the AVM, while an energy-based control philosophy is adopted integrated with the virtual capacitor concept. On the AC cascaded loop, the GFL and GFM strategies are considered for the evaluation of the MMC and system dynamic performance along the DC FRT. MMC protection function considering the arm current is employed, a virtual impedance is implemented in GFM to limit the MMC output current in the event of AC side disturbances. The three DC protection philosophies are discussed, with the non-selective and partially selective ones to be further studied. Finally, to start the studies performed throughout this research work, a main methodology has been presented.

Chapter 3

DC FRT considering non-selective protection strategy

3.1 Chapter introduction

This chapter introduces the system DC FRT and GFM response. Successful DC FRT operation requires proper coordination of C&P actions. Furthermore, this chapter presents a detailed assessment of MTDC system re-energization strategies, focusing on scenarios when interconnecting weak AC grids. Different approaches are compared to highlight their respective advantages and disadvantages, thereby providing insights into the design of suitable operational sequences.

This chapter focuses on the non-selective protection scheme, since this approach serves as a foundational introduction to the DC FRT system, the GFM response, and their broader system implications. Assessment of partially and fully selective protection schemes will be covered in Chapter 5.

3.2 System DC FRT with GFL control

A specific protection scheme is developed based on an established DC protection philosophy, which determines how each system element operates during a fault. Different schemes result in varying levels of system dynamics and DC fault propagation. For in-

stance, in a non-selective protection scheme, the whole DC system becomes temporarily unavailable for power transmission immediately following circuit breakers' opening. This characteristic permits the use of fewer DCCBs and DCRs with lower ratings. Furthermore, once a protection scheme's feasibility is confirmed, MMC control must satisfy all related circuit constraints, e.g., ensuring stability during normal operation and, specifically for the non-selective strategy, managing the absence of the DC system during a fault.

3.2.1 HVDC system under consideration

The DC system used for this scenario is represented in the single-line diagram shown in Figure 3.1. To concentrate on the C&P sequence and characterize the response of the onshore converters under the proposed control strategies during DC FRT, the system simplifies the OWFs or power park modules (PPMs) and the interconnected AC systems. Specifically, the PPMs are represented as infinite buses connected to GFL converters operating in either Vdc-P droop (for the strong grid scenario and GFM introduction) or P-mode (for the weak grid scenario). On the onshore terminals, the interconnected AC bulk systems are modelled using Thévenin equivalents, enabling the variation of grid strength at the point of common coupling (PCC) or point of connection (PoC). No DMR is used throughout the DC system; instead the bipole converter stations use a ground return.

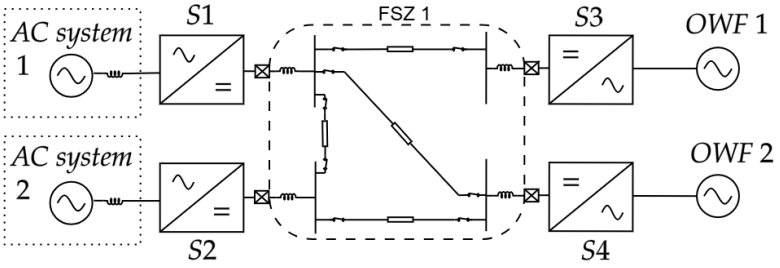


Figure 3.1: AC-DC system single line diagram with a DCCB-based non-selective protection scheme

3.2.2 Study methodology

To establish a general understanding of DC FRT and to provide a benchmark for later studies, the interconnected AC systems are modelled as strong grids. The reference scenario is developed with every station in the MTDC system operating under GFL control. This configuration is used to provide a broader understanding of DC FRT operation of an MTDC system, since the topic has been well-analyzed for point-to-point systems in the literature through both analytical approaches [122] and offline EMT-type simulations [123].

The proposed protection strategy defines the essential conditions for the system to ride through the DC fault, i.e., the temporary loss of the MTDC grid and the temporary blocking (TB) of the MMCs. Consequently, the temporary loss of power infeed is determined by two main stages of the DC FRT, namely, the fault clearing and the restoration process [59], [120]. Operating these stages requires coordinated C&P actions to maintain MTDC grid stability and ensure operation within safe margins. The specific sequence of C&P actions depends on the given hybrid system characteristics and available protection equipment. In this work, a simplified generic framework is used to facilitate the identification of key phenomena during system DC FRT under a non-selective protection strategy.

To analyze the system-level dynamic performance of the MTDC grid, the DC FRT process is divided into two phases: fault clearing and system restoration. For illustrative purposes, a generic C&P sequence depicted in Figure 3.2 is adopted. The fault clearing phase spans from MMCs' blocking, going through the DCCB opening, until the faulty unit (e.g., a faulty cable section) is isolated, see Figure 3.2, instants 2, 3 and 4, respectively. The restoration process begins with the de-blocking of the MMC, instant 5, to initiate STATCOM operation, instant 6. This is followed by the breakers reclosing, instant 7, allowing the MTDC reenergization by means of the DC voltage restoration, instant 8, until pre-fault power flow is restored, instant 9. The detailed processes of converter de-blocking and MTDC grid re-energization will be covered in a dedicated subsection, where different strategies are examined in the context of a weak grid scenario. Therefore, the present section provides only a general overview of the

system DC FRT operation.

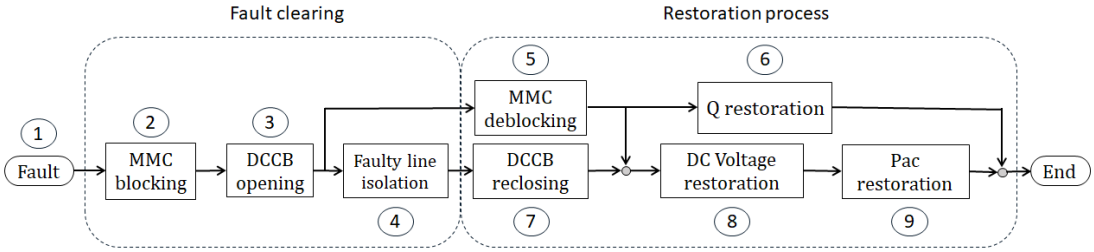


Figure 3.2: DC FRT C&P generic sequence with a DCCB-based non-selective protection strategy.

Regardless of the selected control strategy, once the DCCBs open, the DC grid becomes unavailable and can no longer support the regulation of the MMC's internal energy. Consequently, the use of the DC system and original droop strategy, which are implemented to manage MMC internal energy and MTDC voltage, respectively, becomes ineffective. Therefore, dedicated controllers must be activated to regulate the converter energy and DC voltage.

A simple shift of the energy control reference to the AC cascaded control loop is insufficient, as the inner current control dynamics constrains the permissible response time of the energy controller. The dedicated de-blocking (DD) energy controller (DDEC) is channelled through the AC cascaded control loop, and is tuned to respect the response time of the following controllers in the cascaded loop; its integration in the MMC cascaded control (presented in previous chapter Figure 2.7) is depicted in Figure 3.3. Concurrently, a dedicated de-blocking DC voltage (DDVC) control is implemented to ensure the MMC DC voltage remains within a safe operating range. DDVC uses the MMC equivalent capacitance, $C_{dc,eq}$, which accounts for the submodule capacitors of the converters. Its transfer function, given by (3.1), is used for controller tuning [87]. In this work, the associated time constant is defined on the order of 10^{-2} s.

$$G_{VdcM}(s) = \frac{v_{dc}}{v_{dc}^{*}} = \frac{k_p^{VdcM} s + k_i^{VdcM}}{C_{dc,eq} s^2 + k_p^{VdcM} s + k_i^{VdcM}} \tag{3.1}$$

The role of both the DDEC and DDVC during the restoration process can be further

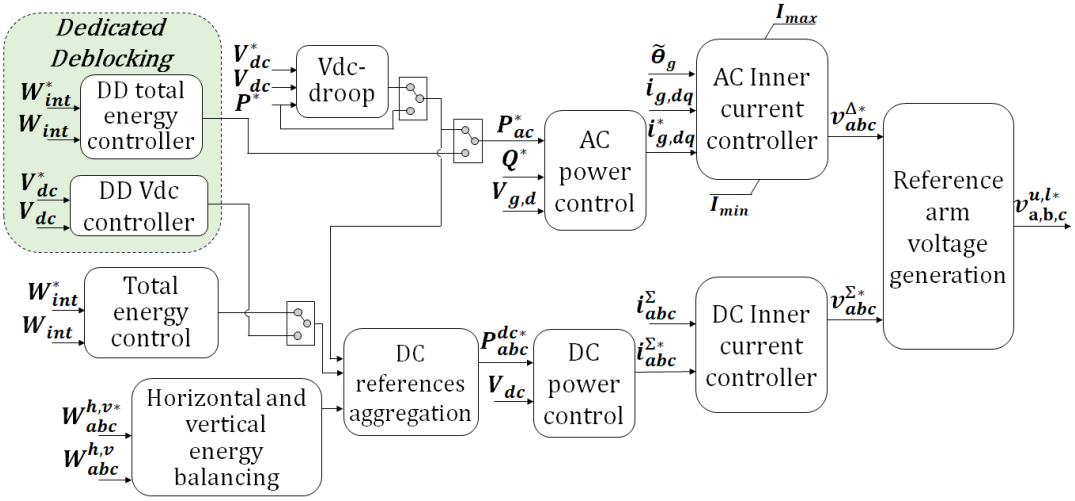


Figure 3.3: MMC GFL control architecture, where the dedicated control to perform the DC FRT is highlighted.

explained by reviewing the cascaded control structure shown in Figures 3.4 and 3.5. After the opening of the DCCBs, switches sw_1, sw_2, and sw_3 are moved to their second position. This configuration adjusts the AC-side power flow to regulate the MMC's internal energy while a temporary Vdc-master controller in each converter regulates the DC voltage at the converter terminal with a fast response, only slower than the inner DC current controller, in this case a response time of 30 ms is selected due to the good performance it presents, as shown presented in the following sections. After the reclosing of the DCCBs, the Vdc-master controller in each MMC is disabled to prevent control conflicts between stations S_1.

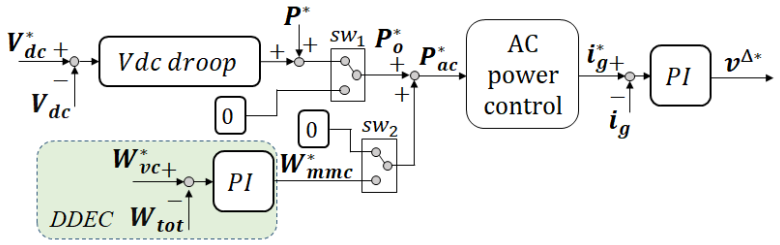


Figure 3.4: Dedicated de-blocking energy control - detailed view.

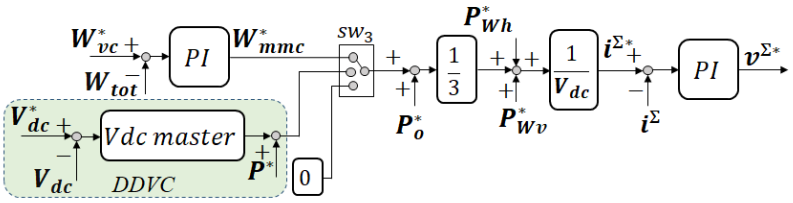


Figure 3.5: Dedicated de-blocking voltage control - detailed view.

3.2.3 Reference scenario

In order to have a proper comparison between GFL and GFM strategies, the same operating mode should be used. Moreover, as an introductory chapter, GFM strategy is implemented in the MMC cascaded control in its simplest form. Therefore, in this chapter, converter station S_1 operates in P-mode. This control mode disregards the MTDC voltage state, delegating the DC voltage regulation task to the other converters in the grid. Consequently, converter stations S_2, S_3 and S_4 are dedicated to regulating DC grid voltage; whilst S_1 remains in P-mode.

To better track each stage of the system DC FRT, the C&P sequence in Figure 3.2 is enumerated. Each stage of this sequence will be adapted per case study throughout the thesis to aid clarity. For the simulations, the active and reactive power operating points for stations S_1 and S_2 are set to 600 MW and 400 MVAr, respectively, reflecting power inversion from the MTDC supplied from OWF production. A DC fault is applied at the midpoint of the transmission cable connecting S_1 and S_2 at 2 s of simulation.

Figure 3.6 depicts the voltage profile of the faulty pole in the MTDC grid during the DC FRT sequence. Upon fault inception at 2 s (instant 1), DC voltages of the faulty pole collapse rapidly. Approximately 3 ms later (instant 2), the converter arm overcurrent protection triggers the blocking of all converters, having minor differences in blocking time due to the different electrical distance to the fault location, as shown in Figure 3.7. This action bypasses the power submodules and prevents their further discharge into the fault.

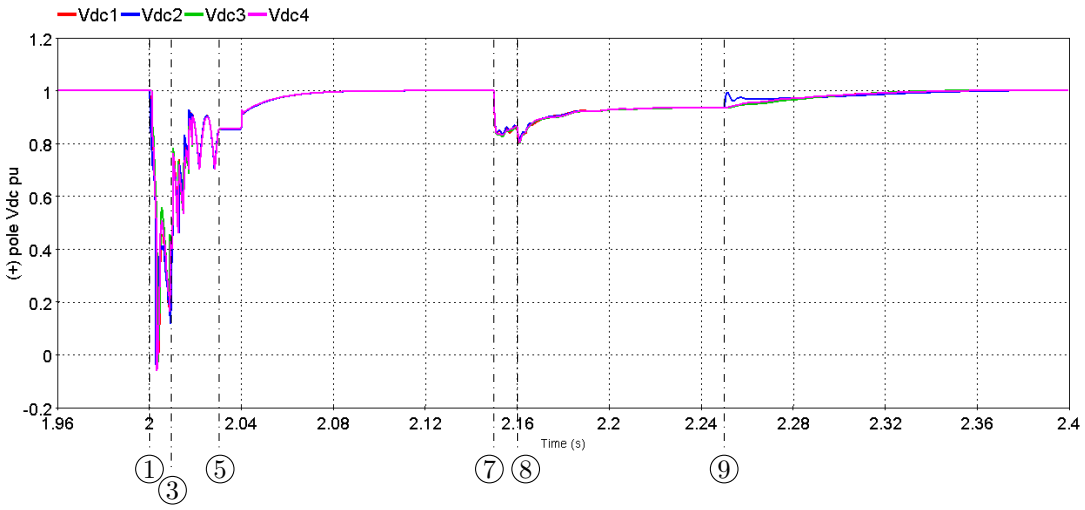


Figure 3.6: MTDC system faulty pole DC voltage profiles measured at the converter terminals- reference case

Once the MMCs are blocked, large fault currents from the AC sides feed into the fault location, resulting in negative active power as observed in Figure 3.6 (where positive power corresponds to flowing from DC to AC). DCCBs are opened at 2.01 s (instant 3). High-frequency oscillations persist in both DC voltage and active power until the fault current is suppressed, approximately 18 ms after fault inception. Following fault neutralization and current suppression, the active power returns to zero, as shown in Figure 3.7.

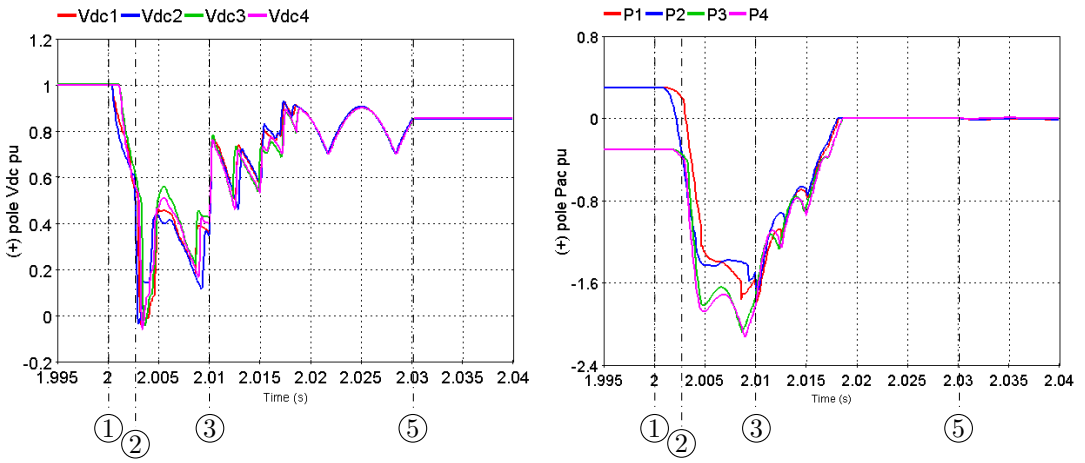


Figure 3.7: MTDC system fault transient DC voltage and active power profiles - reference case

The zoomed-in DC voltage view on the left-hand side of Figure 3.7 reveals in greater detail all MMCs' faulty poles. Stations S_3 and S_4 present a later drop in comparison to stations S_1 and S_2, as the travelling time of the first travelling wave that reached each station is longer. In all cases, the voltage drop is reshaped by the converters' blocking (instant 2), and later by the fault current, driven by the complex behavior of the system at the AC PoC, including interactions with the healthy pole converter in GFL control. The characteristic open-circuit diode rectifier voltage is identified, which persists until the converter is de-blocked at 2.03 s (instant 5).

On the right-hand side of the same Figure 3.7, the active power profiles of all faulty pole MMCs of the MTDC grid are depicted. After the fault inception, for the converters inverting power, the output power is first reduced to zero, and later turned negative, flowing into the MTDC system towards the fault location. While power from the offshore grid fed into the MTDC system is similiarly increased. After all DCCB are open, the fault current is neutralized and fully discharged, as described above, leading to a zero power throughout the hybrid system. At 2.03 s, all MMCs are deblocked, and a rather small transient is identified due to the re-insertion of the MMC power submodules, which are recharged by taking energy from the AC system.

Following a 10 ms delay after the MMC is deblocked, the DDVC assumes regulation of the MMC DC voltage, as seen in Figure 3.6. The faulty section is isolated after the DC grid discharges and the associated DC switches open (instant 4). When reclosing the DCCBs at 2.15 s (instant 7) DC current is pulled from the MMCs in the faulty pole, causing a transient DC voltage drop at the converter terminals. This sequence of events—converter de-blocking, DC voltage and internal energy regulation, and DCCB reclosing—generates a minor power transient, which is barely discernible on the right-hand side of Figure 3.7 and Figure 3.8.

DC voltage returns to its nominal level after the Vdc-P droop control is reactivated at 2.25 s (instant 8). This reactivation causes a significant power transient in stations S_2, S_3 and S_4 as shown in Figures 3.6 and 3.8. Finally, once the MTDC grid is fully re-energized, the voltage stabilizes at its nominal level. The pre-fault power flow is restored via a 300 ms ramp starting at 2.40 s (instant 9), as visible in Figure 3.8 where

the complete system DC FRT is depicted from the AC power perspective.

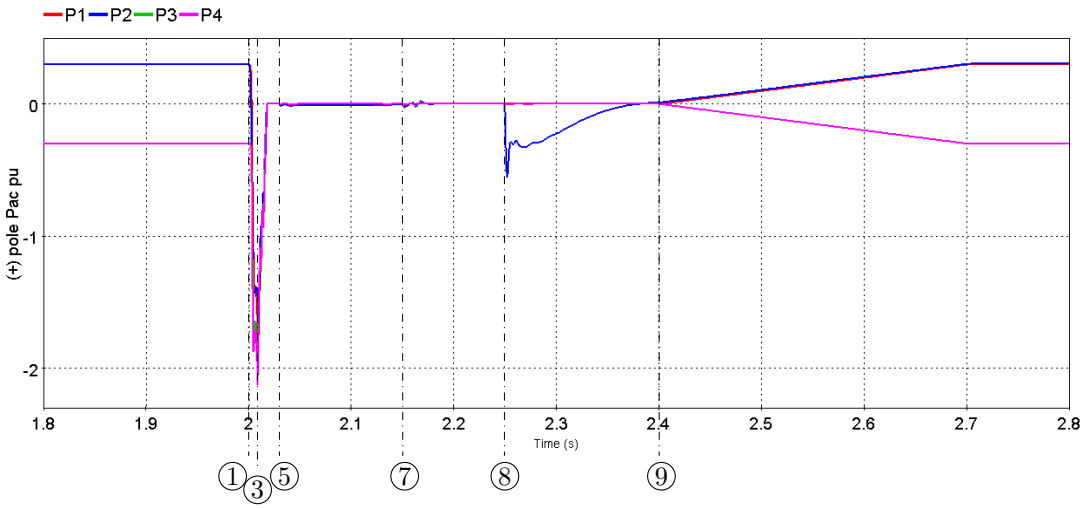


Figure 3.8: MTDC healthy pole active power profiles - reference case

The internal energy of the MMCs during the DC FRT is depicted in Figure 3.9. As highlighted in the previous chapter, this state parameter is fundamental for MMC operation. After the fault is incepted at 2 s (instant 1), the MMC submodules begin to discharge as DC current feeds into the fault through the MTDC grid. Once the overcurrent reaches the 1.5 pu threshold, the MMC submodules are bypassed, halting further discharge. Differences in electrical distance from each converter to the fault lead to different blocking instants, though these differences are small throughout the MTDC.

Following converter de-blocking at 2.030 s (instant 5), onshore converters' DDEC activates, enabling MMC internal energy regulation despite the unavailability of the MTDC grid; whilst the offshore converters have a rather slow discharge without any energy source to support their standby operation. Once the DCCBs are reclosed at 2.150 s (instant 7) the converter experiences a partial discharge due to the lower DC voltage level of the MTDC. At 2.250 s, the Vdc-P droop is reactivated, enabling the re-energization of the MTDC and MMCs. A final small transient, lasting a few hundred milliseconds, occurs after the pre-fault power flow is restored. This corresponds to the DC voltage settling according to the virtual capacitor reference and the Vdc-P droop.

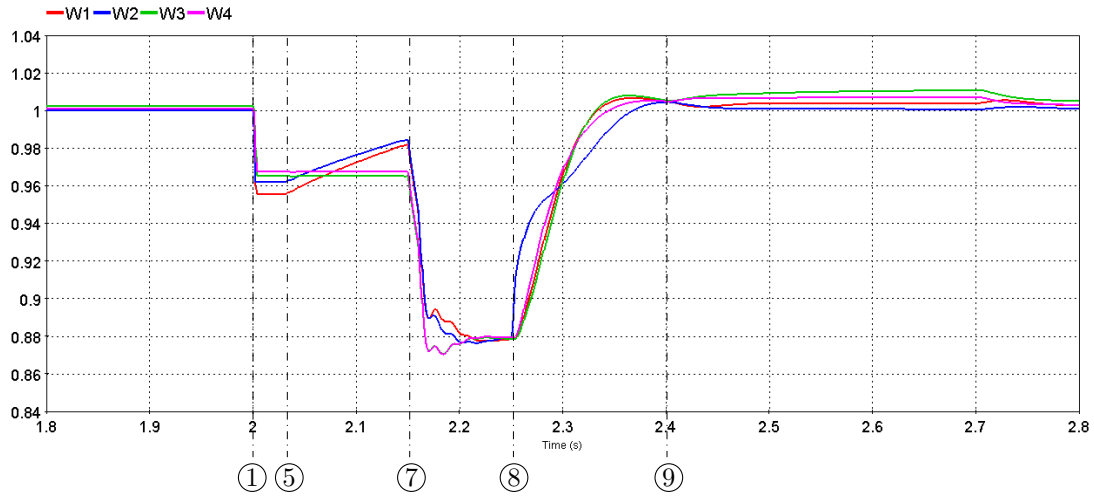


Figure 3.9: MTDC faulty pole internal energy profiles - reference case

Figure 3.10 top graph depicts reactive power profiles of the onshore stations S1 and S2. Similar to active power, reactive power is dominated by the fault current behavior after fault inception at 2 s (instant 1), until the fault current is neutralized. The deblocking transient at 2.03 s (instant 5) is also identified, as it causes a small AC disturbance impacting AC voltage, and consequently, the MMC control reference frame through PLL action. 100 ms after the MMCs' deblocking, STATCOM operation with constant Q is started (instant 6) at 2.130 s of simulation.

Figure 3.10 bottom graph shows the AC voltage amplitude at the PoC, or PCC, for converter stations S_1 and S_2, represented in red and blue, respectively. The DC FRT operation is also reflected in the AC voltage at each converter's PCC, as shown in this figure. Following the MMCs' blocking approximately 2.003 s (instant 2), the voltage amplitude drops significantly, with subsequent high-frequency oscillations linked to the complex dynamics of the fault current. A minor transient occurs after the faulted MMC is de-blocked at 2.03 s (instant 5), due to the reinsertion of the converter's equivalent submodule capacitance, and the use of the DDEC to handle the MMC internal energy, as observed in previous figures.

AC voltage amplitude recovers to its pre-fault level at both stations only after the MMC's reactive power output is restored to its pre-fault condition—that is, when capacitive support is resumed at the PCC. A significant difference arises at 2.250 s when

the Vdc-P droop is reactivated at S_2 (instant 8). This causes a new power transient at the PCC, and the resulting voltage disturbance settles after a few hundred milliseconds.

A more detailed view of the initial fault transient is depicted in the zoom-in on Figure 3.11. Although both equivalent power systems connected to S_1 and S_2 are strong (with a short-circuit ratio, SCR, greater than 3— equal to 5 in this reference scenario), differences are observed due to the MMCs' control characteristics. The use of Vdc-P droop control at S_2 results in a faster impact on the interconnected AC system, when compared with that of S_1, as the droop control immediately draws power from the AC system once the DC voltage begins to drop.

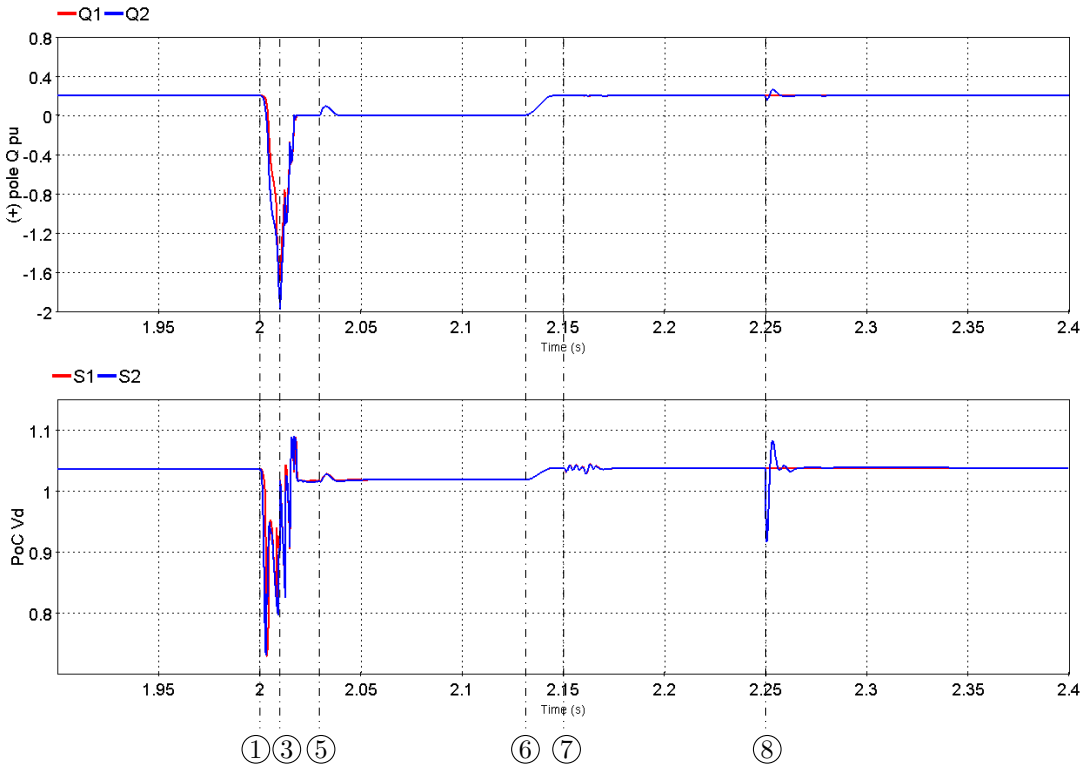


Figure 3.10: MTDC healthy pole reactive power profiles and AC voltage amplitude at the PoC- reference case

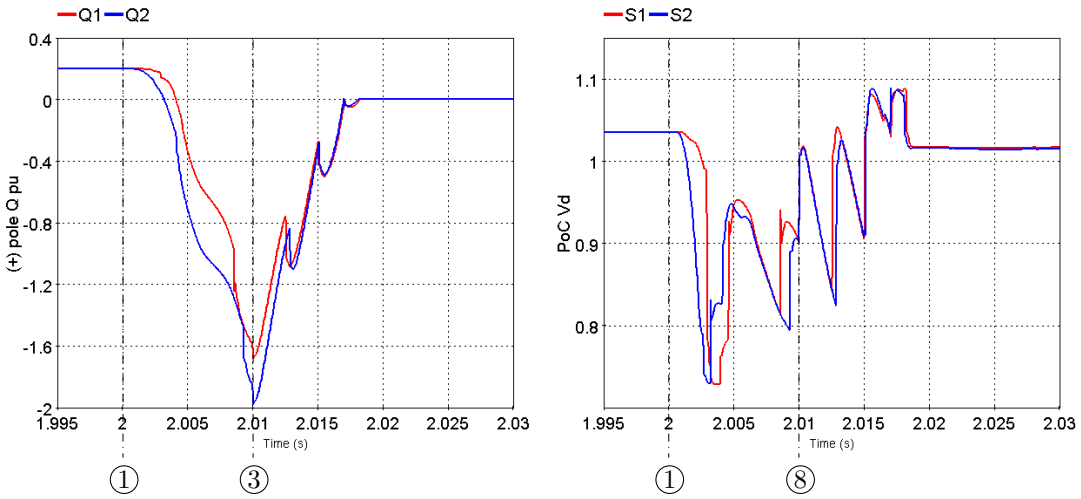


Figure 3.11: MTDC healthy pole reactive power profiles and AC voltage amplitude at the PoC- reference case zoom-in

3.3 Interconnection to a weak AC grid and the MTDC grid re-energization

The DC FRT operation has now been reviewed and understood for the reference scenario. Next, the condition of the interconnected AC system is varied to reflect a scenario of reduced grid strength, as might occur in bulk power systems in the case where the grid strength is reduced, e.g., if scheduled maintenance or faulted grid sections are found, implying the disconnection of certain main lines, and/or power generation is dominated by IBRs controlled with the GFL strategy, or the converter station is integrated to the AC system through a long tie line [49], [124]. This weak-grid scenario is characterized by reduced voltage stiffness, identified by a short-circuit ratio (SCR) below 3 at the MMCs' PoC [53]. To illustrate this condition, the SCRs of the interconnected AC systems at stations S1 and S2 are both set to 1.5.

As already identified, two main power transients are encountered along the system DC FRT: first during the fault clearing and the second along the MTDC grid re-energization. These two major disturbances could compromise system operation under weak grid conditions, as voltage oscillations are likely to propagate —similar to what occurred during the recent blackout in the Iberian Peninsula [49]. The risk stems from

the fact that GFL converters operate essentially as current sources; they rely heavily on a stable grid voltage to track system frequency and inject the specific current required to deliver their target output power [53], [125].

Consequently, the system DC FRT operation should be as smooth as possible, minimizing the transients' magnitude, especially their impact on AC voltage variations, due to its operational importance for the MMCs using the GFL strategy. While the fault transient is largely constrained by protection speed, leaving limited flexibility for its mitigation once a protection scheme is selected, the re-energization transient offers a larger scope for improved performance. During this phase, DC cables and converters are recharged by power injection from the AC to the DC side via the MMCs, which act as the controlled interface between the two systems. However, the converters' ability to manage this power exchange is limited by their operational ratings and the controller's capacity to maintain energy balance.

Several strategies for re-energizing the DC system have been explored in the literature. For example, reference [126] studied monopole DC re-energization as part of an AC black-start process using offshore OWFs, a method inherently limited by the availability of the renewable energy source. Reference [127] proposed utilizing internal capacitors within DC circuit breakers (DCCBs) for re-energization; this avoids AC system constraints but at the cost of increased breaker complexity. Reference [128] investigated re-energization in MTDC systems by employing a single converter for DC voltage regulation, without considering droop-based approaches or implications for weak grid conditions.

Therefore, this section reviews and compares two re-energization strategies under weak grid conditions: the use of Vdc-P droops and a Vdc-master controller, specifically under weak grid conditions. Furthermore, in this subsection, stations S1 and S2 are in charge of regulating the MTDC voltage by means of Vdc-P droops, while S_3 and S_4 are in P-mode. Furthermore, the PLL natural frequency is increased 5 times, and the internal energy controller response time is accelerated to 30 ms, allowing faster corrections to the MMC originated by unbalances linked to power output errors, given the low voltage stiffness at the AC.

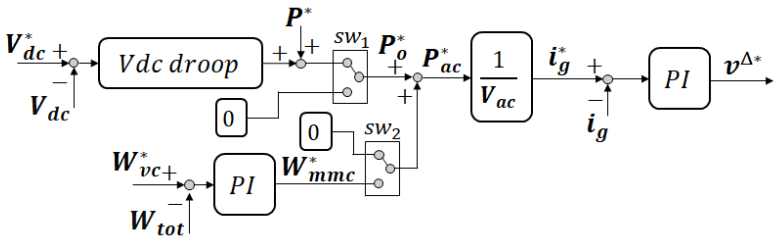


Figure 3.12: GFL AC cascading control loop and reconfiguration during DC-FRT operation.

3.3.1 Re-energization strategies

Once the fault is isolated, the restoration process can begin. The re-energization sequence is determined by the selected control strategy, each approach requiring a specific order of control activation. To clarify this process, Figures 3.12 and 3.13 present a detailed overview of the AC and DC GFL high-level control structures for stations S_1 and S_2. Proper sequencing of this control architecture is essential to avoid conflicts among AC-side power, DC-side power, and total internal energy regulation. This requirement applies both during normal operation and throughout the DC FRT process. During the restoration process, the energy control is coupled to DC voltage dynamics via the virtual capacitor loop. Consequently, to properly manage the re-energization, the virtual capacitor must be disabled in converters that supply power from the AC system to the DC grid. This is achieved by setting $k_{vc} = 0$ in (2.3), thereby fixing the reference of the energy controller.

Additionally, because the DC grid is at a depleted charge level, the use of AC power to control MMC internal energy simply continues during the re-energization process. The DDEC is used as presented in previous subsections. This ensures that internal energy regulation is supported entirely by the AC system during the restoration process.

a) Strategy I - DC grid re-energization using Vdc-P droop control

In this strategy, the DC grid is re-energized through coordinated Vdc-P droop control between both converter stations S_1 and S_2, as part of the DC FRT. As in previous case

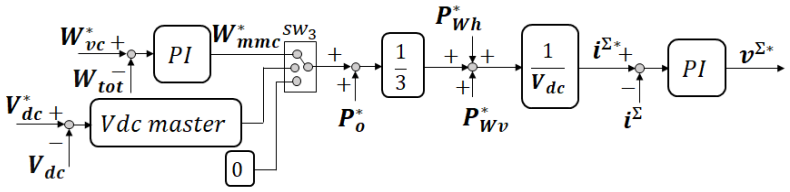


Figure 3.13: GFL DC cascading control loop and reconfiguration during DC-FRT operation.

studies, after fault clearing and MMC de-blocking, the internal energy and DC voltage of each converter must be stabilized. To initiate this process, switches sw_1, sw_2 and sw_3, are shifted to their second positions at 2.030 s of simulation. This configuration enables AC-side power flow to regulate MMC internal energy, while the Vdc-master regulates the DC voltage with a 30 ms response time.

Once the DCCBs are reclosed, an initial transient—attenuated by two pre-insertion resistors—occurs and settles after the resistors are bypassed at 10 ms and 20 ms, respectively. Following this, the Vdc-master control is deactivated at 2.250 s by shifting sw_3 to its third position. Simultaneously, the droop controllers at both S_1 and S_2 are activated by switching sw_1 to its first position. This allows the converters to jointly restore and regulate the DC voltage. Once the DC grid reaches its nominal voltage and is fully energized at 2.300 s normal operation is restored by returning switches sw_2 and sw_3 to their initial positions.

b) Strategy II - DC grid re-energization using Vdc master control (Station 2)

In this strategy, station S_2 alone is responsible for restoring the DC grid voltage using a Vdc-master control throughout the entire re-energization process. The initial sequence remains similar to Strategy I until the DCCBs are reclosed. In contrast to Strategy I, the Vdc-master controller at S_2 remains operational following the reclosing sequence. By slowing down the Vdc-master response time from the order of 10^{-2} to 10^{-3} s, it assumes primary responsibility for the restoration of the complete DC system voltage. This approach enables DC voltage regulation to be handled by a single converter.

At station S_1, two different approaches could be taken: 1) use the AC system to manage its internal energy during the MTDC grid re-energization; or 2) use the DC side to re-energize, increasing the stringency on the other converter. In this work, the second alternative is tested. Once the DCCBs are reclosed, switches sw_2 and sw_3 are returned to their initial positions. This allows the converter to use the re-energized DC grid to balance its internal energy. Once the DC voltage reaches its nominal value, S_1 also restores its droop control by switching sw_1 back to its original position at 2.400 s, thereby completing the transition to steady-state operation.

3.3.2 Re-energization strategies comparison

To analyze and compare the two re-energization strategies, the focus is placed on converter station S_2. When the Vdc-P droop strategy is used, the behavior at station S_2 resembles that of other stations employing the same strategy, control parameters and AC grid conditions; in the Vdc-master strategy, however, only S_2 converter performs the re-energization task. A sensitivity analysis of three electrical signals is used to compare both re-energization strategies: AC voltage amplitude estimation, or its d-axis component, Vd, at the PoC, followed by faulty pole active power and DC voltage during the stages of the restoration process after the MMC deblocking.

Figure 3.14 depicts the use of the Vdc-P droop and Vdc-master controls, on the left-hand and right-hand sides, respectively. The droop percentages used are: 5%, 10% and 25%; while the response time to tune the Vdc-master controller are: 0.5 s, 0.7 s and 0.95 s. These values allow a comparison of slow, intermediate and fast re-energization processes.

Following the generic C&P sequence in Figure 3.2, once the faulty pole converter is deblocked, STATCOM operation is initiated at 2.130 s (instant 6), giving voltage support at the PoC, avoiding any under voltage issues when restoring the pre-fault power flow [53]. In this work, a fixed constant value is used for illustration purposes, but this process can be designed based on the AC system operating characteristics and using a dynamic response, e.g., a Vac-Q droop. At 2.210 s (instant 7), DCCBs are reclosed, using two pre-insertion resistors closing 5 and 10 ms afterwards.

The potential between the MMC and the partially discharged MTDC grid leads to a discharge of the MMC once the breakers are reclosed. This is clearly reflected in DC voltage, which has a drop. In the case of the Vdc-P droop, as no other control action is taken, the voltage drop is slightly recovered by closing the bypass switch of one PIR. The bypass of the second PIR causes a small drop, again reaching 0.9 pu. DC voltage then increases to meet a new equilibrium corresponding to the MTDC grid state.

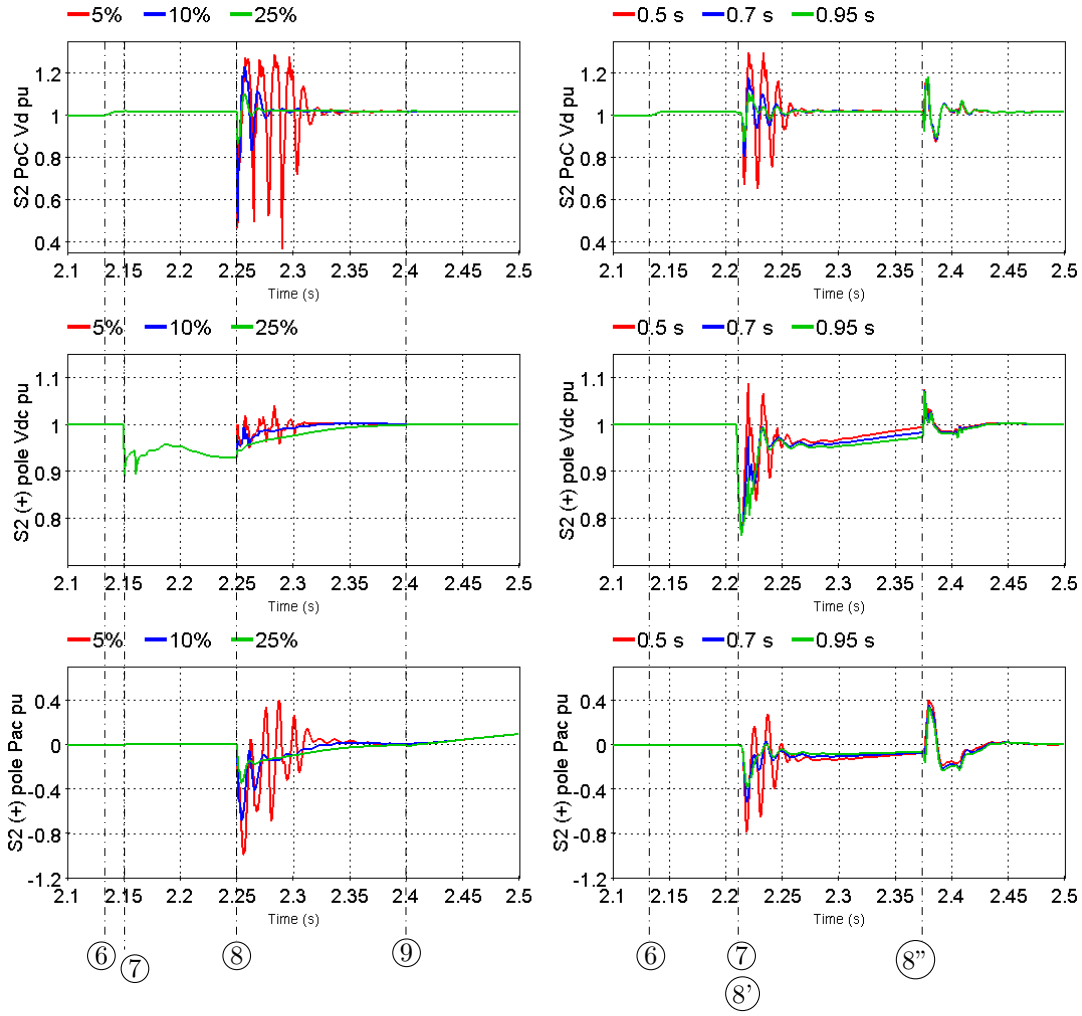


Figure 3.14: PoC Vac magnitude, S_2 faulty pole DC voltage and active power profiles - re-energization strategies comparison

The activation of the Vdc-P droop is done at 2.250 s (instant 8), taking power from the weak grid and injecting it into the MTDC grid to fully re-energize the DC system.

This power request causes a disturbance on the AC system. Depending on the droop percentage the perturbation produces a drop of AC voltage magnitude, reaching values of around 0.87 pu for the 25% droop to 0.5 pu for the 5% droop, continuing with high-frequency oscillations, reaching a value above 1.1 pu to 1.2 pu before settling down, once the DC voltage level is recovered around 100 ms after the droop activation. DC voltage is also affected; nonetheless, the main impact is taken on the AC side. Pre-fault active power is then ramped up at 2.400 s (instant 9).

The right-hand side of Figure 3.14 shows the use of Vdc-master control to re-energize the MTDC grid. Similar to previous case, at 2.130 s STATCOM operation is initiated (instant 6). DCCBS reclosing is done at 2.210 s (instant 7), with the simultaneous retuning of the Vdc-master controller (instant 8'). In this case, an AC power perturbation occurs upon the DCCBs reclosing, as the Vdc-master is active from the MMC deblocking and is kept active. Nevertheless, in comparison with the use of the Vdc-P droop, the power disturbance at the AC PoC is better handled, as the power exchange among systems is better controlled. Vd practically drops down around 0.87 for the 0.95 s to 0.66 pu for the 0.5 s response time, followed by oscillations with overshoots crossing 1.2 pu in the case of the fast re-energization. This time, the DC system faces a larger drop, reaching almost 0.75 pu; yet in each case, from slow to fast controllers, the oscillations are settled after around 50 ms. The Vdc-P droop is switched back at 2.375 s (instant 8"), presenting another transient, which settles after 10 ms, requiring further analysis. Therefore, active power restoration is delayed and not depicted.

From these results, it is corroborated that the weak grid is rather sensitive to any power exchange, disregarding the followed re-energization strategy. However, the sensitivity analysis showed that impact on the AC system was reduced when utilizing the Vdc-master control: AC voltage oscillations were quickly damped even with fast control tuning. Furthermore, the use of a single converter station to re-energize the MTDC system, gives the possibility to the operator to choose among the different AC systems to select the most appropriate one, reducing the perturbation of more AC systems for this task. Beyond this advantage, a second power transient has been identified

when utilizing the Vdc-master controller. This is discussed in the next subsection as a smoother re-energization is expected. In the case of the use of the Vdc-P droop, a high percentage depicts a reduced impact in both systems, similar to the slow Vdc-master controller; nonetheless, the use of Vdc-P droops allowed for a faster active power restoration. Moreover, when compared with the fast Vdc-master control, the large oscillations caused by the Vdc-P droop re-energization strategy took a longer period to settle.

3.3.3 Smooth re-energization with a Vdc-master controller

Previous subsection presented the advantages and disadvantages of both re-energization strategies. The Vdc-master controller demonstrated better controllability compared to Vdc-P droop activation, as it reduced perturbations on the weak grid. Furthermore, it concentrates the MTDC grid re-energization impact on a single AC system, thereby minimizing the overall disturbance within the hybrid system. However, another power transient was observed when switching back from the Vdc-master controller to the Vdc-P droop, underscoring the sensitivity of the weak grid to power disturbances.

To better understand this final transient and the corresponding responses of the MMC during this control switch, the interval between re-energization and the switch-back from the Vdc-master controller to the Vdc-P droop was extended, allowing the dynamic response to settle down. For this purpose, three main control signals are analyzed: DC voltage, MMC internal energy, and active power.

The purpose of analyzing these signals is to identify which controller drives the MMC response, and how it unchains the further interaction with other controllers, leading to the final perturbation of the AC system. From Figure 3.14, it is seen that the slow Vdc-master takes a longer time to fully re-energize the MTDC grid within the proposed 400 ms. Therefore, when changing back to the Vdc-P droop control, the fast droop action leads to a new power transient. On the other hand, the MMC energy level would be different from its DC terminal voltage, causing a new transient when the fast energy controller is channeled to the DC cascaded control loop of the MMC, as this controller uses the virtual capacitor concept, attempting to match the DC grid

charging level.

Results are presented in Figure 3.15. On the left-hand side, DC voltage, MMC internal energy, active power and PoC voltage amplitude at station S2 during the extended re-energization sequence and transition from the Vdc-master to Vdc-P droop control are depicted. On the right-hand side, a zoom-in of the same signals at the moment of switching back the Vdc-P droop is presented. As expected, the longer period for the MTDC grid re-energization allows for the settling of the dynamic response of the MMC. The slow Vdc-master controller takes around 1.7 s to re-energize the MTDC grid as can be seen in MMC DC voltage, since it is a reference of the DC system state.

On the second and third graphs from the top to bottom in Figure 3.15, it is seen that MMC internal energy and active power profiles depict a similar behavior, reaching practically a steady state. Nevertheless, once the Vdc-P droop is returned and the internal energy control is shifted to the DC cascaded loop at t = 3.8 s, an important transient is encountered.

The zoom-in figures help to visualize the control response and interactions. Once the fast energy controller is restored, it pulls power from the MTDC grid towards the MMC, as a slight difference is found with respect to its control objective, driven by the DC grid voltage due to the virtual capacitor. The fast action of the controller presents an important power overshoot, which reduces the MTDC voltage level, leading to the Vdc-P droop action, which causes another power transient on the AC system. The weak grid condition causes the AC voltage to present significant amplitude oscillations, feeding back a rapidly changing reference to the PLL, enhancing the oscillations on the AC system.

The interaction mechanism causing the perturbation propagation from the DC to the AC system is presented in Figure 3.16. The proposed solution to decouple this interaction mechanism initiated by the fast energy control and enhanced by the weak AC grid is to slow the energy controller and gradually return it to its pre-fault value. This can be done in different ways, e.g., by means of a state machine; for practicality, in this work, this is done by changing the controller's proportional and integral coefficients, considering a time and magnitude interlocking, as depicted in Figure 3.17, if the energy

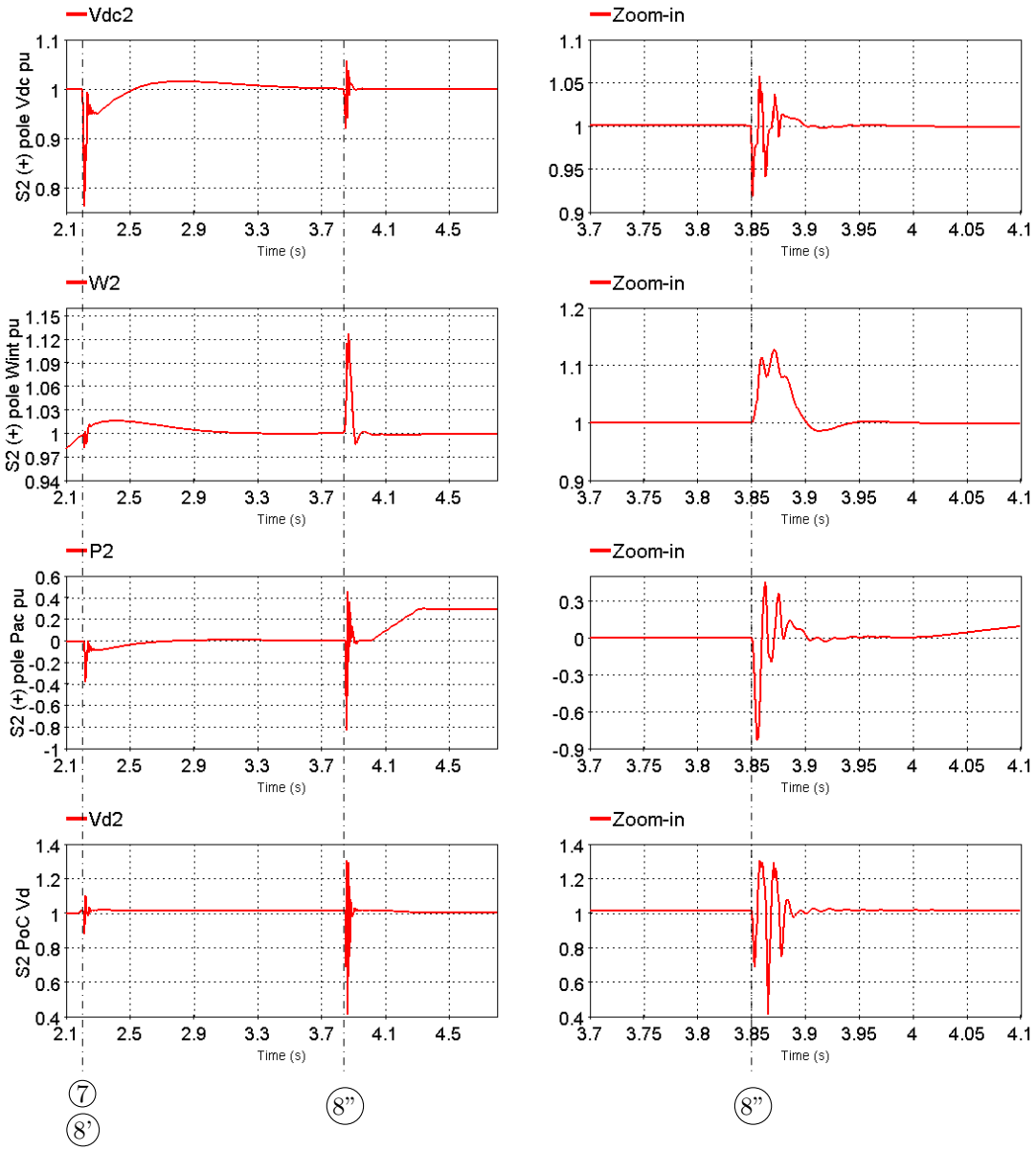


Figure 3.15: S_2 faulty pole DC voltage, internal energy, active power and PoC AC voltage amplitude

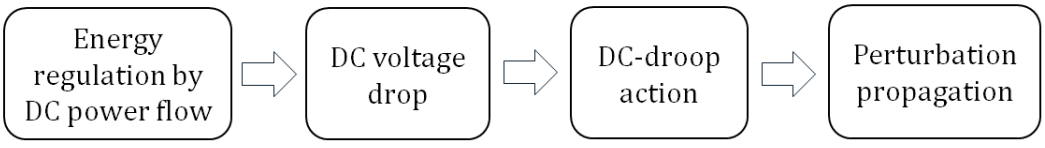


Figure 3.16: MMC control interaction mechanism and perturbation propagation.

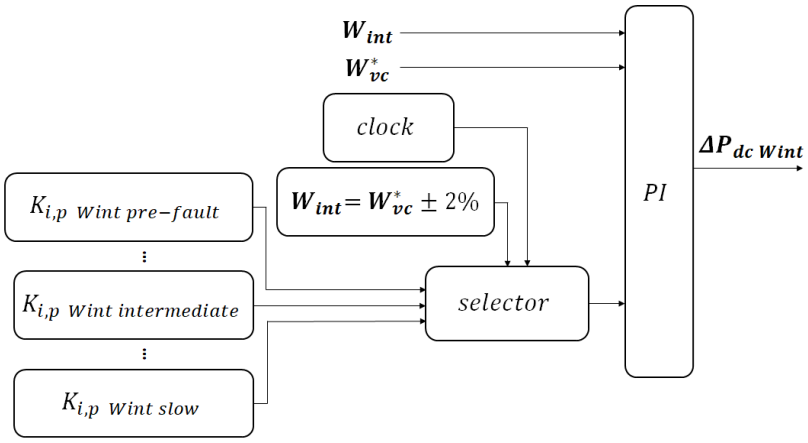


Figure 3.17: Internal energy control PI coefficients management during restoration process.

magnitude is not deviating form its control objective during a sufficient time, this can change to a faster coefficient, with the needed amount of changes to have a seamless transition.

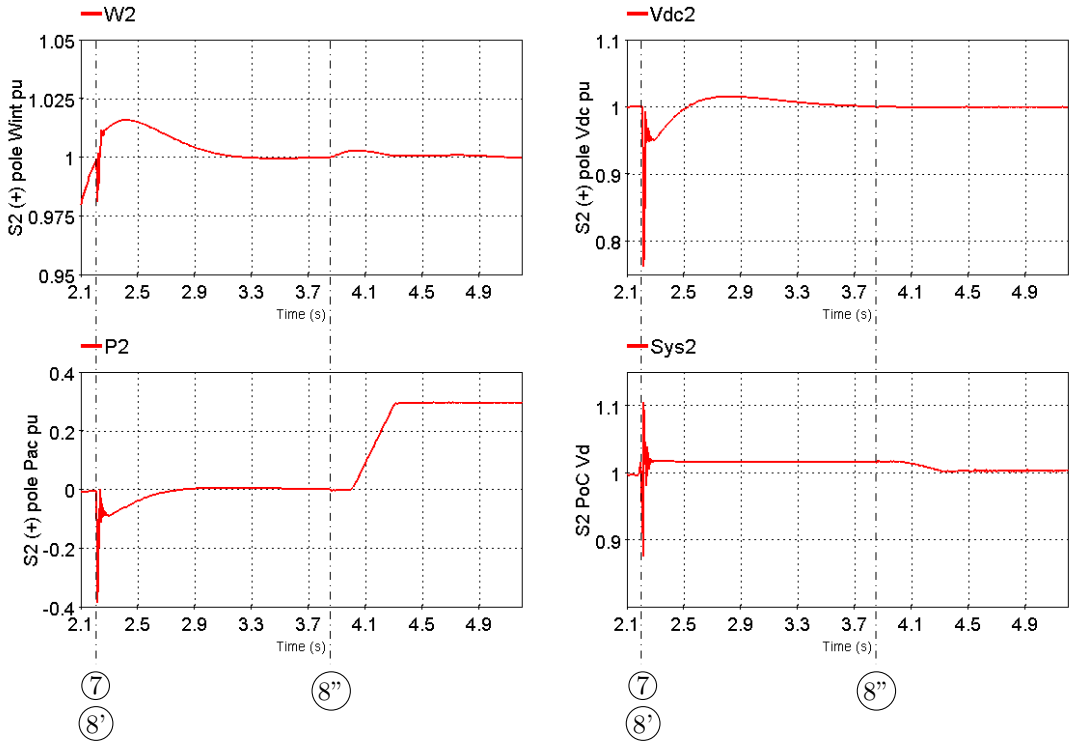


Figure 3.18: S_2 faulty pole DC voltage and internal energy with proposed solution

Figure 3.18 depicts internal energy, DC voltage, active power and the AC PoC voltage estimated amplitude during the re-energization process and pre-fault power restoration with the proposed solution. As expected the swap of the voltage control strategy together with a slower energy control decouples the interaction mechanism between controls presented in Figure 3.16. This is reflected in the energy profile which has a seamless transition at 3.850 s, hence overcoming the related issues. DC voltage as well presents a smooth profile, reflecting the partial decoupling of the MTDC voltage regulation and the MMC energy control. As a consequence, the AC power profile does not cause a perturbation on the AC system, which is reflected in the AC voltage amplitude, which only varies accordingly with the power flow variations.

3.4 Introduction to the GFM response

At this stage, the system DC FRT under a non-selective protection strategy and GFL control has been examined. The analysis of different system conditions during the DC FRT underscores the necessity of minimum coordinated C&P actions to maintain secure operation, as outlined in Figure 3.2. Furthermore, the reduced voltage stiffness of the weak grid has highlighted interaction mechanisms between the AC and DC systems. To improve the low voltage stiffness at the MMC AC PoC, a voltage source behavior is acknowledged as a good alternative. Therefore, in this section, GFM strategy is introduced to have an initial understanding of the implications of this control strategy facing a large disturbance. Therefore, only the fault clearing process is analyzed here, while the complete DC FRT is reviewed when using GFM with DC voltage regulation in the next chapter.

3.4.1 Expected voltage source dynamic behavior

Recently, GFM control has emerged as an alternative to overcome the fundamental limitations of the GFL strategies [89], [129]. Unlike GFL control, GFM converters establish their own voltage reference, thereby avoiding MMC control dependency on the grid voltage condition, which might complicate the system operation during large

disturbances or other kinds of voltage perturbations [49], [88].

This section introduces the GFM control response under DC fault conditions. The objective is to develop an initial understanding of the MMC AC-side response to a DC fault when operated with GFM control, without introducing additional complexity from a supplementary control layer, such as a Vdc-P droop. The analysis will therefore focus primarily on the AC-side behavior of the GFM-controlled MMC.

The GFM approach is based on the emulation of the synchronous machine behavior. To this end, the VSM approach is used, as this control strategy offers the frequency and voltage support not found in the GFL strategy. The parameterization used for the VSM is as follows: for the emulated swing equation (2.10), $H = 1.5$ s and $k_d = 150$; while the Vac-Q droop (2.11), m_v =0.15. Using the obtanied characteristic equation (2.9) of the VSM approach (see Figure 2.9), and the proposed parametrization, the response time can be calculated, in this case, $t_{r,\ vsm}$ =1.79 s. Therefore, the new control dynamics introduced by the VSM in the GFM strategy, compared to the reference case, necessitate an adaptation of the C&P sequence timing. This adjustment increases the interval between actions, thereby avoiding the superposition of transient phenomena and control responses.

The VSM parameters will be discussed further in subsequent chapters, where the MMC internal energy is examined in greater detail. On the other hand, the Vac-Q droop proves essential under weak grid conditions due to its dynamic response to AC voltage amplitude variations. In the approach taken here, the GFM's inherent voltage support is primarily governed by the droop coefficient m_v, which determines the MMC's sensitivity to AC voltage variations.

3.4.2 MMC AC side response under DC FRT

The MMC AC response with GFM control at station S1 is now analyzed under a weak grid condition (SCR = 1.52), similar to previous subsection. This scenario highlights key benefits of the GFM strategy, as the VSM approach provides inherent voltage and inertial support. Consequently, AC voltage and frequency stability at the interconnected grid are enhanced when the MMC employs this control strategy. Given that no

dynamic elements are modelled on the AC side, only the improvement in AC voltage behavior is presented.

Figure 3.19 shows the faulty pole DC voltage, AC voltage amplitude, active power, and reactive power profiles for stations S_1 and S_2 during the fault clearing. The C&P sequence illustrated in Figure 3.2 can be followed using the labels at the bottom of each plot. Upon fault inception, a zero-potential point is created, the initial current flowing towards the fault emits an electromagnetic wave that propagates along the different conducting elements towards the transmission cables' end. After the respective propagation delays, the DC voltage at each station drops sharply, reaching negative values. Similar to earlier scenarios, the oscillatory DC voltage profile is reshaped once the MMC blocks, followed by the complex behavior of the fault current [130].

AC voltage amplitude has an important dip as the faulty pole converter blocks and feeds AC current towards the DC fault location once the MMC blocks. The GFM station, S_1 has a delayed drop and a higher minimum value, when compared with the GFL station, S_2, due to the healthy converter actions, (see Figure 3.20). Active and reactive power profiles during the fault transient are mainly driven by the fault current, as in the previous scenarios; yet, for the GFM station (profiles in red), the drop of active and reactive power comes after the GFL one (profiles in blue), thanks to the healthy pole actions – shown below (see Figure 3.20). As pointed out, the AC response of the healthy pole is shown in Figure 3.20.

The left-hand side of Figure 3.20 displays the active power response of the converters at stations S_1 (GFM, in red) and S_2 (GFL, in blue). As expected, a clear contrast is observed in the initial system natural behavior and following control responses between the GFM and GFL strategies. The voltage-source behavior of the GFM converter leads to a power increase corresponding to the voltage phase jump caused by the sudden loss of power infeed from the faulty converter. As AC voltage drops, two sequential reactions from the healthy pole converter occur. Initially, the voltage source behavior presents a power spike, which is originated by the phase jump linked to the power infeed loss through the faulty pole converter and fault current infeed towards the DC fault. This is followed by the energy release towards the AC system corresponding to the inertial

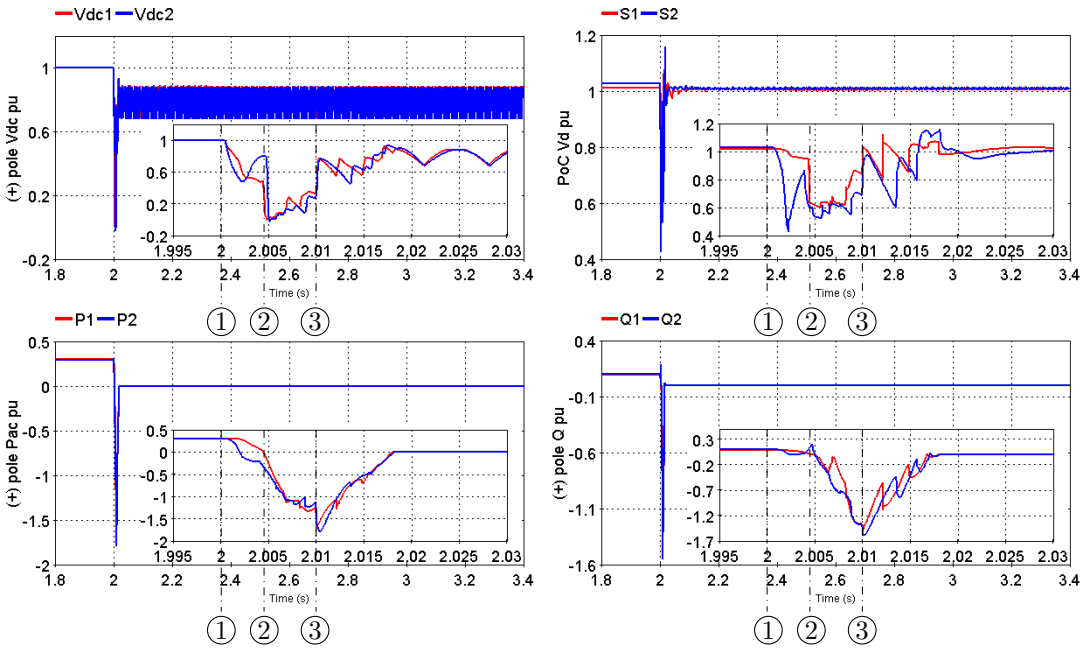


Figure 3.19: S_2 faulty pole DC voltage profiles - GFM introduction

response (IR) of the VSM, increasing the MMC power output.

This power peak drives the MMC to reach its current limit, as visible in the bottom-left zoom-in section of Figure 3.20. After the positive-pole MMC blocks (around 4 ms after fault inception), the rate of power increase grows further, due to the voltage phase jump encountered, identified in the top-right zoom-in section of Figure 3.20 . The power increase in the healthy pole is composed of a low voltage, and, consequently, a large current. As real power nears 0.6 pu, the large AC output current activates the $Z_{virtual}$, creating a virtual voltage drop within the MMC AC cascaded control loop. The resulting profile resembles small phase jumps, caused by the intermittent activation and deactivation of the $Z_{virtual}$ due to rapid variations in the MMC AC current — which is dominated by the AC voltage behavior at the PoC and the IR, according to the mismatch of the converter power reference and power output, emulating the IR of a synchronous machine when the mechanical and electrical power face a difference. DC voltage of the MMC is decreased as the IR response takes the energy from the converter itself, which is replenished by the MTDC grid by means of the MMC internal energy controller.

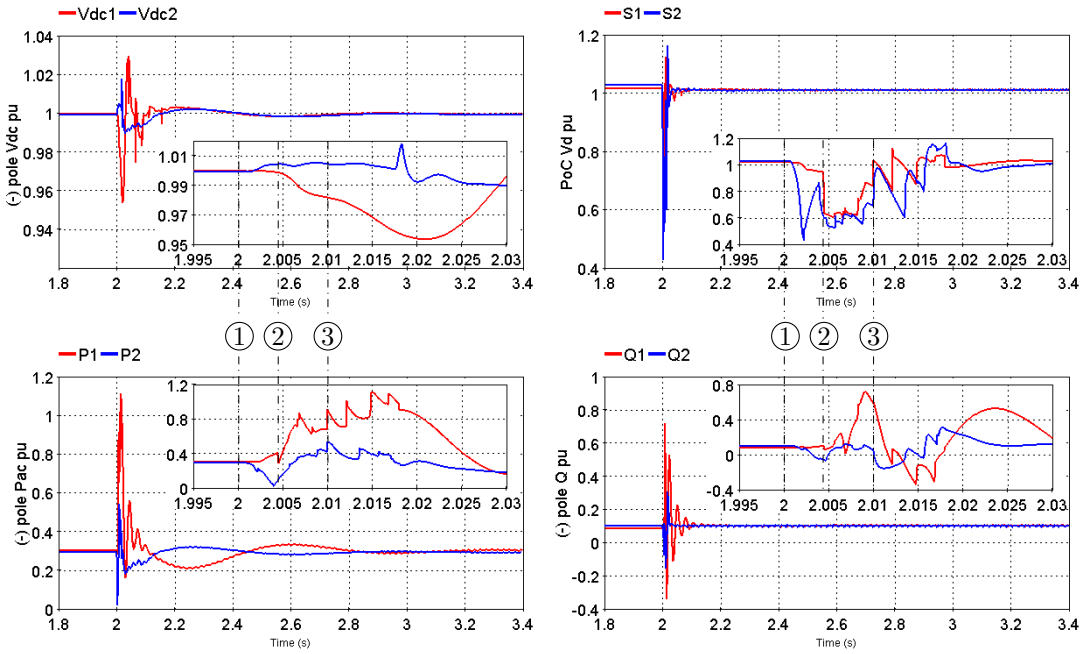


Figure 3.20: S_2 healthy pole active and reactive power profiles - GFM introduction

Once AC voltage magnitude drops, the healthy pole GFM converter injects a large amount of reactive power reaching almost 0.8 pu, as seen in the bottom-right zoom-in section of Figure 3.20. This reactive power injection accelerates the recovery of AC voltage, which after the DCCB opening at t = 2.01 s, sustains a level above 0.8 pu, presenting high frequency oscillations until the fault current is extinguished. The AC voltage recovery enables the healthy converter to inject higher active power into the interconnected AC system, reaching levels above 1 pu, as seen in the bottom-left zoom-in section of Figure 3.20.

Conversely, the positive pole of the GFL station (shown in blue in the same figure) exhibits no active response to the AC-side disturbance. Its behavior is initially governed by the AC voltage dip, which drives the MMC's active and reactive power outputs nearly to zero. This reduction in power export to the AC system causes the MMC DC voltage to rise. Apart from the initial transients during the DC fault inception and opening of the DCCBs, the GFL tries to maintain the DC side voltage control. After the first DC voltage dip, originated by the GFM IR, the GFL converter corrects its power output, allowing the DC voltage quick restoration, with a small overshoot, as

seen on the left-hand side of Figure 3.20.

Furthermore, it is identified that the GFL power profiles has an opposite oscillation to that of the power swings of the GFM converter. The GFM control is driven by the swing equation parametrization, in particular its H and k_d, increasing and decreasing its power inversion from the MTDC grid. Therefore, to each increase or decrease, the GFL converter acts in the opposite sense, compensating with the adequate amount of power to have a fast regulation of the MTDC voltage. After the DCCB opening, at t = 2.01 s, reactive power output also tries to follow the control order, only facing oscillations due to the AC PoC voltage behavior.

3.5 Summary

This chapter has served as an introduction to an MTDC system DC Fault FRT when using a non-selective protection strategy. Two AC control strategies were reviewed: GFL in Vdc-P droop mode, as a benchmark control strategy for Chapter 3, and GFM in P-mode as an introduction to this control strategy. A generic C&P coordinated sequence was presented to ease the use of the analysis methodology proposed in [93], highlighting two main stages of the DC FRT: the fault clearing and restoration process.

Based on the first methodology developed and presented in this work, Figure 2.17, the reference scenario, interconnecting strong AC systems (SCR = 5), allowed for the identification of minimum requirements for control actions imposed by the studied protection philosophy. An MMC DC FRT dedicated control architecture was proposed and tested, delivering main profiles and characteristic responses of the GFL control strategy. Furthermore, a particular AC grid condition was reviewed, i.e., the weak grid condition, i.e., (SCR < 3). Two re-energization strategies, within the restoration process, were analyzed for GFL control: the use of shared Vdc-P droop activation or a single converter Vdc-master use. The analysis highlighted a control interaction mechanism that caused undesired perturbations on the AC system, due to the weak grid voltage sensitivity to power disturbances. Control-oriented solutions were proposed, going from control tuning to new coordination, including sequencing and tuning.

For the GFM strategy introcution, the AC MMC behavior and control responses

during the fault clearing were analyzed when implementing the control strategy in P-mode. This introductory analysis highlighted that even with a low inertia constant value, the converter can reach its current limits, and will have the MMC as the first energy source for the GFM IR. Moreover, the remaining GFL converters demonstrated a fast capability to regulate the MTDC grid voltage, once the GFM converter pulled power from the DC system to compensate for the energy used in the IR.

Chapter 4

MTDC voltage regulation by VSM-based GFM control

4.1 Chapter introduction

Chapter 3 served for both purposes: an introduction to the system DC FRT with a non-selective protection strategy, and to have an initial understanding of the GFM strategy. This chapter presents deepening insights into GFM control, by adding another control layer to the MMC cascaded control, namely, the Vdc-P droop, reaching a control architecture with more functionalities and complexities.

This control architecture attempts to meet both AC and DC needs of the hybrid system. On the one hand, the dynamic support needed by AC systems, is achieved by the VSM approach, as it emulates the IR and damping behavior of synchronous generators, together with inherent voltage support [131]. On the other hand, the MTDC voltage regulation is achieved through coordinated droop control strategies [132]. Consequently, these two control functionalities must operate in harmony during normal operation and transient events.

This chapter examines the integration of GFM control as the sole strategy for voltage regulation in the MTDC network when using a non-selective DC protection philosophy. Furthermore, it presents a study methodology developed for the understanding of the implications of this control strategy for a given DC protection strategy or DC

circuit arrangement, which is also used in Chapter 5.

4.2 GFM in Vdc-P droop mode integration analysis

The GFL-based control coordination served as a reference scenario for understanding the system DC FRT, and the healthy pole firewall effect during AC disturbances [133], as presented in Chapter 3. In this chapter, two case studies with different MTDC control coordination are analyzed, as presented in Table 4.3. This sequence of studies allows a better understanding of the tested generic control and its implications at different levels for the hybrid system along the DC FRT.

4.2.1 Control architecture analysis

The MMC's control architecture integrates the DC voltage controller through both AC and DC cascaded control loops, as illustrated in Figure 4.1. The dynamics of power exchange on each side differ fundamentally due to the distinct control hierarchies beneath the primary Vdc-P droop command.

- On the AC side, the droop command acts upon the VSM synchronizing loop, which governs the MMC AC voltage and power exchange
- On the DC side, the same droop command cascades through the DC power control down to the fast inner current control loop regulating the MMC DC voltage and power exchange

Adhering to cascaded control principles, where each outer layer must respect the dynamics of the faster inner loops, this structure results in different power response characteristics. The AC-side dynamics are shaped by the inertial and damping properties of the VSM. In contrast, the DC-side dynamics are mainly governed by the bandwidth of the inner current controller and the intermediate DC power and internal energy control loops. Therefore, this control architecture, integrating GFM principles, represents a complete paradigm shift in MMC operation compared to GFL control. The different time constants of their respective AC control loops underscore this shift, as compared

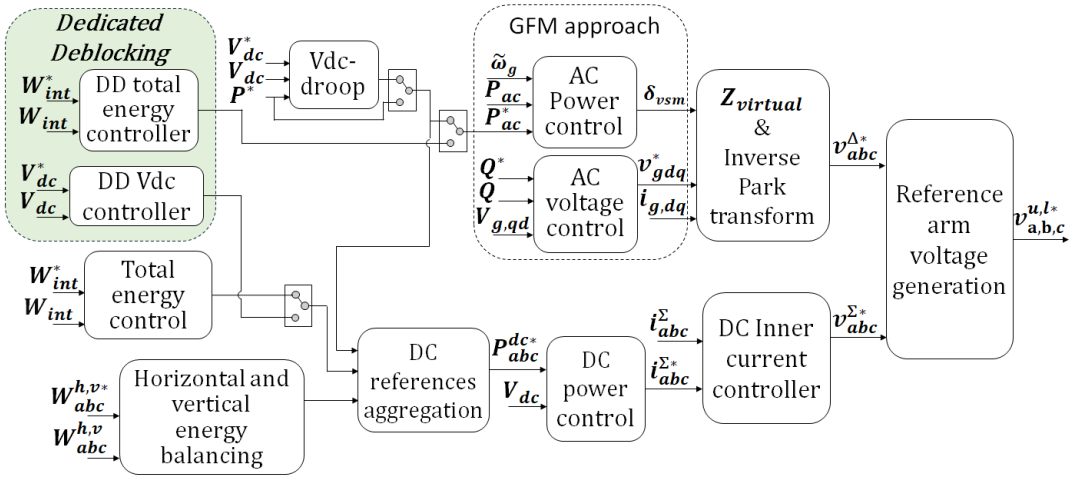


Figure 4.1: MMC GFM control architecture, where the dedicated control to perform the DC FRT is highlighted.

Table 4.1: Droop and AC control loop response time for GFL and GFM control

Control strategy	Droop control [%]	AC power control [s]	Inner current control [s]
GFL	10	-	10^{-3}
GFM	10	1.79	-

in Tables 4.1 and 4.2, considering the VSM parametrization presented in Chapter 3 and the VSM characteristic equation (2.9) derived in Appendix A.

By analyzing the rise time of each cascaded loop, it can be identified that a potential conflict may arise between the inertial response inherent to GFM control and the requirements for stable DC voltage regulation. This is particularly critical for maintaining the desired dynamic performance and stability of both AC and DC systems through proper operation of the MMC. Functioning as an energy buffer, the MMC must accommodate the differing dynamic characteristics of the AC and DC grids, thereby placing constraints on its operation to maintain system stability, particularly under large disturbances. To ensure the safe and reliable operation of MMCs, energy-based control and compensated modulation are often employed to manage their internal energy dynamics and prevent violation of operational limits[62], [75], [82], [134].

Table 4.2: Droop and DC control loop response time for GFL and GFM control

Control strategy	**Droop control** [%] & **Energy control** [s]	**DC power control** [s]	**Inner current control** [s]
GFL & GFM	10 & 10^{-2}	-	10^{-3}

Table 4.3: study cases

Scenario	$V_{dc} - P$ droop S1 & S2	P-mode S3 & S4
Scenario 1	GFM & GFL	GFL & GFL
Scenario 2	GFM & GFM	

4.2.2 Study methodology

In order to study the proposed GFM integration as the sole control strategy regulating the MTDC voltage - taking the DC FRT with GFL of Chapter 2 as reference - two case studies are proposed, as presented in Table 4.3, thus building a study methodology. This allows for the analysis of the system-level implications of the GFM integration when using a non-selective protection strategy, e.g., the available degrees of freedom, together with control and physical interdependencies. This methodology is presented in Figure 4.2. As the reference case has been already presented in previous chapter, in this chapter only the second and third steps of the methodology are presented with two scenarios.

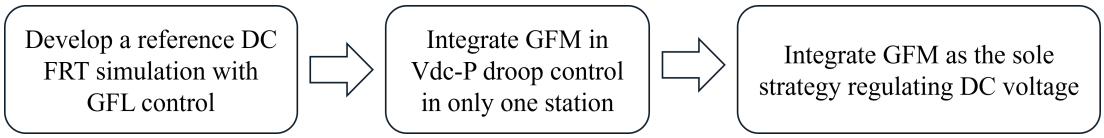


Figure 4.2: GFM integration as the sole strategy regulating the MTDC voltage

4.3 Simulation model

Same MTDC system topology as in Figure 3.1 is used. The nominal values of the MTDC system are given in Chapter 2. The 2 onshore stations (S_1 and S_2) operate in GFL/GFM strategies, sharing the task of DC voltage regulation by means of droops.

Differing from previous chapter, now the two onshore stations are regulating the MTDC voltage. Therefore, the model of the offshore stations (S_3 and S_4) providing power from the OWFs is simplified, using GFL converters controlled in P-mode.

Pole-to-ground faults are incepted at the middle of the cable connecting stations S_1 and S_2 in all the scenarios. To clear the fault, all DCCBs operate under the tripping and closing signals from protection relays. The total time between fault inception and fault neutralization by the DCCBs, including the time for protection algorithm computation, relay to DCCB communication, and DCCB operating time, are assumed to be 10 ms, though faster opening times have been acknowledged in the literature [107], [109]. As in previous chapter, the rather long DCCBs opening time considered does not significantly impact the presented studies, as the faulty converter poles lose power transmission capability under the non-selective protection strategy, irrespective of whether they are blocked or not.

The MTDC re-energization strategy is based on the activation of the Vdc-P droop. As well, The interconected AC systems are considered to be strong grids, namely, with an SCR = 5, and each station features a grounded return to simplify the modelling approach and enable better identification of the control responses under scrutiny. The DC FRT analysis is carried out in a sequenced manner, from fault inception until post-fault active power restoration, and it is segmented into two main sections: fault clearing and restoration process [93], [120].

As shown in Figure 3.2, the two scenarios follow the same protection sequence. Upon fault inception (instant 1), the faulty pole converters are quickly blocked as a result of converter overcurrent protection (instant 2). To start the fault clearing, the DCCBs are opened 10 ms after the fault inception in a non-selective protection strategy (instant 3). After the fault clearing and faulty cable isolation (instant 5), the restoration process starts.

The timing to initiate the restoration process (i.e., converter deblocking (instant 4), see Figure 2.16), the DCCBs reclosing (instant 6), DC voltage restoration (instant 7) and active power restoration (instant 9), are modified in each scenario due to the imposed dynamics of the GFM strategy. In Scenario 1 each stage of the restoration

process is delayed with respect to the reference case, allowing sufficient time to characterize the system performance during each dynamic event. Furthermore, in Scenario 2, adding a second GFM-controlled converter further slows down the overall system dynamics, requiring additional modifications to the MMC control parametrization, as will be demonstrated in the next section.

4.4 DC FRT with GFL & GFM

In this scenario, the GFL- and GFM- controlled MMCs share responsibility for regulating the MTDC system voltage, as shown in Table 4.3. Thus, new interactions will be identified, in comparison with the introduction to GFM analyzed in previous chapter. As in the GFM introduction, the intervals between events in the C&P sequence were extended - when compared with the GFL reference case - to ensure sufficient time for the converters' responses to settle, thereby preventing the analyzed phenomena from overlapping. Furthermore, to have a global overview and better understand the implications of the GFM control with Vdc-P droop in the system operation, the analysis starts with three fundamental signals owing to their physical and control interdependencies: DC voltage, active power, and the MMC internal energy.

4.4.1 Fault clearing

Figure 4.3 shows the positive and negative pole DC voltage, active power, and internal energy of the MMCs during the fault transient. As in the reference case, the DC voltages of the faulty pole quickly drop after the inception of the fault at 2.0 s (small delay due to the travelling time of the first electromagnetic wave takes to reach the converter station [135]). Overcurrent protection quickly blocks the converters, preventing the stored energy in every MMC of the positive (faulty) pole from further decreasing and damaging the converter valves.

The difference in the blocking time between the GFL converters, i.e., S_2, S_3 and S_4, is mainly linked to their electrical distance to the fault location; contrastingly, the GFM converter has a later blocking. This is explained by the arm current components, as

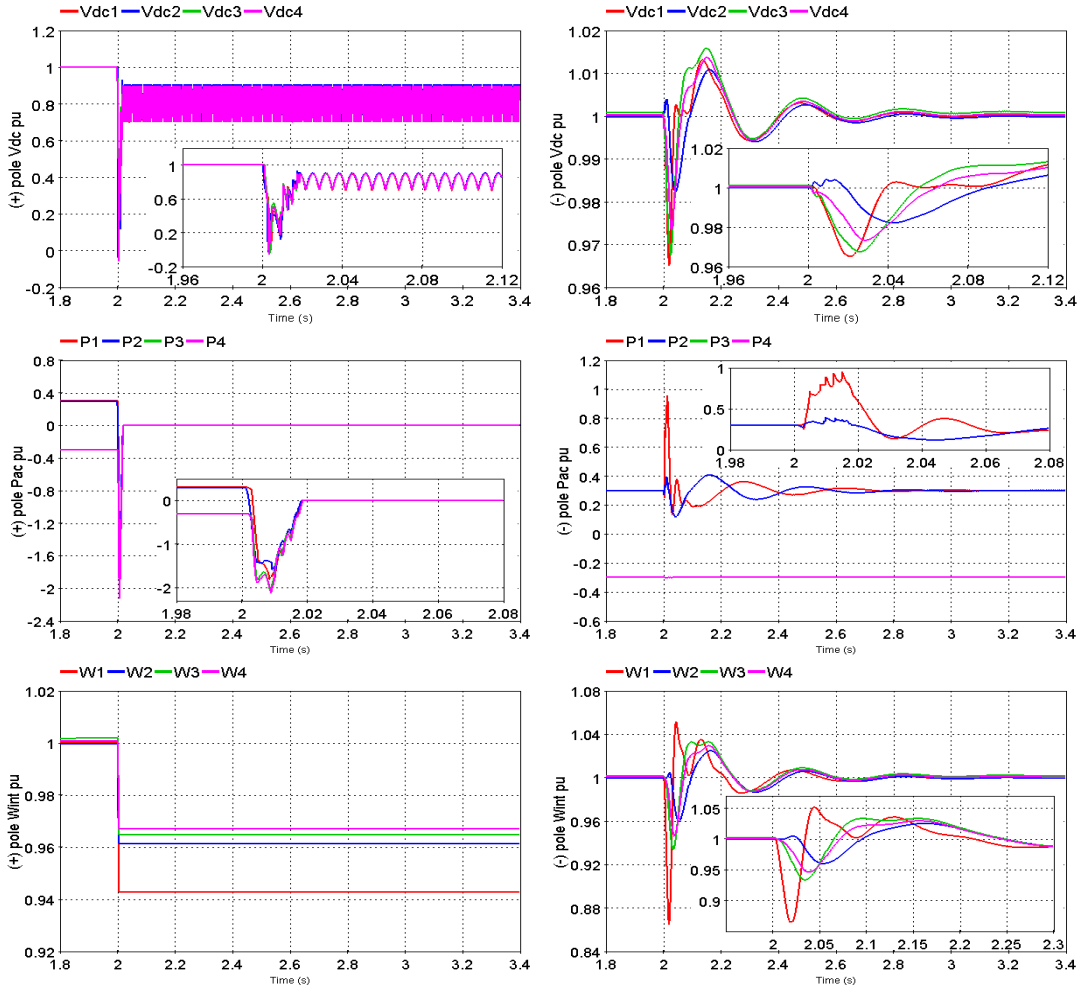


Figure 4.3: MTDC faulty and healthy poles Vdc profiles - with GFL & GFM

given by 2.18 and GFM control characteristics, explained in previous subsection. The slower AC dynamics of the MMC imposed by the GFM control and the PoC voltage, leads to reaching the blocking threshold in a later moment, as depicted in Figure 4.4. Of course, the AC grid conditions might vary the current contributions at each converter station, e.g., as discussed with the weak grid condition.

The zoom-in of the DC voltage profiles depicts the already known fault transient profile before and after the fault neutralization. Once the fault current is extinguished, the characteristic open circuit diode-rectifier profile is identified. On the active power profiles zoom-in the power transient is also identified. As seen in the previous chapter, the GFM profile, has a delayed drop due to the AC inherent support from the healthy

pole, in red; whilst the rest of the MTDC grid has a faster drop. In all cases, once the fault current is extinguished, the active power profile reaches zero.

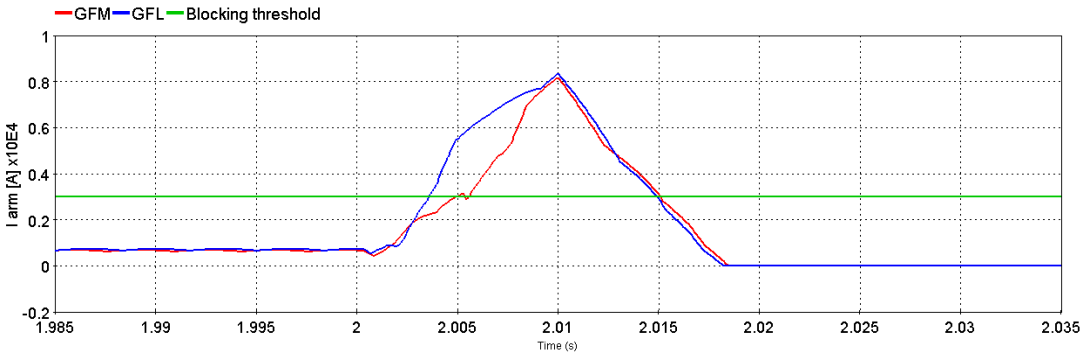


Figure 4.4: MTDC faulty and healthy poles Vdc profiles - with GFL & GFM

For the healthy pole converters, shown on the right-hand side of Figure 4.3. The MTDC voltage suffers a small dip, with the GFM converter exhibiting the lowest value, in red. This is due to the active power characteristic response of the GFM control described in the previous section, and here expanded with further details on the DC dynamics. The GFM converter increases its power output, in red, responding to a significant phase jump derived from the loss of power infeed from the faulty pole, followed by the inertial support to its interconnected AC system.

Nevertheless, once the GFM converter power output exceeds approximately 0.7 pu, the virtual impedance current limiter constrains the MMC power output, ensuring the safe operation of the MMC, as depicted in the zoom-in. This initial power response rapidly increases the energy export to the AC side, causing a transient drop of the converter's internal energy, in red, whereas the internal energy control promptly restores the energy level using the DC system as source to balance the energy used to support the AC system, as expected from the control architecture presented in Figure 4.1.

As the DC system is used by all the MMCs to manage their internal energy, under the virtual capacitor principle, the MMCs in P-mode only track the MTDC voltage state. Contrastingly, the converters regulating the MTDC voltage adjust their power exchange among the AC and DC systems to compensate for the energy used by the MMC AC response in the GFM strategy, as this also impacted the MTDC grid voltage.

Furthermore, from Figure 4.3, it is clearly identified that after the DC fault is neutralized, the power oscillations between the MMC at S_1 and S_2 are practically opposite and persist for around 1 s after the fault inception. The oscillations profile is mainly driven by the VSM dynamics, which in turn are dictated by H and k_d. These two parameters could be further adjusted to obtain a desired settling time. As expected, the perturbation is propagated to the DC system through the power, DC voltage and energy interdependence of the hybrid system.

4.4.2 Restoration process

The restoration process starts with the onshore MMCs' deblocking at the positive (faulty) pole (instant 4). As the DC system is still disconnected, only STATCOM operation is possible for these converters. To ensure safe MMC operation under either GFL or GFM control, it is imperative for the converters to manage their DC voltage and internal energy, as discussed in previous chapters. Once the onshore MMCs are deblocked at 3.40 s (instant 4), stations S_1 and S_2 faulty MMCs use the AC side to regulate their total energy under the DD energy control. As highlighted in previous chapter, the offshore converters lack a power source as the OWFs would curtail or reroute their power while the MTDC is not available, therefore, these MMCs only regulate their DC voltage, using their available energy. As well, these converters could be deblocked in a later stage, before the MTDC system re-energization.

As seen in Figure 4.5, it takes the GFM MMC (S_1) around 1.6 s to reach the energy control objective. While the GFL MMC (S_2) reaches its nominal value in 400 ms, with a small overshoot. After the DCCBs are reclosed at 5.00 s (instant 5), the MMCs partially re-energize the DC network, resulting in the transient drop of both internal energy and DC voltage. Next, the complete HVDC system can be re-energized by means of the the implemented Vdc-P droop at 5.60 s (instant 7), causing the main power transient during restoration, as seen in Figure 11.

Compared with S_1, the faster GFL active power response causes the converter in station S_2 to experience a larger power share when re-energizing the DC grid. Therefore, the interconnected grid should be capable of coping with such large perturbation.

Alternatively, as proposed in [136], the GFM converter may be temporary switched to GFL control during this period to ensure balanced power contribution from the two AC networks. In addition, a single converter in V_{dc}-master mode can be used to re-energize the DC system in a controlled manner, as seen in previous chapters.

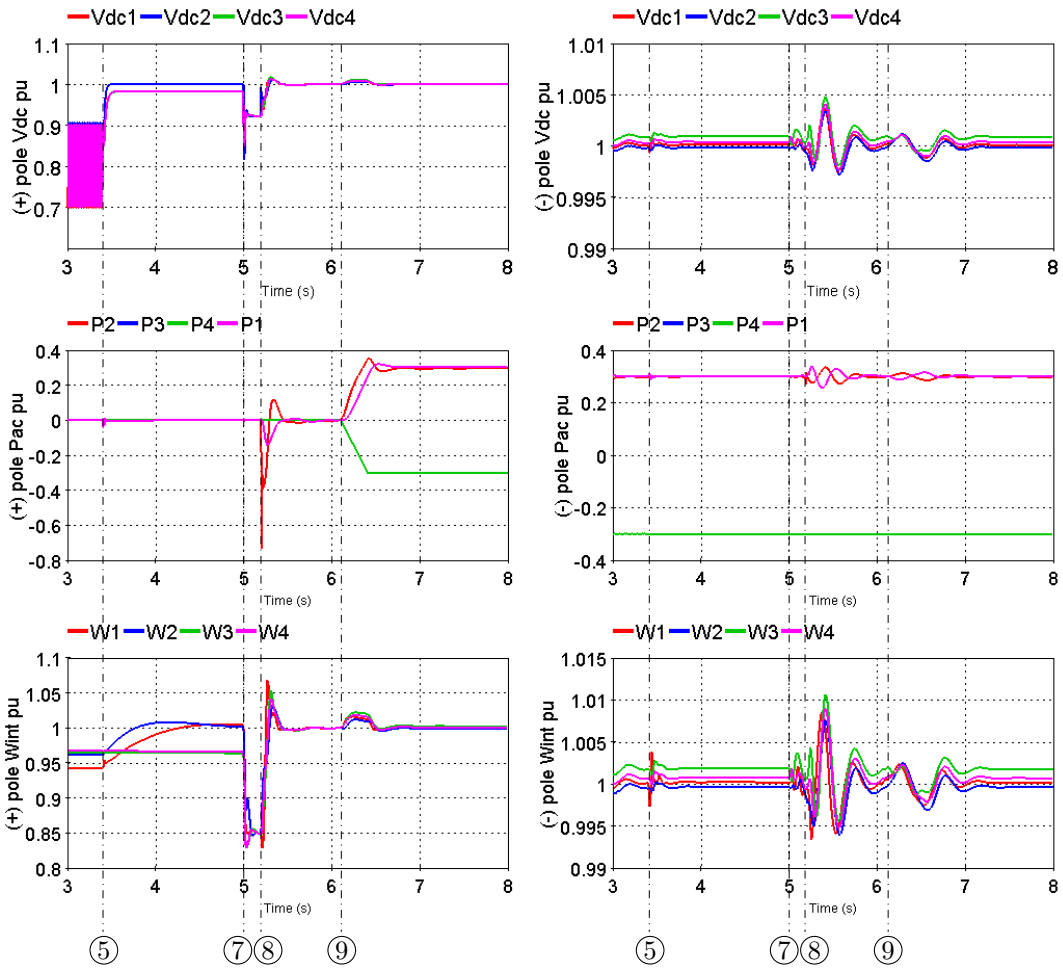


Figure 4.5: MTDC faulty and healthy poles Vdc profiles - with GFL & GFM

Finally, power restoration occurs at 6.10 s (instant 9). Both the GFM and GFL converters ramp up their power exports to the AC systems, while their DC voltages and internal energy are well regulated during the power restoration. On the healthy pole, the main variations of the healthy converter's energy are given by the perturbations caused by the faulted pole converter during the DC grid energization and the restoration of pre-fault power flow. Similar to energy profiles, DC voltages give a good indication

of the different stages along the DC FRT at both the healthy and the faulted converter. Thus, in both cases, the Vdc profile resembles closely the energy profiles. Nonetheless, the impact on the healthy pole is not as severe as in the case of the converter total energy. This is due to the fast AC response of the GFL converter to balance the Vdc variations.

As seen from this case study, having only one GFM-controlled converter does not pose a major issue for the system, despite the difference in control response. However, for larger MTDC grids with many converters, it is necessary to consider the difference in rise time, e.g., power ramp up, to ensure adequate coordination and power sharing among the different converters. The results from the healthy pole are omitted because their transients are minor.

4.4.3 Perturbation propagation mechanism

To better understand the perturbation propagation mechanism, the healthy pole of stations S_1 and S_2 are reviewed in more detail. To this end, AC and DC power flows with their respective control references, DC voltage, and internal energy of the MMCs are presented in Figures 4.6 and 4.7.

At station S_1 using GFM, the AC power response cannot follow its control command during a period after the fault inception, lasting practically 1.2 s. The power used to give support to the interconnected AC system leads to the MMC energy decrease. The energy controller requests power from the DC system to compensate for this reduction of internal energy, while the droop control quickly requests the converter to reduce its power extraction from the MTDC grid. Consequently, the MMC internal energy quickly recovers with a small overshoot.

On the AC side, the VSM dynamics lead to a reduction of the MMC power output. The mismatch between the AC and DC power flows, and energy absorption by the MMC, leads to abrief increase of the MMC DC terminal voltage, which oscillates in the opposite sense of the GFM-controlled MMC AC response util the oscillations are dampened by the VSM and the overall system damping. It is important to highlight, that, as expected from the previous analysis, the AC and DC power flows present an important

mismatch. Having the DC power response a proper track of its control command and the AC power flow facing difficulties in tracking the Vdc-P droop reference.

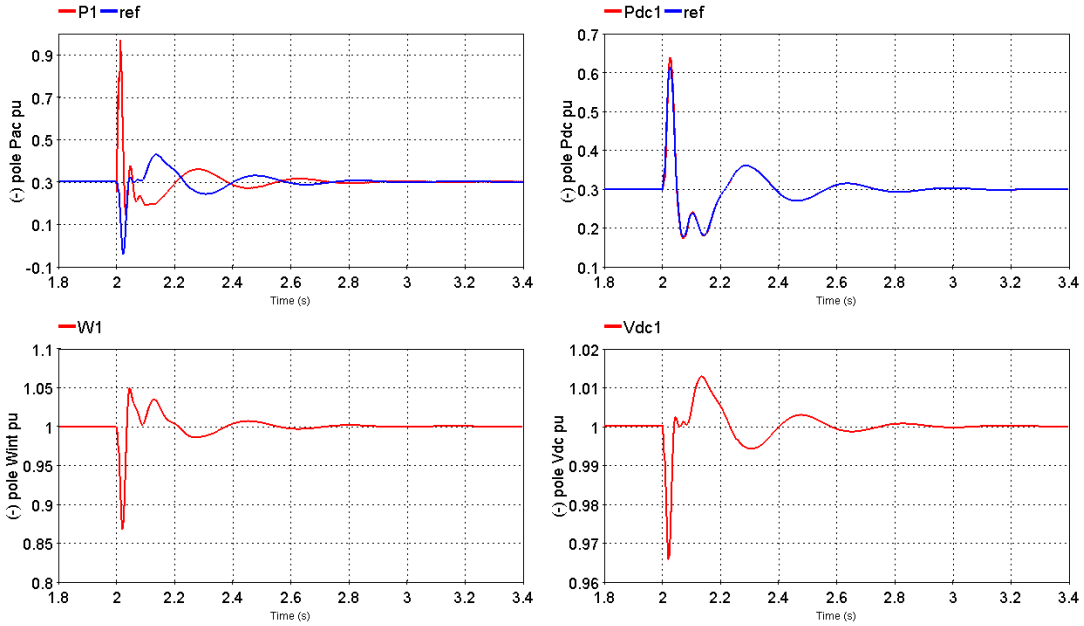


Figure 4.6: S_1 healthy pole in GFM during fault transient

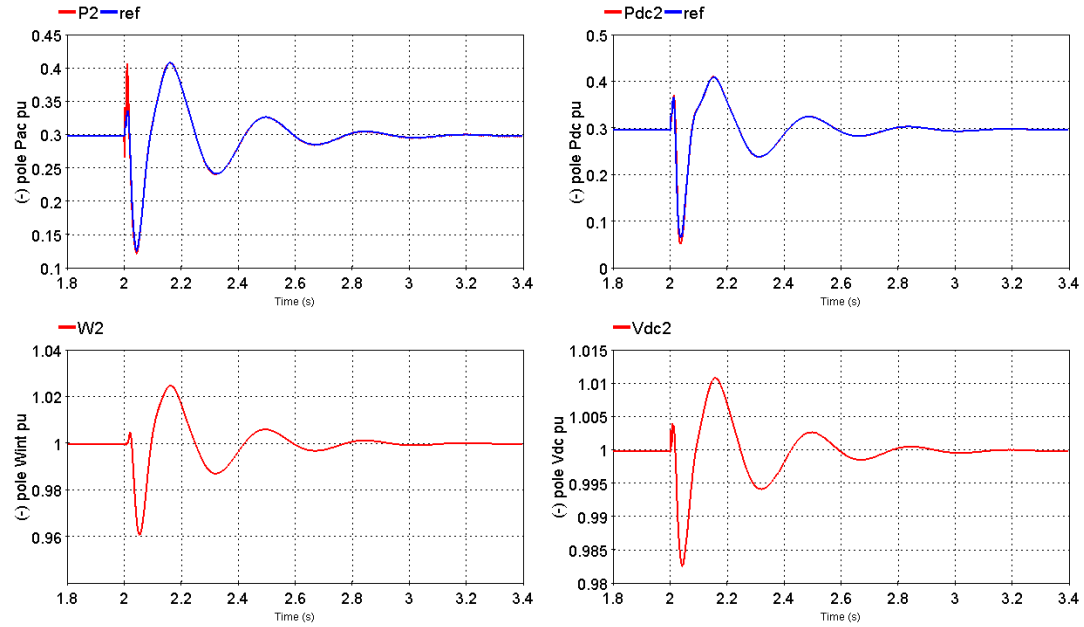


Figure 4.7: S_2 healthy pole in GFL during fault transient

As described above, after the healthy pole MMC in GFM delivers its IR towards the AC seen large disturbance, power oscillations cause the converter's internal energy to fluctuate, prompting the energy controller to request DC power to restore the MMC's internal energy level. These two interacting control responses create a mechanism that propagates the power oscillations from the AC into the DC system. As seen in Figure 4.3, the most affected converter is the GFM converter itself; nevertheless, the physical interdependencies lead to further impact on the remaining stations.

Figure 4.7 shows the station S_2 in the GFL strategy supporting the MTDC system voltage regulation by means of the Vdc-P droop. Consistent with the preliminary analysis presented earlier in this chapter, the simulation results demonstrate that both the AC and DC power flows track their respective control references with high fidelity, as these two cascaded control loops have fast dynamics as shown in Table 4.1. The GFL converter has a practically perfect track of its control reference, contrasting with the GFM-controlled MMC, indicating that the main responsible for the DC voltage regulation right after a large disturbance is the GFL converter. This is explained by the better match between AC and DC power flows of the GFL converter, when compared with the GFM converter, as discussed in the preliminary analysis of this chapter.

The faster AC power response of the GFL converter allows the MMC to have a better track of its control command, which is dominated by the Vdc-P droop, due to the DC voltage variations. The Vdc-P droop control takes further actions once the MMCs' DC voltage diverges from its nominal value, therefore, taking back part of the perturbation to the interconnected AC system at S_2. In this sense, the GFL-controlled MMC and the interconnected AC systems would oscillate against the GFM-controlled MMC, partially damping the osillations originated by the IR, which is driven by the emulated swing equation (2.10). Thus, the interconnected AC system is affected due to the perturbation propagation as described in the control interaction mechanism diagram of Figure 4.8

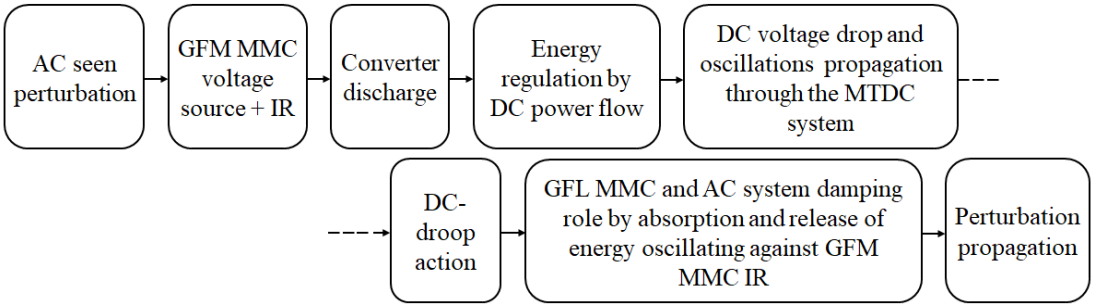


Figure 4.8: Control interaction and perturbation propagation mechanism with GFM and GFL

4.5 DC FRT with GFM in Vdc-P droop as the sole strategy regulating DC voltage

In this scenario, the MTDC control coordination is performed as given in Table 4.3. As described above, the use of GFM for both onshore MMCs slows the overall system dynamics during the analyzed transients. Therefore, to avoid the overlapping of transient phenomena during DC FRT operation, the time lengths of the coordinated C&P sequence in Figure 3.2 are adapted accordingly. Furthermore, as recognized in previous section, inertial response (IR) in GFM control can cause the MMC's internal energy to deplete, requiring additional DC-side power for rapid energy balancing. Consequently, the GFL MMC assumes primary responsibility for DC voltage regulation during the initial stages of the transient event.

By actively modulating its power output in response to the DC voltage variations, the GFL converter provides the necessary damping to suppress the oscillations excited by the GFM MMC's response. However, the situation becomes more critical in the current scenario, where both MMCs operate in GFM. In this case, when the MMCs provide IR to the corresponding AC systems, the required DC power may compromise DC voltage regulation. Therefore, additional control tuning is needed to avoid the identified conflict and enable a coordinated DC FRT operation by the MMCs. In this sense, the rise time of the energy controller is increased to the order of 10^{-3} s, resulting in a partial decoupling between the IR and the power requirement from the DC grid

to balance the internal energy of the MMC. However, it is essential to ensure that the converter's internal energy remains in a safe range during the operation.

4.5.1 Fault clearing

The fault transient is shown in Figure 4.9. As expected, seen on the left-hand side, DC voltage, active power, and internal energy profiles for the faulty pole at S_1 and S_2 resemble those of the GFM converter in Scenario 1. DC voltage drops after the first travelling wave reaches each converter station [135], followed by the MMCs blocking at 2.0025 s (instant 2), thereby bypassing the converter submodules and preventing further discharge of the MMCs.

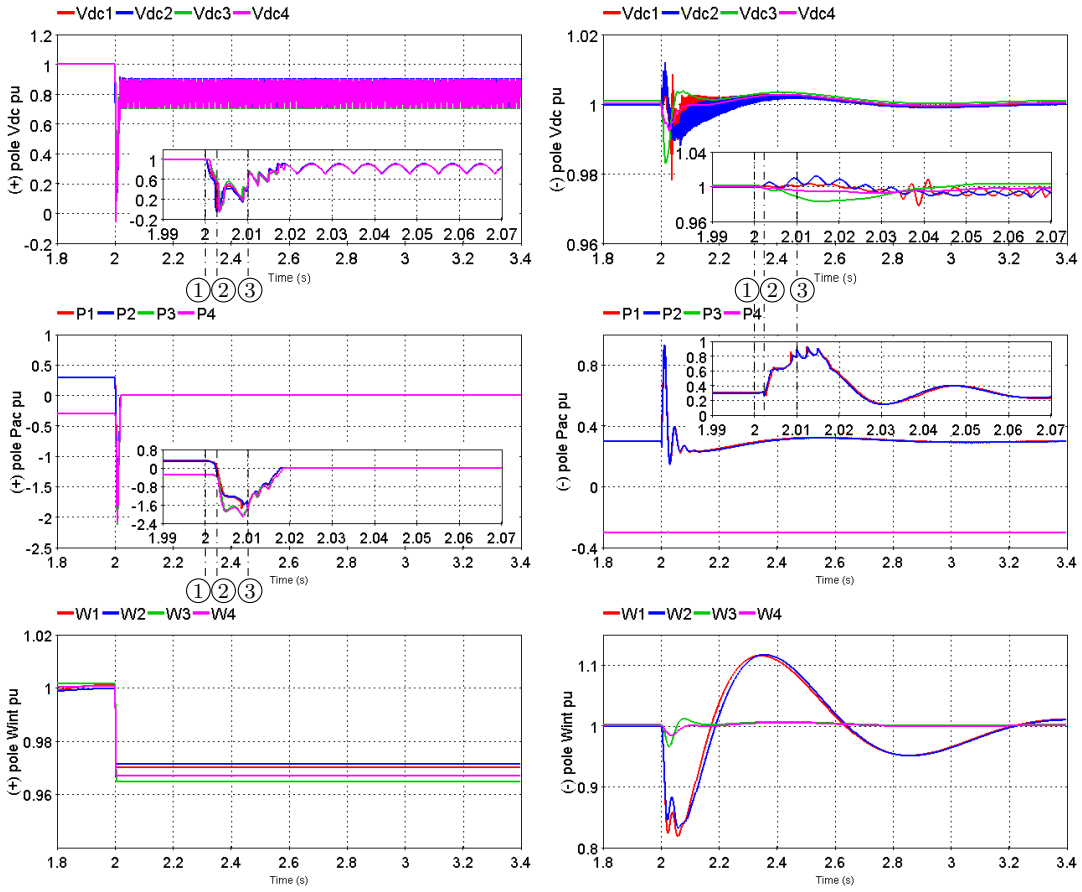


Figure 4.9: S1 and S2 fault transient detailed view - only with GFM

Once the DCCBs are opened at 2.010 s (instant 3), the DC voltage recovers to the

value determined by the open circuit diode rectifier characteristic. In the meantime, the fault current gradually decreases and the faulty cable is isolated (instant 5 but not shown in Figure 4.9).

On the healthy pole as shown in the right column in Figure 4.9, the active power responses of S_1 and S_2 are nearly identical due to their shared GFM parametrization, with minor differences arising only from the DC grid topology. The lowest energy level for the converters is approximately 0.85 pu during the transient, as both converters provide rapid IR response to the AC grids, quickly depleting their internal energy.

4.5.2 Restoration process

The restoration process is shown in Figure 4.10. Following the deblocking of the faulty pole MMCs at 3.4 s (instant 4), the DD controllers manage both the total MMC energy and the DC voltage. Energy is well controlled and DC voltage is quickly restored. When the DCCBs are re-closed at 5.4 s (instant 6), it causes transients on the DC voltage as the DC grid is partially re-energized. Finally, at 5.6 s, the V_{dc}-P droop is activated (instant 7) to regulate the DC voltage.

Due to the power supply from the power converter into the DC system, MMC internal energy is initially reduced, but quickly recovers by the converter energy control. It can be noticed in the bottom left graph of Figure 4.10, that both converters in GFM strategy have an energy overshoot that temporarily crosses 1.1 pu. This is caused by the differing AC and DC power dynamics when using GFM control, as described in previous subsections. Once the MMC's internal energy settles, power transmission is restored. The healthy pole, shown on the right-hand side of the same figure, exhibits small-magnitude perturbation propagation, thus highlighting the safe operation of the DC fault management on the positive pole.

Another key difference from previous scenarios is the pre-fault power restoration at 8.0 s (instant 9), which is performed more slowly. This is due to the slow dynamics of GFM compared to GFL control, and the new tuning of the energy controller, which presents slower dynamics. Therefore, to prevent larger excursions in the converter internal energy, the power is ramped up over 1.5 s. Similar to Scenario 1, the

healthy pole converters exhibit minimal magnitude variations in response to the power perturbations at different stages of the DC FRT C&P sequence.

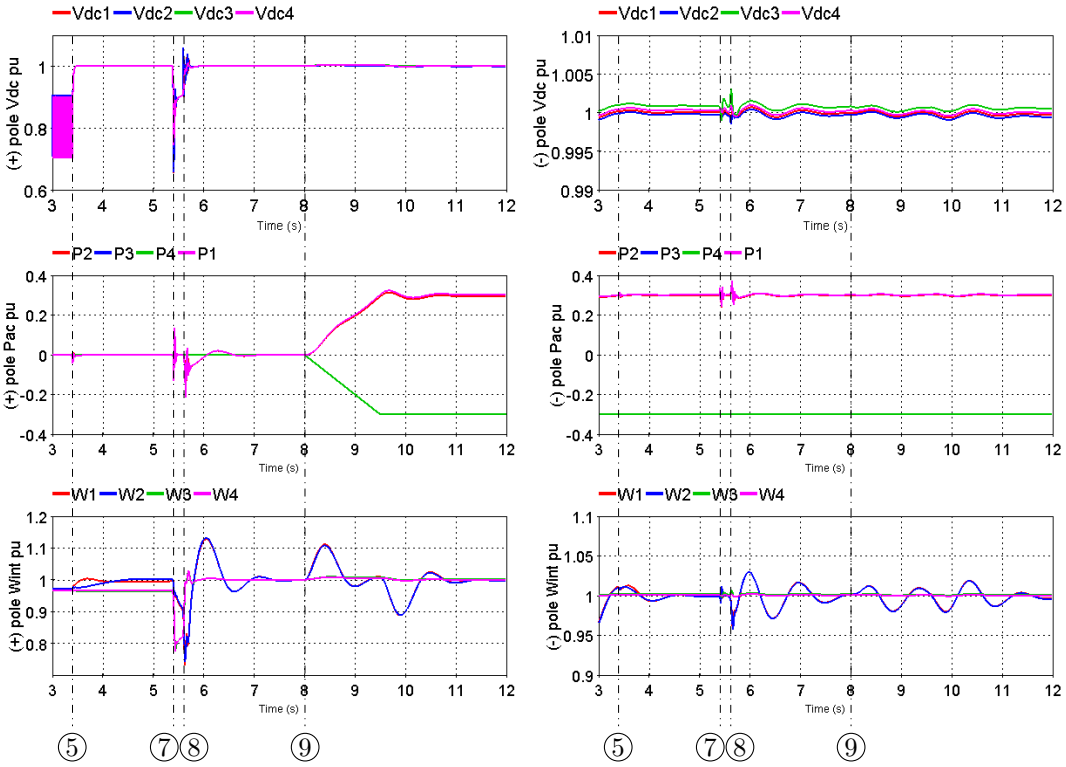


Figure 4.10: S1 and S2 restoration detailed view - only with GFM

4.5.3 Comparison of applying a short temporary stop for the three cases

Once the DC FRT operation is fully understood for a generic GFM approach in V_{dc}-P droop control mode, the C&P sequence duration can be reduced to accelerate system restoration. Therefore, the focus of this analysis is set only on the faulty pole converters at stations S_1 and S_2. Following the sequence timing of Chapter 3, the proposed temporary stop takes 400 ms to begin the ramp-up of active power. On the left-hand side of Figure 4.11, the reference scenario is depicted, where only GFL control is used; on the right-hand side of the same figure, the second scenario is depicted, where GFM control is introduced at station S_1.

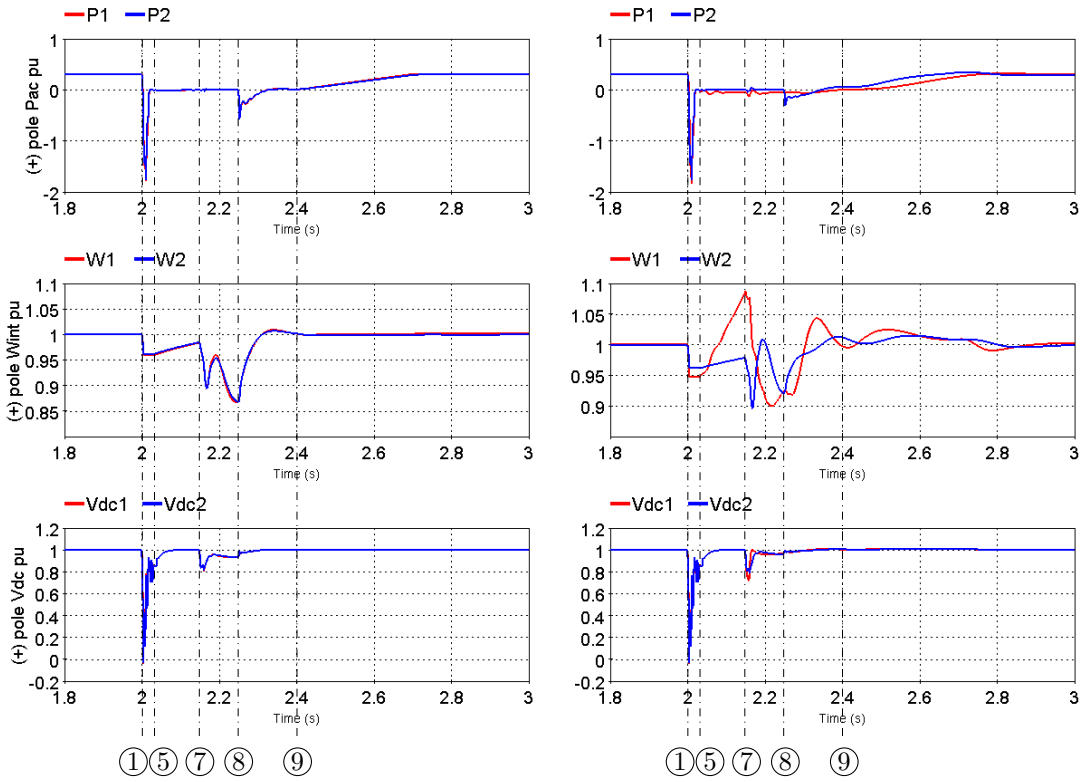


Figure 4.11: First and second scenarios comparison - same C&P sequence

The reference case, described in detail in Chapter 3, presents a well-managed DC FRT in the 400 ms sequence. After the fault inception at 2 s (instant 1) voltage drops, the faulty pole converter blocks at 2.003 s (instant 2) and the DCCBs open at 2.010 s (instant 3). The restoration process starts with the MMC deblocking at 2.030 s (instant 5) with the activation of dedicated deblocking controllers; its internal energy is managed via power exchange with the AC side, and its DC voltage is managed with a master controller.

Once the DCCBs are reclosed at 2.100 s (instant 6), the MMC has a partial discharge, as the MTDC grid pulls a current given its lower potential with respect to the MMC. After a short transient caused by the PIRs, the Vdc-P droop control at stations S_1 and S_2 is reactivated at 2.3 s (instant 7), bringing power from the AC side to the DC system and completing the DC grid re-energization. The MMC internal energy and DC voltage are then restored, and at 2.4 s (instant 9), active power is ramped up to its pre-fault value at a rate of 0.1 pu per 0.1 s. In contrast, in the second scenario, the

fast restoration presents significant energy excursions due to the MMC AC response, driven by the GFM strategy, as seen in the red active power profile.

To mitigate the observed energy excursion caused by power exchange mismatches between the AC and DC sides of the MMC, two primary alternatives are investigated in this work.

Alternative 1: GFL-to-GFM Transition

The first approach involves switching to GFL strategy before deblocking to facilitate a "soft" restoration. Control is subsequently returned to GFM mode once the pre-fault active power is restored and the PoC has settled down. This transition scheme is illustrated in Figure 4.12. To ensure a seamless transition, two control actions are done simultaneously at the precise moment of the switch:

- The d- and q-axis components of the difference voltage reference, $v_{dq}^{\Delta*}$, generated by the GFL strategy are held and added to the corresponding GFM control loop references
- The VSM calculations for the MMC output voltage angle and grid frequency are reset to the PLL estimation

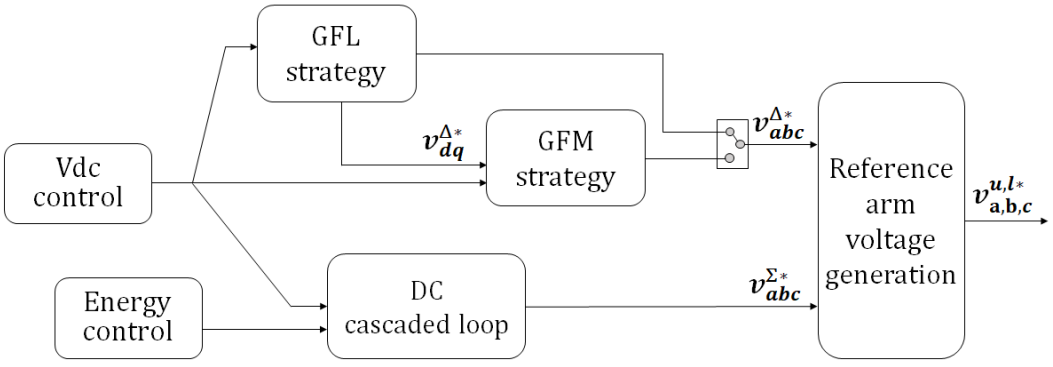


Figure 4.12: Switching from GFL strategy to GFM

Alternative 2: Delayed Restoration

The second alternative involves delaying the MMC deblocking, the reclosing of the DCCBs, and the activation of the Vdc-P droop. However, active power restoration

remains scheduled for 400 ms after fault inception.

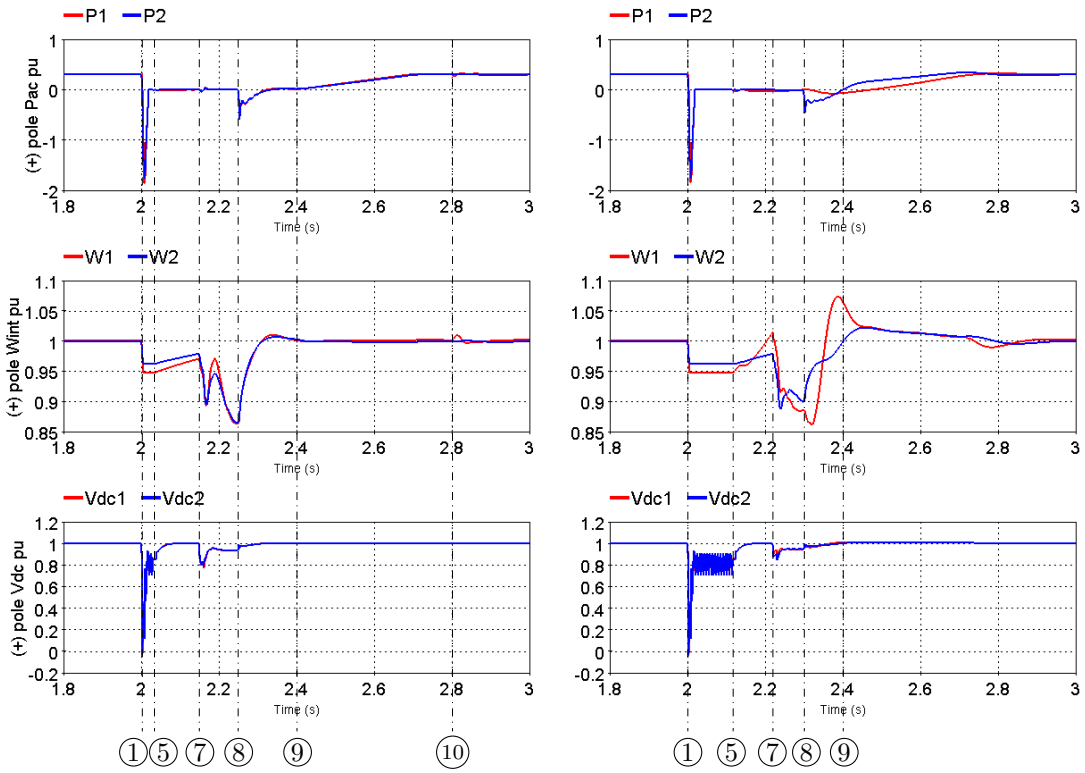


Figure 4.13: Scenario 1 alternative restorations for a short temporary stop

The implementations of the first and second alternatives are shown in the left- and right-hand sides of Figure 4.13, respectively. When deblocking the converter in GFL control, the MMC has no active response towards the AC side state; thus, no significant power exchange is identified when the equivalent power submodule is integrated into the conducting path of the MMC, as seen on the top graph of Figure 4.13. Therefore, the MMC internal energy presents a well-behaved profile, as seen in red. Its difference with the faulty converter at station S_2, in blue, is given by the different energy level found when blocked due to the use of GFM control. GFM control is turned back once the pre-fault power flow is restored at 2.8 s (instant 10), facing a small transient, avoiding any significant internal energy excursion of the MMC.

In the second alternative, right-hand side of Figure 4.13, the converter deblocking is delayed by 85 ms, occurring at 2.115 s (instant 5). This control delay is intended to allow the AC PoC to settle and avoid any significant IR after the power converter

is deblocked in GFM strategy. This is depicted on the right-hand side of Figure 4.13. By this modified timing of the control action, the MMC AC response is rather small, and mainly driven by the DDEC, which takes power from the AC side to manage the converter internal energy. Furthermore, the pre-fault power is ramped up at 2.4 s (instant 9). At this stage, the DC voltage has not yet settled to its nominal value; the slow power swing of the GFM converter during the DC grid re-energization causes the GFL converter to extract more power from the DC system, thereby altering the ramp rate during this period.

The DCCBs reclosing is also delayed to 2.210 s (instant 7), after PIRs bypassing transient, the Vdc-P droop is reactivated at 2.300 s, allowing for the complete MTDC grid re-energization. Furthermore, from the power profiles, it can be seen that the GFL converter (in blue) has a faster response than that of GFM converter (in red), being thus the faster GFL control the main responsible for the MTDC system re-energization, corroborating the analysis done in previous section. Finally, at 2.400 s (instant 9), active power is ramped up.

For the last scenario, i.e., where GFM is the sole strategy regulating the MTDC grid voltage, it is expected that further difficulties in shortening the DC FRT duration will appear, as seen in previous case scenario. This is mainly due to the slower energy controllers used to decouple the control interaction mechanism described in previous section, which allowed the stable operation of the MTDC system with such control coordination.

Figure 4.14 presents both the 400 ms length C&P sequence and an extended one, on its right-and left-hand sides, respectively. The fault clearing is managed as in previous cases, shortly after the fault is incepted at 2 s (instant 1), fault pole converters block approximately at 2.003 s (instant 2). DCCBs open at 2.010 s (instant 3). Similar to previous scenario, the deblocking of the MMCs is delayed to 2.115 s (instant 5). At this stage, DDEC and DDVC take control of MMC internal energy and DC voltage, respectively, until the MTDC grid is reconnected by reclosing the DCCBs with two PIRs at 2.220 s (instant 7).

As discussed earlier, once the MTDC system re-energization starts, bringing power

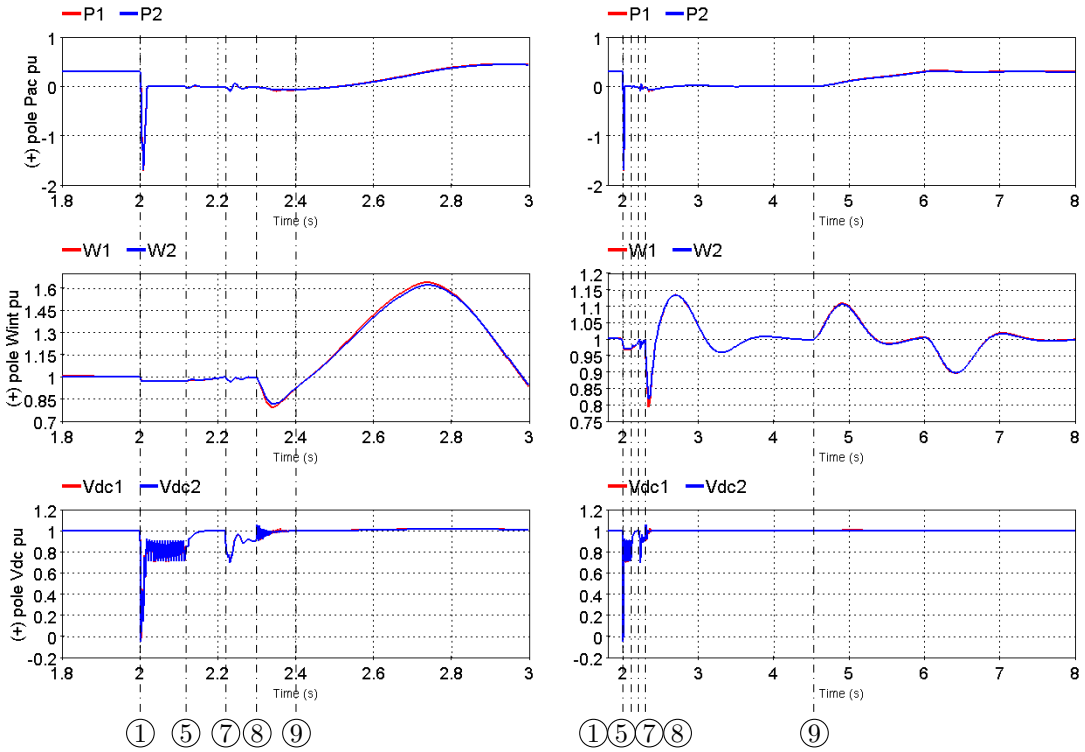


Figure 4.14: Scenario 1 alternative restorations for a short temporary stop

from the AC into the DC system, the sluggish response of both the energy controller and the GFM strategy causes energy excursions that may compromise system MMC safe operation by exceeding operational margins. The results confirm that the duration of the C&P sequence cannot be reduced compared with the previous cases. Therefore, sufficient time must be taken between major power transients to ensure safe converter operation. This alternative is depicted on the right-hand side of Figure 4.14, where the period between the DC grid re-energization and pre-fault power ramp-up is extended. On top right, active power is depicted for the extended DC FRT. It can be seen that the restoration time takes 2.5 s due to the extended periods between the fault clearing and active power restoration. MMC internal energy is seen in the middle right graph.

The fault clearing has not a main variation, with respect to previous cases; nonetheless, once the MTDC system re-energization starts (instant 8), a longer period is taken to initiate the following control command. Due to the mismatch between the power exchange between the AC and DC sides with the MMC, an overshoot in internal energy

is seen, which settles down after around 2.300 s. At 4.5 s (instant 9), active power is ramped up, with a reduced ramp rate, when compared with the previous cases, as done in the first analysis of this case scenario.

The restoration ramp takes 1.5 s to meet the pre-fault power flow. During this period, upper and lower energy excursions are identified, given the slow response of the energy control. While DC voltage is practically sustained to its nominal value few hundreds of milliseconds after the re-energization is initiated, confirming the decoupling of the controllers interaction.

Previous results show that compared with the reference sequence timing with GFL control, an early deblocking can cause the GFM reaction to an unsettled AC PoC and lead to further issues of MMC internal energy. Furthermore, it is important to highlight that no dynamic element has been modelled on the AC system, therefore, the time needed for the disturbance to settle down at the PoC might vary. Therefore, proper studies should be carried out to identify the ideal timing for the C&P sequence coordination. On the other hand, switching to GFL control when deblocking the MMC has shown a well-behaved system response, circumventing the possible issues that the power converter could face in a quick deblocking with GFM control.

As expected, the last scenario showed the limitations of this MTDC system control coordination, where the slow AC response of the GFM strategy, together with a slow energy controller, would challenge a fast recovery. Again, similar to the case with only one converter using GFM control, the modelling of the AC system has been importantly simplified; therefore, a more detailed AC system could offer a view of the possible interactions this control strategy could have. Yet, the presented phenomena would only be amplified or reduced, based on the system damping and other controllers' tuning, as the underlying mechanism would be present.

4.5.4 Use of one AC system to regulate the MTDC grid energy

To facilitate the extended application of GFM control as the primary mechanism for MTDC grid voltage regulation, an alternative strategy has been proposed that partially decouples perturbation propagation from control interactions within the healthy pole

during fault disturbance propagation. This decoupling is achieved by reducing the bandwidth of the energy controller within the coordinated GFM and GFL control architecture of the MTDC system, as described above and illustrated in Figure 4.8.

However, a system-level control perspective offers an alternative to propose another MTDC system control coordination. From this viewpoint, the absence of GFL converters can constrain the MTDC voltage regulation. Good alignment between the DC and AC power flows of a GFL converter facilitates the rapid delivery of power necessary to restore DC voltage whenever an IR is provided by GFM-controlled MMC. This interaction effectively damps the oscillations typically originated by the GFM control strategy.

Examining in more detail the perturbation propagation and control interaction mechanisms described in Figure 4.8, it can be inferred that the Vdc-P droop action remains minor if sufficient energy is available within the MTDC grid to support the GFM converter response. Furthermore, if the converter's internal energy were regulated by the AC system, the propagation of perturbations into the DC system would be reduced, as the main source to replenish this MMC energy would not be the MTDC grid.

Although this approach may conflict with the fundamental objective of providing support to the AC grid via GFM control, the slow dynamics of such an energy controller may facilitate the stable operation of this control architecture, as shown in Figure 4.16. As a consequence, the converter will cause a new perturbation in the corresponding interconnected AC system, in this case, AC system 2, following the control interaction mechanism described in Figure 4.15.

Obviously, this control architecture implies that the outer control loops must respect the rise time of the following controllers in the cascaded loop, similar to the DDEC in previous subsection. Therefore, the energy controller is tuned for a rise time of 2 s. On the other hand, a rather slow energy control might jeopardize the MMC energy levels and proper operation, as the control might be prone to have energy excursions as seen in previous analyses.

The implementation of this MTDC system control coordination is done by using the

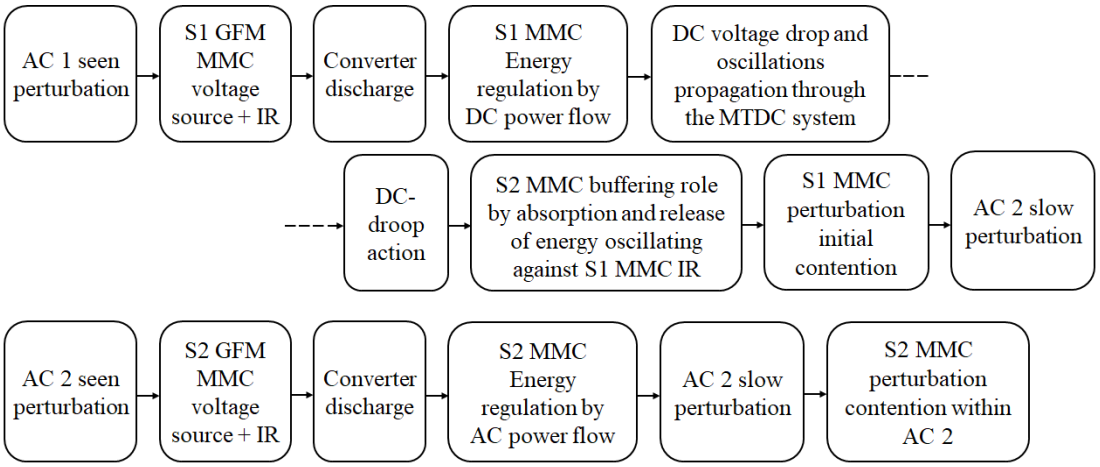


Figure 4.15: Control interaction and perturbation propagation mechanism with GFM and AC side internal energy regulation

proposed control architecture from the previous analysis, presented in Figure 4.16 at converter station S_2; whilst converter station S_1 keeps the control architecture presented in Figure 4.1 with a fast energy controller, i.e., a rise time in the order of tens of milliseconds. Results are presented in Figure 4.17, having the behavior of the healthy pole of converter station S_1 on the left-hand side and converter station S_2 on the right-hand side. As expected, both stations have the voltage source response followed by the IR and damping of the GFM strategy; contrastingly, the impact on the converter internal energy is rather different. The fast energy controller using the MTDC system as energy source has a well controller behavior, having deviations from the nominal value of areound 0.1 pu; whilts the slow energy controller of the MMC at station S_2 has significant excursions slightly larger than 0.2 pu. These results confirm previous analysis.

After the converters have a partial discharge do to their reaction to the AC seen perturbation, the converter with a fast controller causes the MTDC voltage to have a drop close to 0.96 pu, which quickly reaches converter station S_2. At S_2, the initial AC and DC power mismatch leads to a slight increase of internal energy and DC voltage, but the energy used to deliver the IR and the further depletion of DC voltage lead this converter to have a reduced energy level. The low energy poses difficulties for the converter to sustain a proper DC voltage, generating high-frequency oscillations.

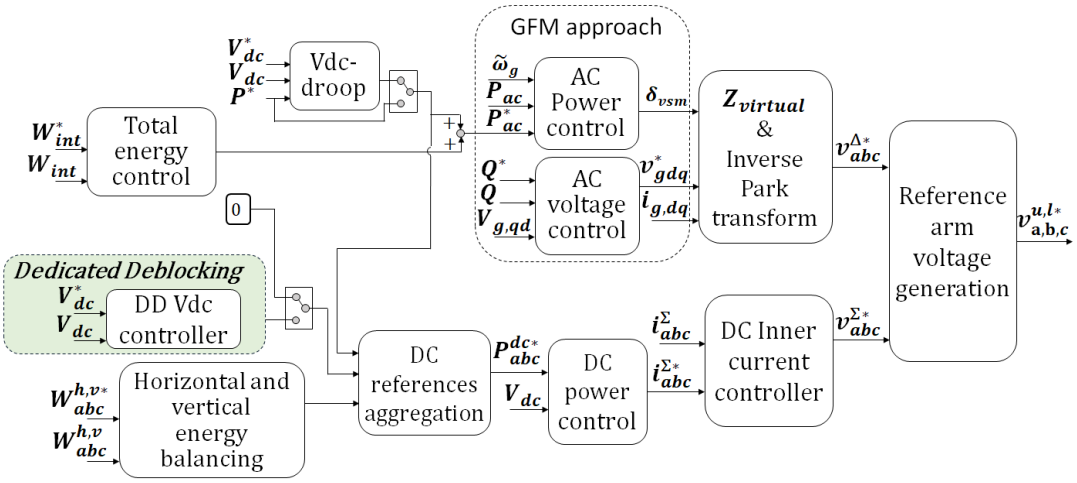


Figure 4.16: MMC GFM control architecture, where the dedicated control to perform the DC FRT is highlighted.

In respects to the faulty pole, results are presented in Figure 4.18 for stations S_1 and S_2, in red and blue, respectively. The fault clearing is presented on the left-hand side, while the restoration process is shown on the right-hand side; both processes follow the generic open-loop sequence presented in Figure 3.2. At 2 s, the fault incepted, instant 1. After the first travelling wave reaches the measuring point, DC voltage drops, converters start to discharge and a few milliseconds afterwards, both converters block, instant 2, bypassing the MMC power submodule, as shown in the zoom-in of each signal.

As seen in the internal energy profiles, the converter with a fast energy controller, at station S_1, takes a longer time to block as the fast controller attempts to sustain the MMC internal energy, thus reducing the rate of change of the fault current, reaching the arm current threshold after the MMC at S_2. Once the MMCs are blocked, current is fed from the interconnected AC systems, as reflected in the power profiles, reaching their peak at 2.010, when the DCCBs are opened, instant 3. After the faulty cable is isolated, and the fault current has extinguished, the MMCs are deblocked at 3.6 s, instant 5, using the DDEC and DDVC, allowing the proper management of the MMCs' internal energy and DC voltage. MMC at S_1 presents a minimum overshoot, while MMC at S_2 controller has a larger one of around 0.03 pu due to its proximity to the

control reference, taking a longer time to settle down with a slow oscillation of around 2.4 s.

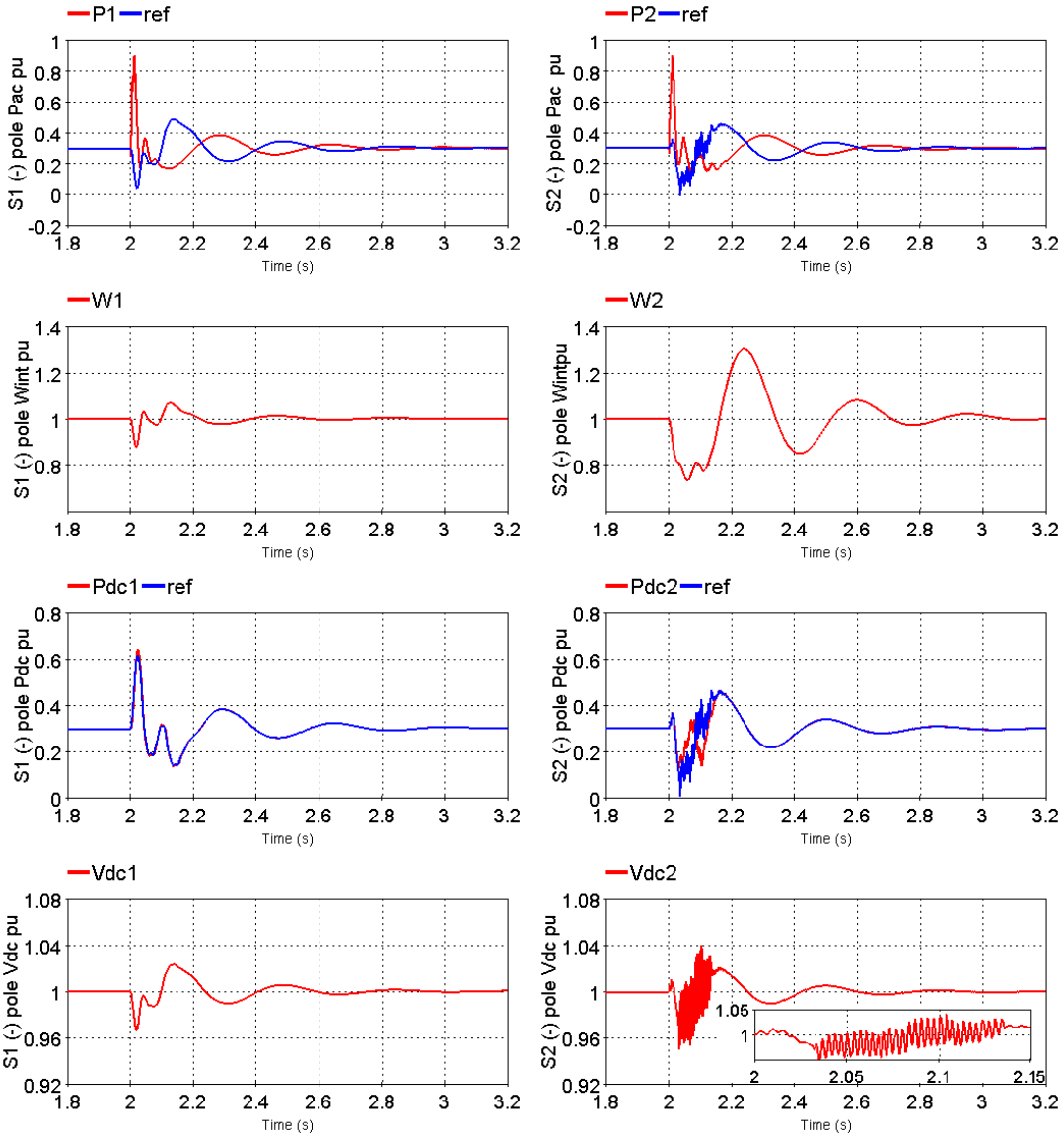


Figure 4.17: Perturbation propagation

DC voltage oscillations originated by the GFM response at S_1, and propagated through the fast energy controller into the MTDC grid, are buffered by the MMC at S_2. Thus, the converter at S_2 reduces and increases its DC power inversion, following the Vdc-P droop command. As its energy controller is rather slow, an overshoot of internal energy is seen in the converter. Approximately after 800 ms, the healthy pole

transient behavior settles down and presents minor variations, as in previous subsection (see Figure 4.10), thus, the restoration process is not presented for this pole.

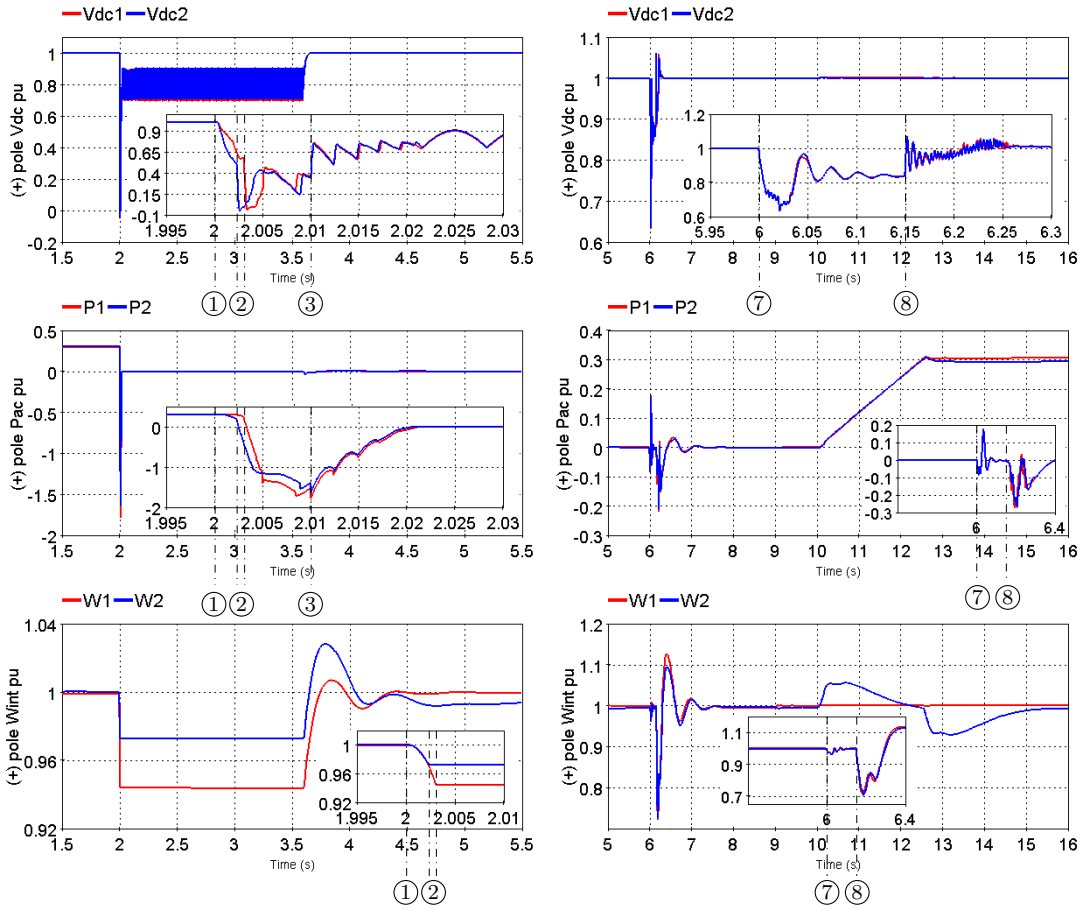


Figure 4.18: Faulty pole DC voltage, active power and internal energy profiles

At 6 s, the DCCBs are reclosed, instant 7, leading to a partial discharge of the converters and DC voltage drop. After the transient caused by the bypass of the PIR, the Vdc-P droops are reactivated at stations S_1 and S_2 to re-energize the MTDC system, at 6.150 s, instant 8. Power from the interconnected AC systems is used causing a new transient. MMCs' internal voltage and DC voltage are then restored. At 10 s pre-fault power is restored with a 2.5 s ramp, avoiding important MMC internal energy at station S_2 excursions; whilst MMC at S_1 presents a well-behaved energy profile.

4.6 Summary

This chapter presented a methodology that allowed the understanding of the dynamic performance of the GFM strategy throughout the MTDC grid as part of the DC FRT analysis in an AC/DC hybrid system using a non-selective DC protection philosophy. The methodology allowed for highlighting inherent problems in this MTDC grid control coordination, and solutions to manage them were tested and validated.

The energy-based MMC control in GFM with Vdc-P droop has shown characteristic responses along the hybrid system DC FRT. The AC inertial support of the VSM imposes further constraints on the MMC operation, particularly on its energy regulation.

The IR is linked to the power mismatch between the converter output and its reference, mimicking the power mismatch between the mechanical and electrical power of a SM facing the AC disturbance caused by the DC fault. Consequently, the healthy converter internal energy depletion will be correspondent to the given AC inertial support. Therefore, for HVDC MMCs, the energy reservoir within the power submodules will constrain the possible inertia constant, H, values to deliver an IR.

Contrasting with the characteristic firewall effect of the HVDC system using GFL control, the interaction mechanism between GFM and the Vdc-P droop was identified as part of the perturbation propagation within the hybrid system. The slow AC dynamics of the VSM reduce the MMC's power sensitivity to DC voltage variations, allowing the faster GFL control to supply the requested power by the MTDC grid. As such, oscillations in the GFL MMC are a control interaction between GFM and GFL as shown in the perturbation propagation mechanism in Figure 4.8, which allow the GFM-originated power oscillations to be damped.

These challenges, inherent to this GFM approach, stem from the VSM dynamics and interdependencies within the hybrid system. Therefore, the proposed solution, i.e., the partial decoupling of the energy control from the IR, allows for the VSM damping and the Vdc-P droop action to quickly settle, avoiding further interaction between converters and the interfaced AC systems.

Two distinct decoupling strategies were analyzed and experimentally validated with

EMT-type offline simulations, both of which demonstrated satisfactory performance regarding the DC FRT capabilities of the system. However, the implementation revealed critical limitations regarding internal energy management:

- Energy Controller dynamics: the utilization of a slow energy controller introduced significant challenges in maintaining an efficient internal energy balance within the MMC
- Operational constraints: due to these control delays, the converter exhibited a restricted operational range, as the MMC struggled to regulate its internal energy effectively during rapid transitions

This suggests that while the decoupling successfully enables the normal operation of GFM as the sole strategy regulating the MTDC system DC voltage, during fast transients, the performance of the MMC is ultimately bottlenecked by the bandwidth of the energy control loop, highlighting the limits of a conventional MMC architecture to deliver AC and DC simultaneous services.

On the other hand, regardless of the chosen control strategy, GFL or GFM, minimum necessary control actions must be implemented to ensure safe converter operation along the system DC FRT. Thus, the proper regulation of the MMC energy must be achieved at all times.

Chapter 5

DC FRT with partially selective protection

5.1 Chapter introduction

This chapter presents two main contributions to the DC FRT analysis: a methodology for developing a partially selective protection strategy in a minimum mesh MTDC system, benchmarked against GFL control; and the analysis of the integration of GFM control to better understand different system-level implications of the protection strategy and together with this control strategy.

The fundamental elements of the partially selective protection philosophy reviewed in Chapter 2 are applied to perform an initial segmentation of the MTDC grid. This initial segmentation considers three main scenarios and is validated through two key processes: the sizing of DCRs using a converter blocking methodology, and the definition of coordinated C&P actions to properly clear DC faults. The C&P coordination is further detailed and modeled for the most complex of the three scenarios. Simulation results serve a dual purpose: they corroborate the analysis conducted during the development of the protection strategy and provide a benchmark for the integration of GFM control.

The integration of GFM control is carried out gradually, following the study methodology presented in previous chapter (Figure 4.2). First, GFM in Vdc-P droop mode is

integrated at one converter station, enabling a better understanding of MMC control dynamics under the electrical circuit constraints imposed by the partially selective protection strategy. This is followed by a summary of system-level implications of GFM in Vdc-P droop control integration. The analysis highlights critical challenges that arise when GFM control is used as the sole strategy regulating DC voltage, and presents a fundamental solution to address them. A proof of concept is presented and illustrated in a simplified manner.

With respects to the modelling approach, a bipolar minimum mesh is employed, as depicted in the single-line diagram in Figure 5.1. All converter stations are rated 2,000 MW, DC voltage of 525 kV, and one averaged value model per arm, equivalent to 400 submodules, giving an MMC electrostatic constant of 0.04 s, while the metallic return is grounded at S_1 only. The GFL and GFM control schemes, used in S_1 and S_2, are implemented as presented in Chapter 2 and the V/f control are implemented in S_3 and S_4, by fixing to 1 the frequency reference in the GFM power synchronizing control loop. OWFs are modelled as a controlled current source interconnected to a split bus in the offshore converter station, representing the grid side converter of the aggregated wind turbines, since the focus of the studies is on a system-level approach.

5.2 Implementation of the partially selective protection strategy

A comprehensive protection strategy can be architected by leveraging the foundational principles of the partially selective protection philosophy, as detailed in Chapter 2. The initial phase of this development requires a critical assessment of the converters' roles within their interconnected AC systems. By evaluating their system relevance, operators can define specific criteria to ride through the DC fault. In this specific case study, onshore MMCs are expected to ride through DC faults and remain in continuous operation given their role in maintaining frequency stability and voltage support; these MMCs are assigned the highest operational priority within the MTDC network. As a consequence, DCCBs are considered only for the onshore DC switching yards.

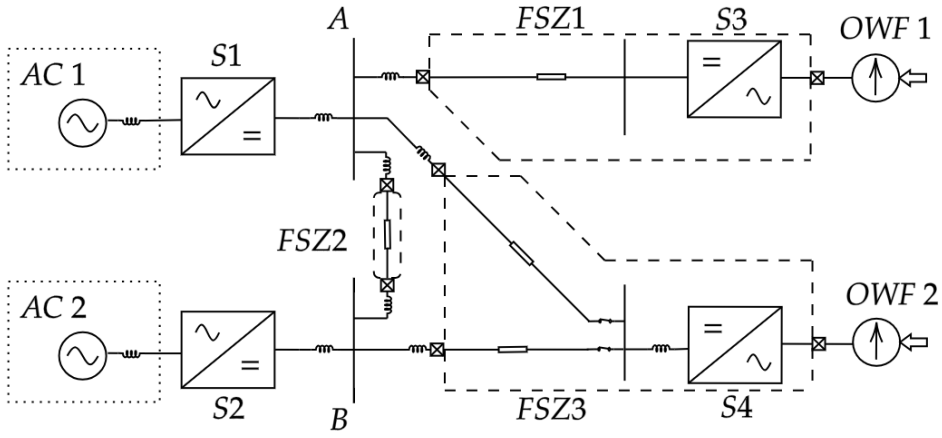


Figure 5.1: MTDC system single line diagram with partially selective segmentation

Figure 5.1 presents the proposed segmentation of the MTDC grid. Due to topological characteristics, the branch interconnecting S_3 to the MTDC system is considered a single FSZ; this radial interconnection defines the FSZ1. FSZ2 is defined based on the relevance of the interconnected AC systems and a hypothetical higher fault occurrence probability; thus, the transmission cable connecting converter stations S_1 and S_2 is treated as a single FSZ. The remainder of the MTDC grid is aggregated into one FSZ, containing two FIZs, one per transmission cable.

With the proposed MTDC grid segmentation, under the partially selective protection philosophy, a pole-to-ground fault in FSZ1 would imply the permanent stop of the faulty pole converter, while the power infeed from the interconnected OWF can be rerouted through the healthy pole, considering control and switching actions, including synchronization. The converter rating would limit the maximum power from OWF1 thereby may necessitating wind power generation curtailment. A pole-to-pole fault would imply the loss of the complete bipole station S_3. Therefore, fault contingencies in this zone imply the permanent stop of the faulty poles' MMCs.

FSZ2 is defined due to the operational priority of the onshore converters and a hypothetical higher fault probability in this cable section, for which maintaining DC voltage control is essential for overall MTDC operation. This fully selective zone enables continuous operation of the MTDC system without temporary interruption.

In FSZ3, a fault occurring in either of the two cables results in the temporary

blocking of the faulty pole converter at station S_4. In addition, due to the operational prioritization of the onshore converters, DCCBs are installed only at the onshore switching stations. At the offshore station, on the contrary, only DC disconnecting switches are considered. These devices require a low current level to operate (a few Ampères), which implies that fault current must be extinguished before disconnection switches can be opened [105], [118]. The fault current contribution from the OWFs is interrupted by the ACCB on the AC side of the offshore system, while the fault current contribution from the healthy MTDC through the DMR is interrupted by a lower voltage rating DCCB, an example of a mature technology for this task, is the metallic return transfer breaker (MRTB), a lower-cost solution [114].

5.2.1 Main protection parameters interdependencies

The continuous operation of the two main MMCs within the MTDC system, i.e., converter stations S_1 and S_2 is assured by keeping the current flowing through each of the converter's arms under a certain safe threshold. This can be achieved in different ways, specifically, three main and complementary protection parameters can be assessed to deliver the expected performance of power converters during a DC fault, i.e., the MMC submodules' overcurrent capability, fault neutralization time, and size of DC current limiters, conventionally considered as DCRs [102]. The definition of one of the three parameters will influence the other two, increasing or reducing the stringency set on the remaining protection elements' parameterization. This is schematically presented in Figure 5.2 [102]. For example, a high arm current blocking threshold reduces the need for large DCRs or faster DCCBs, while high-speed DCCBs reduce the requirement to limit the fault current rate via DCRs, allowing for smaller DCRs and a lower arm blocking threshold, as the fault current transient would not evolve to reach its maximum peak value due to the fast action of the DCCBs.

For illustration purposes, this study employs a blocking threshold of 1.5 pu (3 kA) for the converter arm current. Furthermore, a DCCB opening time of 5 ms is assumed as a baseline for protection coordination. While faster opening times —ranging between 2 ms and 4 ms— have been documented in recent literature [107], [109], the 5 ms

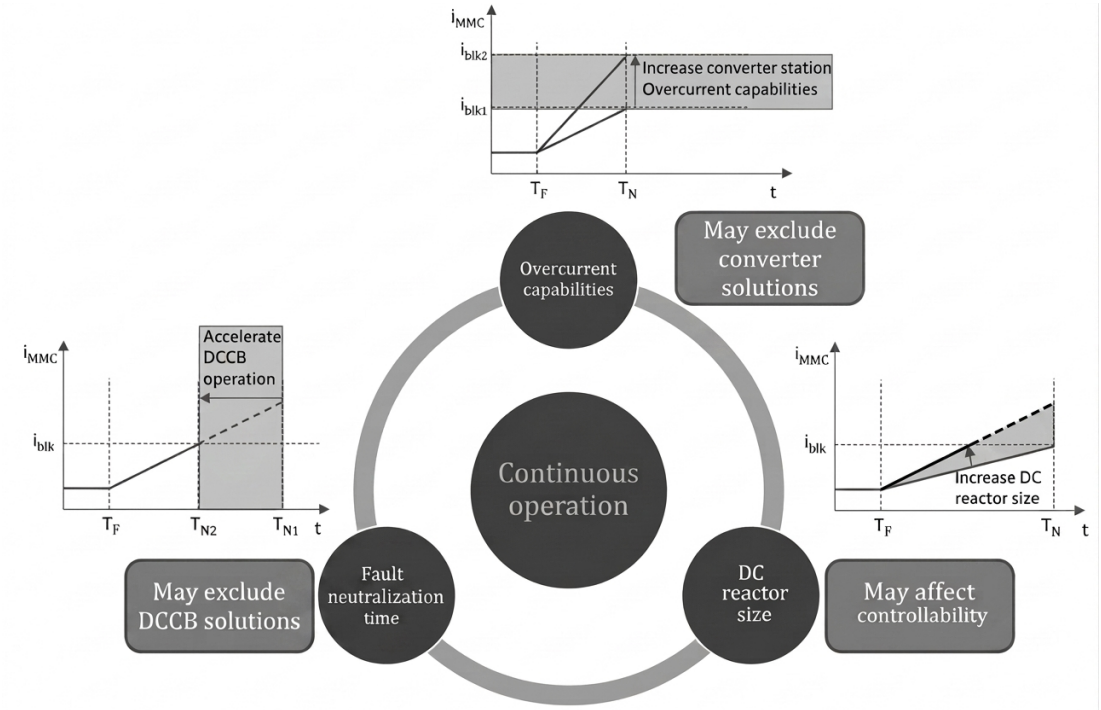


Figure 5.2: Interdepence between system-level protection parameters considering MMC continuous operation [99]

assumption provides a safety margin that accounts for relay calculations, potential communication delays and mechanical tolerances in standard industrial equipment. Of course, exhaustive testing should be performed across various operating points, including the maximum rating, and at different fault locations; nonetheless, in this work only illustrative cases are depicted.

5.2.2 DCRs sizing

The proposed grid segmentation has been developed in accordance with the fundamental principles of partially selective protection, a strategy that balances system reliability with reduced component costs. However, comprehensive validation remains necessary to address the non-linear trade-offs in DCR sizing, where inductance must be sufficient to suppress the fault current's rate of rise (di/dt) without compromising system stability. Furthermore, properly timed coordination of C&P actions must be developed to ensure that converter control effectively interfaces with protection relays and prevent

blocking of selected power converters.

Since the fault neutralization time is pre-defined at 5 ms following a fault event, the DCR sizing is determined using a converter blocking methodology. This process involves simulating pole-to-ground faults within each FSZ to evaluate system resilience. Specifically, the response of the corresponding MMCs is monitored to determine their operational state—identifying whether they maintain continuous operation or their blocking is triggered, as illustrated in Figure 5.3. Furthermore, the ACCBs action is not presented as the objective in this subsection is to identify the blocking performance of the power converters within the MTDC system.

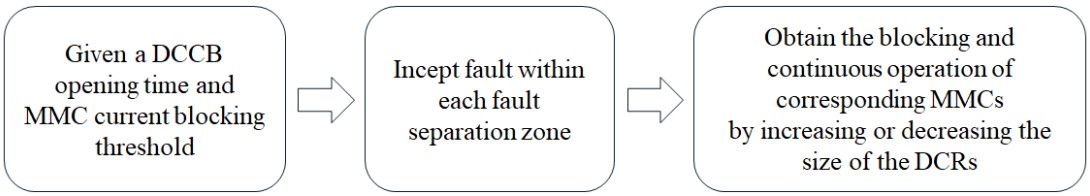


Figure 5.3: DCRs sizing methodology

Alternatively, the interplay between the three primary protection parameters allows for diverse design methodologies [137]. For instance, one approach can begin with the delimitation of FSZs, accounting for control-area liabilities, and MMC blocking characteristics. This is followed by an assessment of permissible steady-state losses to determine the optimal sizing of DCRs. Subsequently, an appropriate DCCB opening time is selected from available technological options. This sequential prioritization is necessitated by the fact that the maximum current capability of converter valves is currently a critical design constraint, offering less flexibility for adjustment compared to other system parameters.

The purpose of this work is to illustrate key aspects of DC FRT operation, including GFM converter stations in the MTDC, rather than to optimize the protection strategy. Therefore, the analysis is limited to a single representative fault per cable, while comprehensive testing would be needed to determine optimal values in a real system. Therefore, a pole-to-ground fault is incepted at the midpoint of each cable of the MTDC system, i.e., one DC fault within FSZ1, one within FSZ2, and two within FSZ3, the

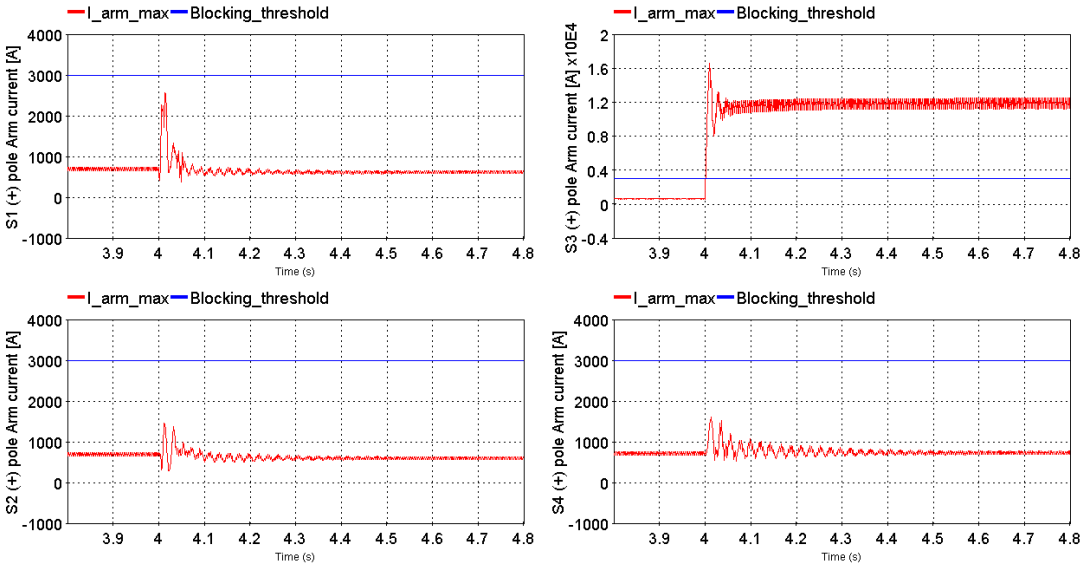


Figure 5.4: Fault test at FSZ1

first one in the cable connected to busbar A, and the second in the transmission cable interconnected to busbar B.

Simulation results for FSZ1 are illustrated in Figure 5.4. As anticipated, a fault occurring at the middle of the branch interconnecting the offshore station S_3 triggers a rapid surge in fault current throughout the MTDC system. However, proper sizing of the DCRs across the grid ensures that MMCs outside the affected FSZ maintain continuous operation. In this case, the FSZ1 DCR is sized to 250 mH. These converters experience only a brief transient and successfully return to their pre-fault steady state within a few hundred milliseconds. Conversely, as seen in the upper-right corner, the maximum arm current of MMC at S_3 exceeds the 3 kA blocking threshold in around 3 ms, triggering its blocking.

Owing to its central proximity to converter stations S_1 and S_2, FSZ2 serves as a critical junction for the protection of the entire MTDC grid. Specifically, this zone demonstrates the application of a fully selective protection philosophy and its expected performance. In this protection configuration, the cable interconnecting the two nodes is equipped with one DCCB at each cable end. This setup aims to isolate faults strictly within the protected zone, thereby ensuring the continuous operation of the remaining MTDC system.

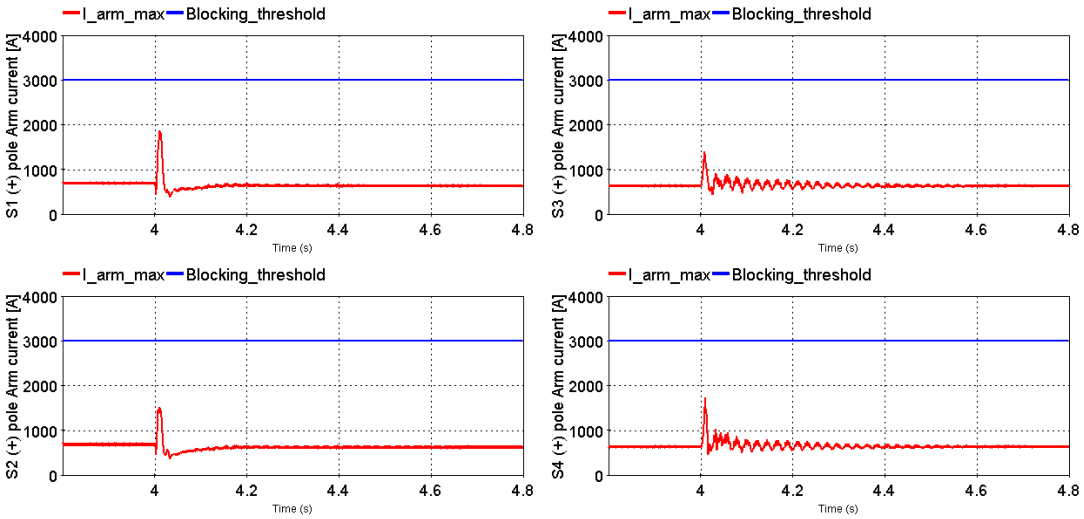


Figure 5.5: Fault test at FSZ2

The obtained simulation results for a DC fault test conducted within FSZ2 are depicted in Figure 5.5. As anticipated, the grid exhibits significant resilience: all MMCs experience only a minor transient, with arm currents successfully suppressed below the blocking threshold. Consequently, every MMC in the network maintains continuous operation without triggering a blocking action. Notably, the peak fault current within each converter arm remains below 2 kA, more than 1 kA under the blocking threshold. Nevertheless, due to the cable location within the MTDC grid, these inductors are relevant not only for FSZ2, but for the overall MTDC system protection strategy's proper performance.

For FSZ3, the protection strategy is validated through two separate fault tests, each located at the midpoint of the cables within this zone. The first test is done in the cable interconnecting converter stations S_1 and S_4; while the second fault test is performed in the cable interconnecting stations S_2 and S_4. In both scenarios, the protection strategy is designed such that only the converter at station S_4 is permitted to block.

Obtained results, presented in Figures 5.6 and 5.7 for the first and second tests, respectively, confirm that the calculated DCR sizes successfully satisfy the required system behavior. Specifically, the reactors provide sufficient current limiting to ensure the continuous operation of the MMCs at converter stations S_1, S_2, and S_3 throughout the fault transient.

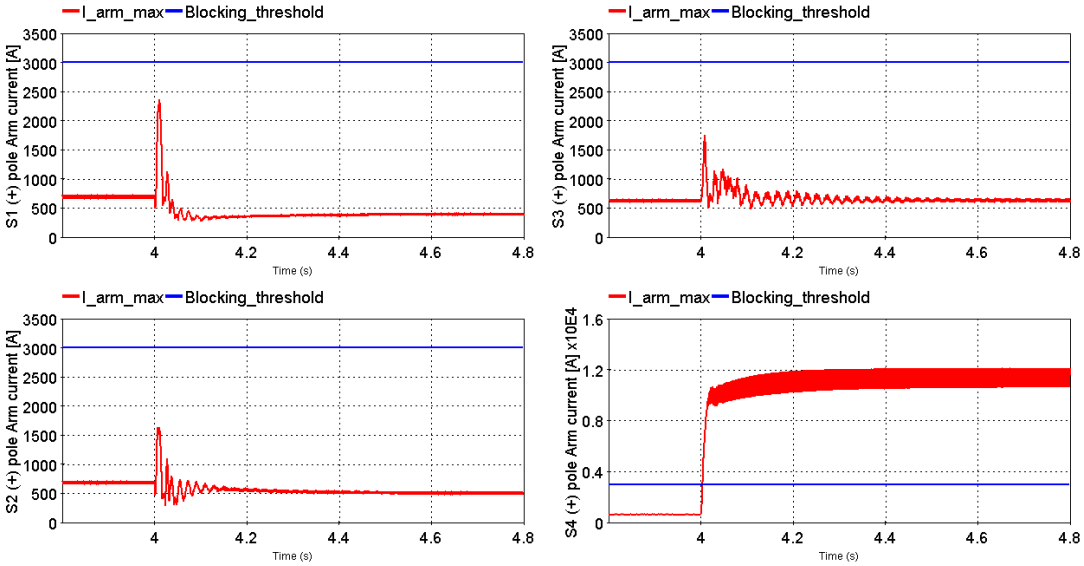


Figure 5.6: Fault test at FSZ3 A

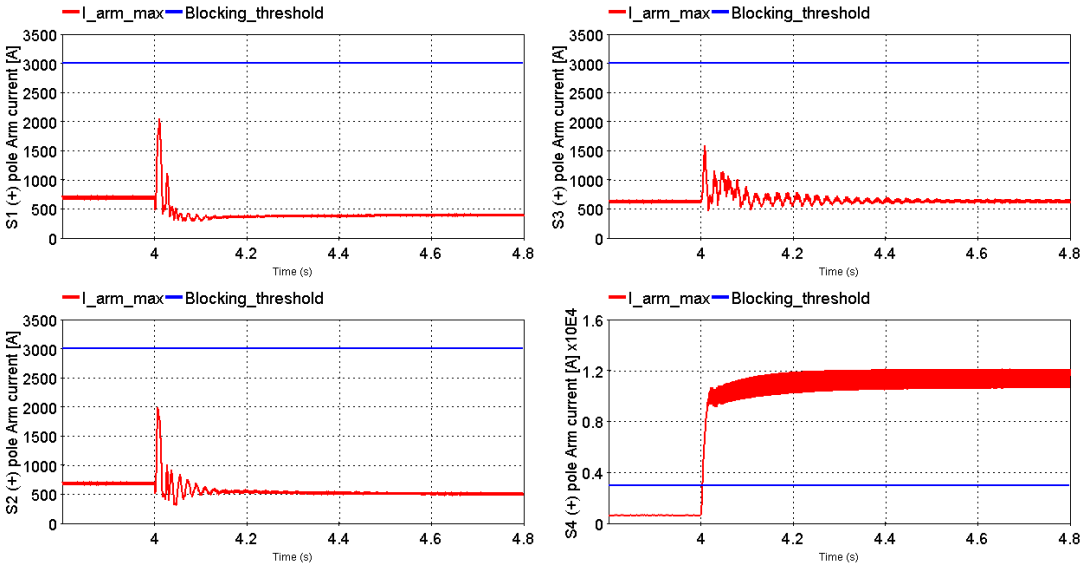


Figure 5.7: Fault test at FSZ3 B

The obtained inductance values are summarized in Tables 5.1 and 5.2. The high DCR values are due to the relatively slow opening time of the DCCBs [137], while the lower DCR value at S_1 compared to S_2 is related to the capacitance of the transmission cables connecting the feeders. Longer cables allow more current to sustain the DC voltage at bus A, resulting in a lower fault current peak, thereby naturally limiting the fault current peak and reducing the need for additional lumped inductance.

Furthermore, the large size of DCRs would impact both the initial capital expenditure (CAPEX) and daily operational expenditure (OPEX). Additionally, the integration of multiple line inductors fundamentally alters the DC grid dynamics. These new dynamics are directly driven by the strategic placement and sizing of the DCRs. Thus, the control challenges for the MTDC converters and the overall MTDC system stability will be different when compared with the previous protection strategy, analyzed in Chapter 3. Thus, a re-assessment of the control tuning is foreseen under these new electrical characteristics of the DC circuit.

Table 5.1: DCRs size at each converter station

Converter station	**DCR [mH]**
S_1	200
S_2	350
S_3	250

Table 5.2: DCRs size per FSZ and bus bar

FSZ	**Bus A DCR [mH]**	**Bus B DCR [mH]**
1	200	-
2	275	275
3	200	200

5.2.3 DC FRT C&P coordination

Once the main characteristics of the electrical circuit are defined, the dynamic behaviour of each phenomenon can be characterized and understood. Following the study methodology developed in previous chapters, the dynamic behaviour of each phenomenon in

the DC FRT analysis can be characterized by implementing GFL in the onshore converter stations (S_1 and S_2), then a comparison with GFM control can be carried out. The DC FRT is comprised of three main stages, as presented in the flow diagram in Figure 2.16. Fault detection is typically performed at each measuring point by protection relays considering local measurements and no communication with other protection devices [138]. For the analysis of the dynamic system performance along the DC FRT, two main stages are considered: the fault clearing and the restoration process [93].

Fault clearing and management of offshore loss of power infeed

The fault clearing and restoration processes are dependent; nonetheless, the main steps within each stage are based on the used protection philosophy. For the partially selective protection strategy proposed in this chapter, the focus is on a fault occurring within FSZ3, where C&P coordination is the most complex in the MTDC, particularly on the offshore side. In this scenario, the sequence of events and associated phenomena during fault clearing under the partially selective protection strategy proceed as follows:

- Fault occurs within FSZ3
  - DC voltage drops in the protection zone
    - Current increases through DCCBs
    - S_4 faulty pole MMC starts its discharge
      - Arm current increases, and converter blocks
      - Offshore reference voltage is lost (V/f control is lost)
      - The offshore AC network starts to feed current
      - OWFs start islanded operation with low voltage ride-through (LVRT)
- Faulty section isolation
  - DCCBs open
    - Fault current fed by the MTDC through the high voltage cables is suppressed

  - ACCBs open
    - Fault current infeed from offshore AC system is suppressed
  - Lower rating DCCB in the DMR opens
    - Fault current infeed from the MTDC healthy pole through the DMR is suppressed
  - DC disconnecting switches are opened, and faulty cable is isolated

The management of the loss of power infeed from the OWF occurs in parallel with the ACCB opening. Furthermore, three main alternatives are identified based on possible C&P coordinated actions: no loss, minimum temporary loss, and permanent loss.

- Management of the loss of infeed – ACCB is opened
  - No loss: reroute OWF production through the healthy pole
    - Seamless transition is achieved having adequate control and connection to the healthy pole feeder, with smooth synchronization. The pre-fault power generation is under the offshore HVDC MMC rating
  - Minimum temporary loss
    - OWF power dissipation: by means of crowbar, OWF DC chopper, OWF AC dynamic braking system (DBS), another DBS at the offshore AC switching station [139]
    - Possible OWF generation curtailment: blades pitching and rotor yawing [140]
    - OWF power re-route through the healthy pole
  - Permanent stop
    - Trip of the OWF, considering initial dissipation, power generation reduction and shutdown

Restoration process

The restoration process requires the re-energization of the remaining healthy section within the FSZ3, necessitating proper coordination among all the switching units, the HVDC system and the OWF. Therefore, the complete restoration sequence will depend on how the loss of power infeed is managed. In this case, as the focus is on a system-level perspective, the restoration sequence considered is as follows:

- MR DCCB reclosing
- DCCB reclosing (with properly sized pre-insertion resistors)
  - The remaining healthy section of the FSZ is re-energized by the healthy MTDC, where the main onshore converters are responsible for DC voltage regulation
- Deblock offshore HVDC MMC in V/f control
  - Synchronized ACCB reclosing
- Return OWFs to normal operation, and disconnection from the AC side healthy pole

5.3 Reference case scenario – GFL control

The focus of this work is on the system dynamic performance along the DC FRT when integrating GFM as the sole strategy regulating the MTDC system voltage. Therefore, the gradual inclusion of GFM in this thesis follows the study methodology proposed in the previous chapter and depicted in Figure 4.2, while the OWFs modelling is simplified to an aggregated turbine, considering only the grid-side converter. Thus, the OWFs are represented by a simplified voltage source converter controlled as a current source. This modelling approach allows the MTDC system to see the temporary loss of power-infeed, expected from the OWFs FRT and the corresponding AC voltage variations at the offshore HVDC converter. A more detailed representation of the OWF can refer to [93], where the OWFs' control is revised in a more detailed manner.

The required C&P sequence to operate the system DC FRT is shown in Figure 5.8. Following this sequence, the reference system behaviour during DC FRT with the partially selective protection strategy is shown in Figure 5.9, where the FSZ3 breakers' opening is triggered in sequence: the two onshore DCCBs, the offshore ACCB, and the MR DCCB. After the fault inception at 4 s, the currents through the DCCBs at buses A and B rise rapidly and reach a peak of about 6 kA before the breakers open at 4.005 s. Once the fault current contribution from the rest of the MTDC network is interrupted, the currents at buses A and B decay to zero within approximately 25 ms. On the offshore side, the ACCB opens after four cycles (80 ms), suppressing the AC fault current. The MRTB opens after about 600 ms, a delay mainly due to its 600 A rated current threshold [114], which can vary depending on the available technology and system requirements [34], [105], [107], [141]. After all breakers have opened and the fault current is fully suppressed, the DC disconnectors can operate to isolate the faulty section.

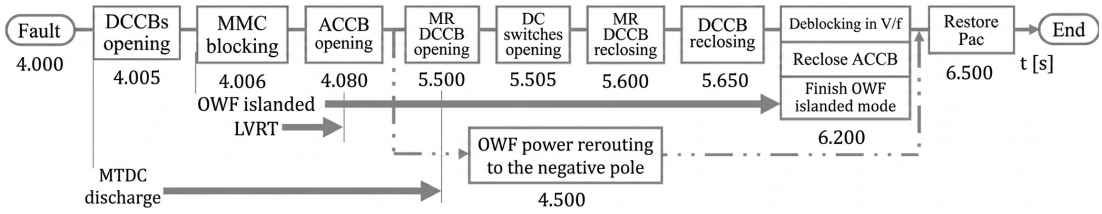


Figure 5.8: DC FRT C&P sequence for a fault in FDZ3

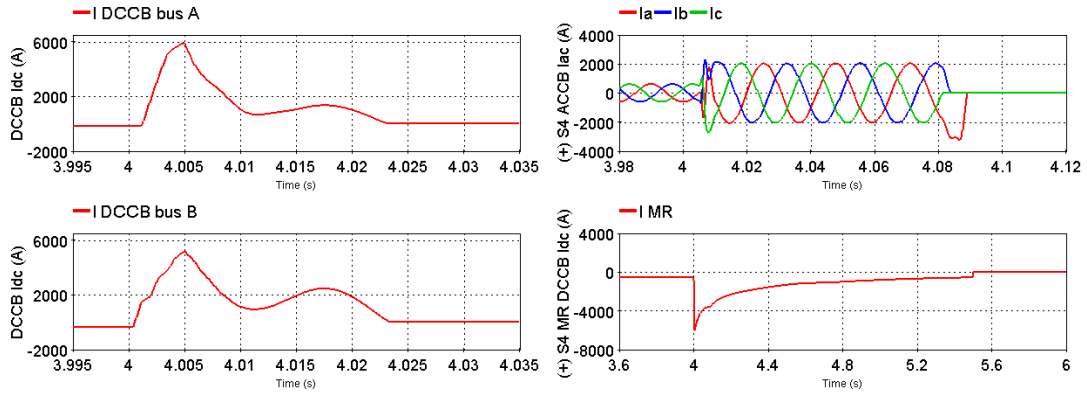


Figure 5.9: Fault current neutralization in FSZ 3

It is important to recall that the offshore AC side is out of the scope of the core

analysis of this thesis. Therefore, the presented results only delineate on a high-level the expected behavior. Figure 5.10 illustrates the offshore grid behaviour during the fault event. On the left-hand side, the OWF d- and q-axis current components are shown together with their control references. To minimize temporary power loss, wind power is initially dissipated and curtailed immediately after fault detection, until it is rerouted through the healthy pole, provided that the MMC power rating is not exceeded. During this interval, the d-axis current is set to zero and remains so until power rerouting occurs at 4.5 s.

At the same time, the OWF must provide LVRT support to the AC grid while the V/f control is lost. This support is achieved by injecting q-axis current after the loss of V/f control, with the MMC operating as a diode rectifier, until the ACCB opens. As a result, a small AC voltage is maintained on the OWF side, ensuring that the OWF remains connected. Once the ACCB opens, the OWF enters full islanded operation, as reported in [18].

The right-hand side of Figure 5.10 shows the three-phase voltage waveforms of the faulty S_4 MMC and the OWF. The DCCB opens at 4.005 s, with the subsequent opening of the ACCB observed approximately 80 ms after fault inception. Following DCCB reclosing and FSZ3 re-energization, an offset appears in the MMC AC voltage while the ACCB remains open. At 6.2 s, the offshore MMC is deblocked, and V/f control is restored, re-establishing the offshore AC voltage reference and enabling recovery of the pre-fault power flow through this pole. For the OWF AC voltage, a short transient occurs when the ACCB opens and the OWF is connected to the healthy pole feeder. A final small transient is observed during reconnection to the original pole.

Figure 5.11 illustrates the MTDC behaviour along the DC FRT. The left-hand side shows the DC voltage and active power of the faulty pole, while the right-hand side presents the healthy pole. When the fault is initiated at 4 s, a transient propagates through the entire MTDC system. The opening of the DCCBs prevents further fault propagation to other FSZs. As expected, the voltage at station S_4 drops to zero and remains there until the MR DCCB opens, creating a temporary potential difference between the DMR and the faulty converter, as seen in Figure 5.11.

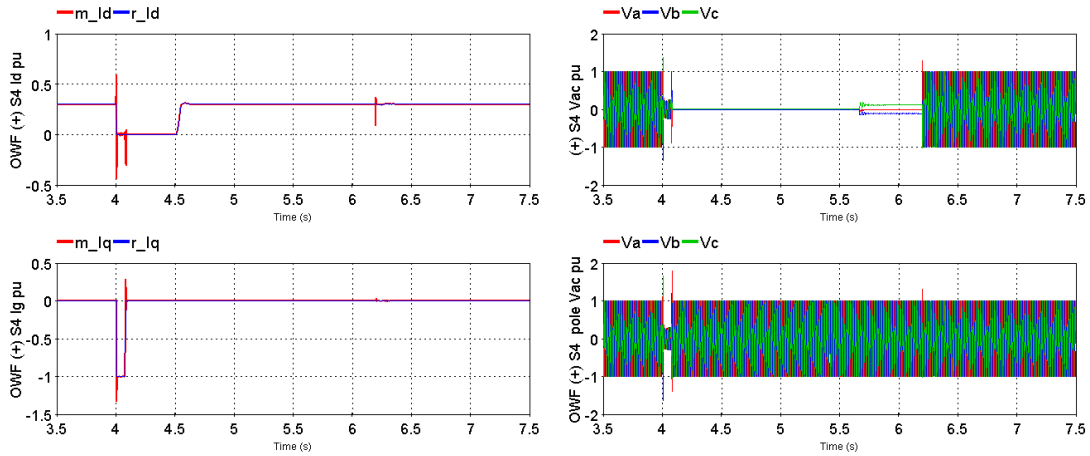


Figure 5.10: Offshore DC FRT overview

This potential disappears once the MRTB is reclosed. After the DCCBs are reclosed, a transient of approximately 100 ms occurs due to the operation of the pre-insertion resistors and the re-energization of the remaining FSZ3. Another transient appears at 6.2 s when the faulty S_4 converter is deblocked under V/f control. The subsequent restoration of power flow through this pole activates the droop control, leading to an increase in MTDC voltage consistent with a 10% power flow variation.

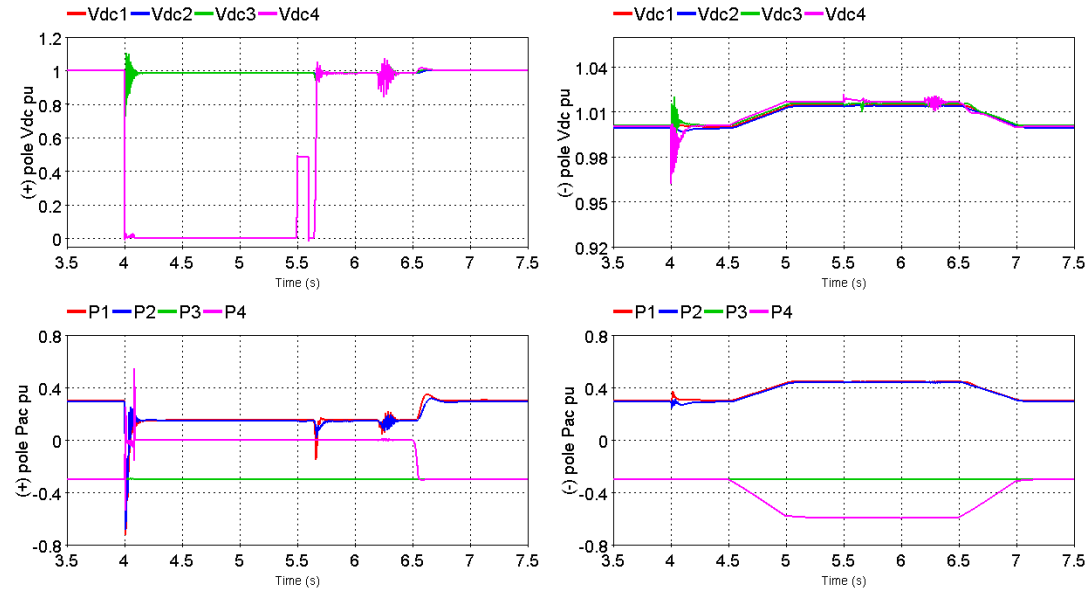


Figure 5.11: MTDC Vdc & Pac

Active power profiles of the faulty pole show that the temporary loss of power infeed results in a shared reduction of power export at the onshore stations, as both operate with the same droop setting. Short transients are observed during DCCB reclosing and MMC deblocking, also reflected in the DC voltage waveforms. The healthy pole presents minimum impact, and power rerouting effectively limits the loss of power infeed. Once the wind-generated power is rerouted through this pole, the MTDC voltage changes by about 0.015 pu, as each converter accommodates an additional 0.15 pu of the power previously injected through the positive pole.

5.4 Integration of GFM control with a partially selective protection

In this section, the gradual inclusion of GFM control in the converter stations of the MTDC grid is carried out, where stability issues are presented and mitigation solutions to the C&P are provided. In Chapter 4, it has been analyzed that the support provided by GFM in Vdc-P droop mode to its interconnected AC and DC systems is limited by both control and physical interdependencies. In particular, the MMC's cascaded AC control loop exhibits a relatively slow response due to the GFM operation, whereas the DC control loop is mainly constrained by the inner current controller. This mismatch between AC and DC dynamics creates an inherent conflict in the MMC control architecture, making the system prone to oscillations in AC/DC power exchange during transient events. As a result, an MMC operating in GFM mode faces challenges in properly balancing AC and DC power flows while simultaneously regulating its internal energy and the MTDC voltage during large disturbances, e.g. DC faults.

5.4.1 GFM control only in station S_1

Compared to non-selective approach presented in Chapter 4, the partially selective protection strategy requires a greater number of DC reactors with larger ratings to be installed in the network, resulting in new dynamic behaviour in the DC system. To implement GFM control in Vdc-P droop mode as the sole DC voltage regulation strat-

egy, combined with an energy-based controller, a partial decoupling of the controllers' interactions was needed. To this end, the use of reduced inertial support with high damping, and a slow energy controller were adopted as control tuning guidelines for the MMC cascaded control. The VSM parameters were set to an inertia constant of $H = 1.5$ s and a damping coefficient of $k_d = 150$, while the rise time of the internal energy controller was set to $t_r = 800$ ms. This control configuration is adopted as the baseline for integrating a GFM converter with the proposed protection strategy.

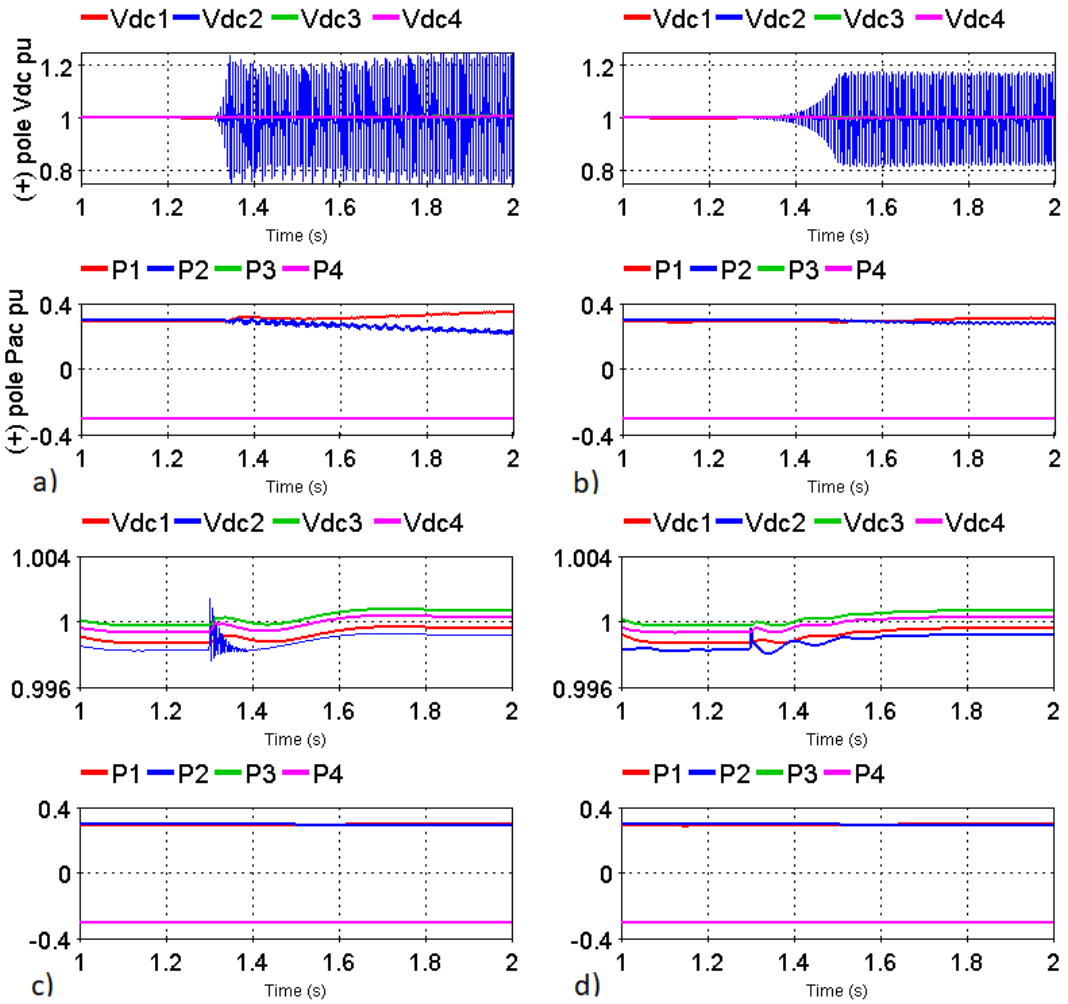


Figure 5.12: Positive pole MTDC Vdc & Pac for different energy control rise times. a) $t_r = 800$ ms b) $t_r = 200$ ms, c) $t_r = 130$ ms and d) $t_r = 30$ ms

After the activation of the droop control at 1.3 s, station S_2 exhibits high-frequency oscillations (see Figure 5.12, a). A slower controller may jeopardize the MMC operation;

whilst a faster control (Figure 5.12, b) t_r = 200 ms, c) 130 ms and d) 30 ms) provides rapid corrections that compensate for the DC reactors and restore stable operation. Based on this trend, a rise time of t_r= 50 ms is adopted for the remainder of the section.

5.4.2 GFM oscillatory behaviour

Similar to the non-selective protection strategy case, the inclusion of a GFM converter at one station increases the further perturbation propagation throughout the hybrid AC/DC system. In this scenario, the DC voltage drop induces the Vdc-P droop mechanism, while the mismatch between AC and DC power-flow dynamics gives rise to a series of oscillations, which are finally damped with the GFL converter support. Nevertheless, the adopted control parametrization exhibits a noticeably oscillatory response following the large disturbance, indicating that the system is operating close to its stability margins, as illustrated in Figure 5.13.

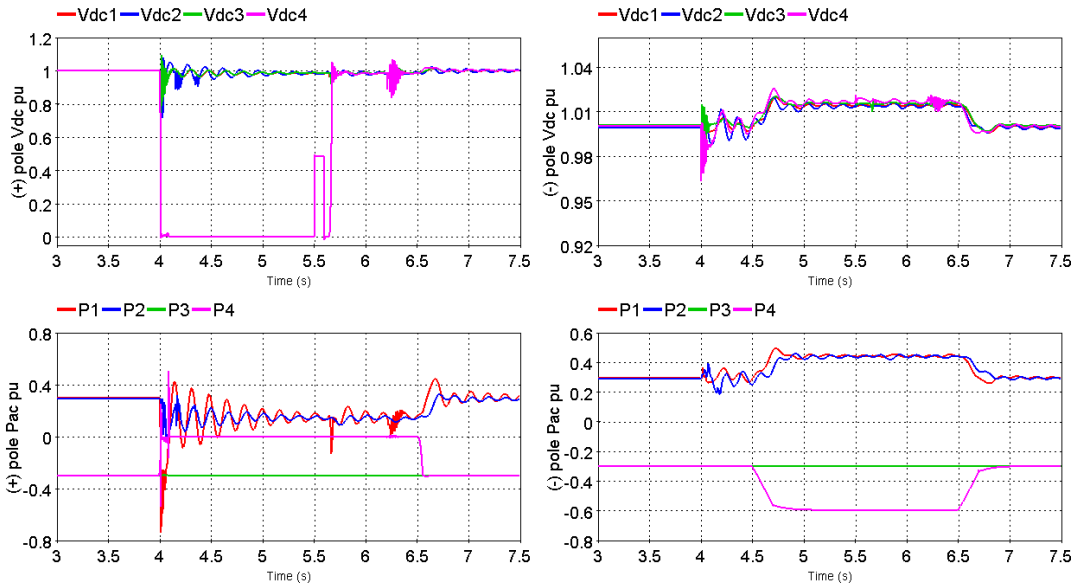


Figure 5.13: MTDC Vdc & Pac with 1 station in GFM and low damping

Increasing the damping term k_d from 150 to 500 significantly improves the MMC dynamic response by effectively damping the oscillations arising from the differing AC and DC dynamics (Figure 5.14). As a result, the system now clearly follows the C&P

sequence stages shown in Figure 5.8, exhibiting behaviour similar to the reference GFL control case. In this configuration, the GFM-controlled MMC propagates the disturbance to the connected AC system with well-damped oscillations, while the faster GFL control compensates for the slower dynamic response of the GFM controller, consistent with the studies presented in previous chapter.

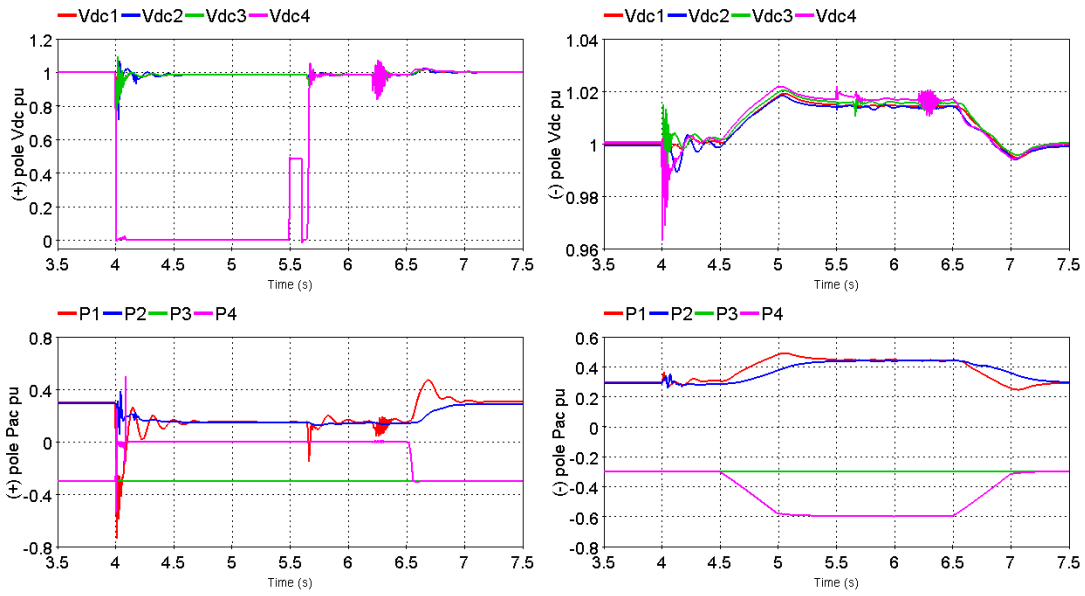


Figure 5.14: MTDC Vdc & Pac with 1 station in GFM and proper damping

5.4.3 GFM control in both stations S1 and S2

The system dynamics from the inclusion of GFM control under the proposed protection strategy have been analyzed. It is evident that, for the conventional hybrid system architecture, the GFM operation in Vdc–P droop mode exhibits an inherent tendency toward an oscillatory behavior. Moreover, as a fundamental DC system design requirement, adequate dynamic regulation of the DC voltage must be ensured, which constrains the permissible variation of the Vdc–P droop coefficient. Consequently, deploying GFM control at both stations will increase the level of interaction with the connected AC grids and further amplify oscillations. Furthermore, the absence of GFL control support for MTDC voltage regulation reduces the available degrees of freedom to balance the AC/DC power mismatch of the GFM converter. Therefore, system

modifications are required, either in control or hardware.

Control modifications are assessed by reducing the GFM inertial support and increasing the VSM damping. Figure 5.15 illustrates the configuration where both S_1 and S_2 operate in GFM mode with a very reduced inertia constant, i.e. $H = 0.25$ s. A sensitivity analysis is performed in the damping coefficient (k_d = 250, 500, 750). Results show that, despite the low inertia and increased damping, once the droop control is activated at the first station at 2 s, the mismatch between DC and AC power-flow dynamics continues producing undamped oscillations.

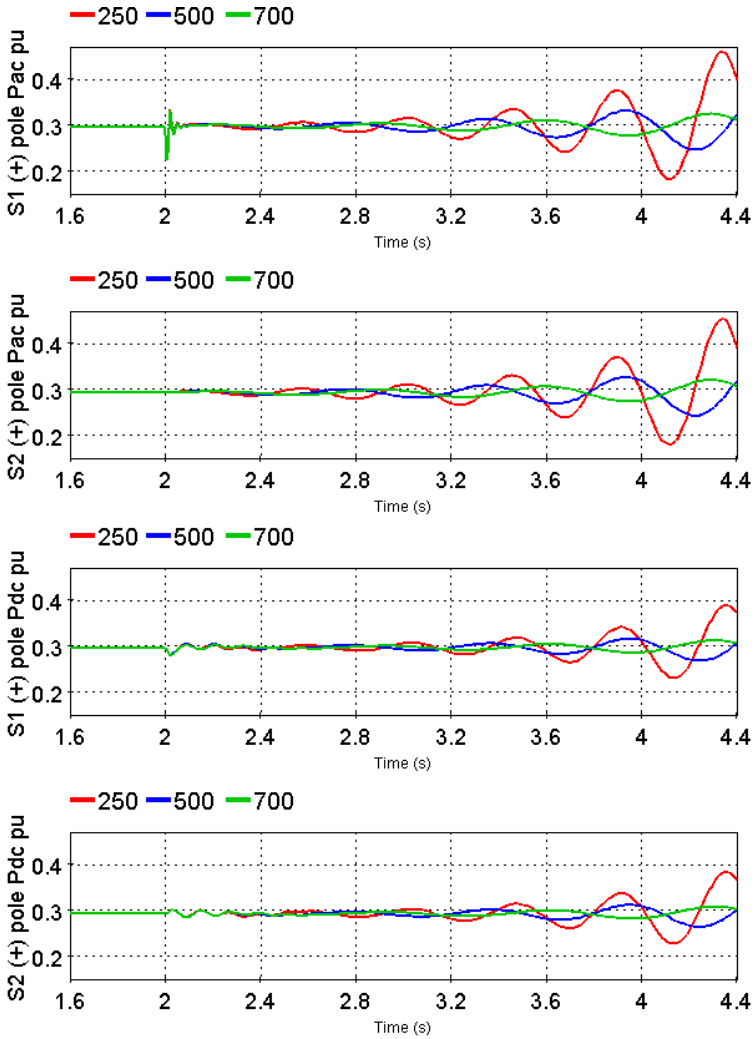


Figure 5.15: S_1 and S_2 (+) pole Pac & Pdc with both stations in GFM and different damping coefficients

After results have corroborated the previous analysis, it is now important to recall the system's operating principles and its remaining degrees of freedom. The MTDC voltage regulation is done by dedicated converter stations with Vdc-P droop as the outermost control layer. The Vdc-P droop reference is channelled to the AC and DC voltage modulation references. This control architecture, i.e., DC voltage regulation through AC and DC power flows, plus MMC internal energy control through DC power, is improved by means of the virtual capacitor principle [68], [81]. The simplified virtual capacitor used in this work uses the square of the DC voltage measurement at the MMC terminals as the MMC internal energy reference, as given in equation (2.3), where the internal energy control reference is limited as presented in [68]. Consequently, the MMC total energy storage is coupled to the MTDC voltage state, thereby creating an expanded energy reservoir.

This expanded storage enlarges the MTDC system's stability region, which is especially important given the large DC inductances that reduce the MTDC stability [86]. In addition, a fast energy control was necessitated by the MMC with GFM in Vdc-P droop control, due to a circuit design dictated by the partially selective protection strategy (passive elements DCRs and cables). A reduced rise time to tune the PI controller increases the speed with which the controller meets its command objective; in other words, the energy controller tightens the coupling between the MMC energy and the DC voltage, not allowing the control architecture to partially decouple the DC power flow from the energy control as done in Chapter 4.

On the AC loop, the VSM parameters can be adjusted. Nonetheless, reducing H would weaken the control's intended effect. Moreover, during transient events, the GFM response presents the dominant behavior throughout the hybrid system, as seen in the perturbation propagation in previous results and presented in [6]. It is seen, thus, that the AC and DC dynamics of the MMC are constrained by this control architecture, and a fundamental conflict: the controller must simultaneously serve the distinct power needs of both the AC and DC systems. At a system level, the lack of the GFL converter participating in the MTDC voltage regulation further restricts the available degrees of freedom.

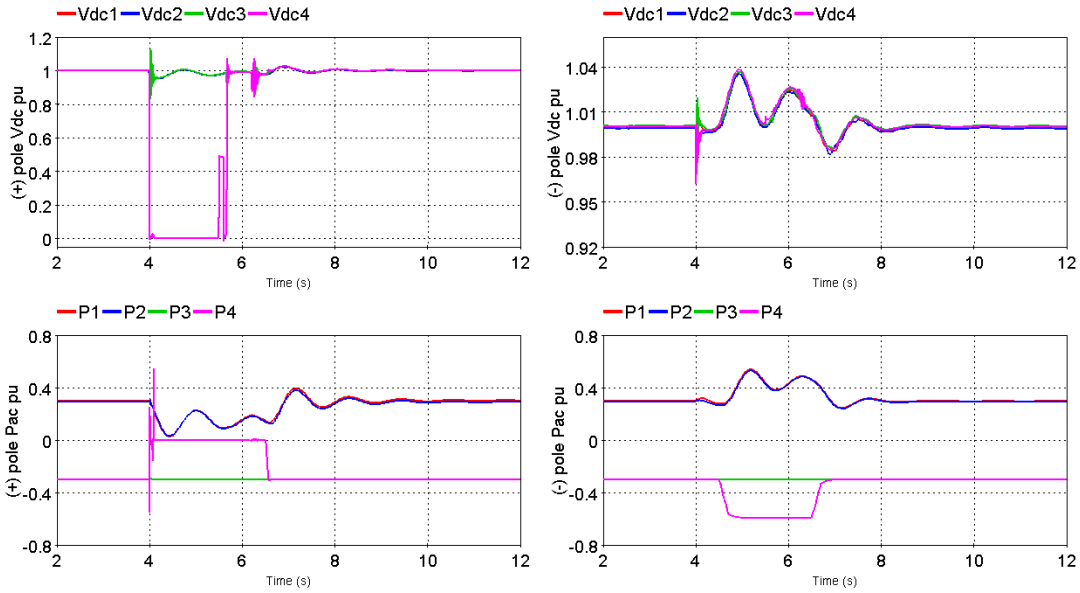


Figure 5.16: MTDC Vdc & Pac with 2 stations in GFM

Therefore, the preceding analyses and illustrative results indicate that the desired control functionalities have reached the limits for a conventional MMC architecture and the DC electrical circuit imposed by the partially selective protection strategy. Therefore, in order to decouple the AC and DC dynamics when using energy-based MMCs with GFM as the sole strategy regulating the MTDC voltage, another approach is needed, e.g., an extra energy storage system (ESS). In practice, this can be implemented by using a converter-interfaced supercapacitor or battery, together with a higher-level system energy management control [142]. Due to space and time constraints, the AC and DC dynamics decoupling is presented in a simplified manner, serving only as a proof of concept. This is done by increasing the converter electrostatic constant, or its capacitance by ten times from previous cases. The VSM parametrization is kept as in the previous subsection, i.e., $H = 1.5$ s and a damping coefficient of $k_d = 500$.

Figure 5.16 shows the MTDC system performance along the DC FRT operation with the proposed concept and using GFM as the sole strategy regulating the MTDC voltage.

The increased size of the system energy storage enables partial decoupling of the AC and DC dynamics, thereby allowing stable operation of the system throughout

each stage of the C&P sequence presented in Figure 5.8. The perturbation is further propagated in the hybrid system, resulting in more pronounced oscillations compared with the case where GFM is applied at only one station. Therefore, the proper tuning of the VSM should be performed, as the oscillations may lead to further interactions with the interconnected AC systems, which so far have been considered as ideal strong systems.

5.5 Summary

In this chapter, a comprehensive methodology for implementing a functional, partially selective protection strategy in an MTDC grid was presented and evaluated. The core criteria for system partitioning were reviewed and utilized as foundational guidelines to establish the proposed DC grid segmentation. Furthermore, the interplay between key protection parameters was analyzed, providing a theoretical basis for the results obtained during the sizing of DCRs. Finally, this relationship was used to highlight the inherent trade-offs involved in DCR sizing, specifically focusing on the control and operational challenges it can impose on MTDC grid stability.

The role of the various circuit breakers and their operational coordination with grid control actions were emphasized, illustrating the spatial propagation of perturbations throughout the hybrid MTDC system and its interconnected AC networks. Furthermore, the dynamic performance of the hybrid system during DC FRT under a partially selective protection strategy was thoroughly analyzed. This assessment was initially performed using a standard GFL control strategy as a benchmark, followed by an evaluation of the system's response during the gradual integration of GFM strategy.

The GFM strategy exhibited significant challenges in accomodating both AC and DC power flows under the new DC system dynamics imposed by the relatively large DCRs. Because the energy controller tuning demanded a wider bandwidth, the system's available degrees of freedom were further constrained. This restriction effectively left the Vdc-P droop and VSM settings as the sole remaining parameters for tuning the power converter control. A detailed investigation into the control interaction mechanisms—previously established in earlier chapters—revealed a strong coupling between

the MMC's AC and DC dynamics. This cross-domain coupling with differing dynamics explains the highly oscillatory behavior observed in GFM-controlled units under these specific DC circuit characteristics. Notably, and mirroring the phenomena documented previously, the GFL-controlled converter acted as a stabilizing agent, actively contributing to the damping of GFM-originated oscillations within the MTDC grid.

Relying exclusively on the GFM strategy to regulate the DC voltage exposed the fundamental limitations of both the existing coordinated control functionalities and conventional DC system architectures under these severe constraints. To address these limitations, a partial decoupling of the AC and DC dynamics was proposed as a fundamental architectural solution. The successful proof-of-concept presented in this chapter demonstrates that mitigating these cross-domain interactions is crucial for unlocking the full potential of GFM control in highly restricted multi-terminal topologies, thereby establishing a path forward for resilient hybrid grid operations.

Chapter 6

Concluding remarks and perspective

Successful development and integration of MTDC systems into existing AC power grids necessitate strict adherence to fundamental operational constraints, most notably, stable steady-state operation and robust DC FRT capabilities.

The development of methodologies appeared essential to perform the proposed studies. Under the different proposed frameworks, studies appeared consistent having a clear structure for the development of models, phenomena understanding and conclusions drawing. Every study confirmed the need for a sequential review and analysis of phenomena. Beyond the probability of using a particular protection strategy, the study of different large disturbances allowed a comprehensive overview of the system natural behavior and responses. This comprehensive review allowed for a more complete understanding of the different C&P philosophies, MTDC system operating principles, modeling requirements, software reckoning, and project development.

6.1 Conclusions

By systematically analyzing system conditions and the available operational degrees of freedom, this thesis clarifies the complex interactions and interdependencies inherent in hybrid AC/DC power systems, specifically where distinct AC networks are inter-

connected via multipurpose MTDC grids. These insights establish a robust theoretical foundation for the proposed C&P strategies, ultimately ensuring reliable DC FRT performance across a wide spectrum of operational constraints. Furthermore, the framework developed herein provides grid operators and system designers with a scalable approach to mitigate cross-domain vulnerabilities, bridging the gap between required protection schemes and MTDC system control coordination for future hybrid systems' R&R and stability concerns.

To seamlessly integrate and evaluate the proposed control functionalities within MTDC systems, two distinct research methodologies were developed and systematically executed (see Figure 2.17 and Figure 4.2). In alignment with standard power system modelling practices, the complexity of the simulation environment was increased progressively. This staged approach allows for a clearer isolation and characterization of specific transient and steady-state phenomena. Consequently, the interconnected onshore and offshore AC systems were modeled using equivalent, simplified representations; this approach reduced computational effort and eliminated peripheral grid dynamics, thereby keeping the analytical focus primarily on the core MTDC system dynamics.

Building upon the system-level analysis, open-loop C&P sequences were further developed (Chapter 3 and Chapter 4) or fully designed (Chapter 5) to maintain MTDC system integrity during DC fault scenarios. These operational sequences were systematically evaluated under both non-selective and partially selective protection philosophies, considering various technological devices and AC grid conditions. This comprehensive analysis demonstrated the extent of perturbation propagation throughout the hybrid AC/DC system. Furthermore, GFL control was utilized as a benchmark to investigate the performance of the hybrid system, against which GFM control was analyzed as a viable alternative for simultaneous AC and DC services, aiming to increase the overall hybrid system R&R.

The weak AC grid condition was analyzed as a critical scenario for hybrid system DC FRT performance. Obtained results confirmed the inherent challenges associated with reduced voltage stiffness and facilitated the precise identification of detrimental control

interactions. As part of the restoration process within the DC FRT process, the re-energization of the MTDC grid exhibited a better controlled performance when utilizing a single converter with a Vdc-master control, in comparison with the distributed use of Vdc-P droop control. Furthermore, to mitigate the different issues identified, the decoupling of control interactions was proposed as a feasible solution, highlighting the necessity for tailored, sequenced control strategies.

Under a non-selective protection philosophy, a thorough analysis of the GFM strategy was conducted, specifically examining its AC response to large disturbances and DC-side interactions during MTDC voltage regulation. The healthy converter's internal energy depletion will correspond to the given AC inertial support. Thus, the desired inertial support will require proper sizing of MMC internal energy storage, namely, its submodule capacitors. Coordinating GFM and GFL controls to regulate grid voltage revealed a specific control-interaction mechanism, as well as limitations in delivering simultaneous AC and DC services. The slow AC dynamics of the VSM reduce the MMC's power sensitivity to DC voltage variations, allowing the faster GFL control to supply the requested power by the MTDC grid. Based on this system behavior, the extended use of GFM as the primary strategy was enabled by partially decoupling the interaction mechanism through MMC control degrees of freedom, namely, by slowing down the response time of the internal energy controller. Satisfactory results of the system DC FRT were obtained for two distinct decoupling strategies, thus validating the performed analysis. Nevertheless, the inherent limitations of such control coordination were underscored.

Under a partially selective philosophy, a methodology for developing a grid protection strategy was introduced. The interdependency among key protection parameters was highlighted, and an alternative development approach under this same philosophy was presented. Restricting the use of HV DCCBs throughout the DC grid highlighted the need for lower-rating DCCBs in the MR conducting path and ACCBs on the offshore side. Furthermore, utilizing different types of CBs underscored the need for proper coordination in the open-loop DC FRT C&P sequence. Under the GFL strategy, the MTDC grid DC FRT sequence presented fewer challenges beyond those

already highlighted. Conversely, similar to the non-selective protection strategy, emergent constraints posed significant challenges for GFM-based power electronics control while simultaneously reducing the available degrees of freedom compared to the non-selective case. To address this issue, the response time of the MMC internal energy controller was tuned to the order of tens of milliseconds, allowing the MTDC system to start normal operation within stability margins. For MTDC grid control coordination — where the GFM strategy acts as the sole mechanism regulating DC voltage —a rigorous analysis of the operating principles revealed the hybrid system's limitations in decoupling the identified control interaction mechanism. Consequently, a fundamental solution was proposed: integrating increased energy storage. While presented as a proof of concept, this solution establishes a foundation for future location and optimization of the additional ESS.

Overall, the research objectives have been fulfilled, providing scientific contributions originally envisioned for this work. The findings offer a robust framework for understanding and mitigating the complexities of MTDC system integration when facing large disturbances, in particular pole-to-pole DC faults.

As a corollary contribution, this thesis used an established theoretical framework - namely, system modelling with block diagrams - to derive the characteristic equation of the generic VSM control, providing a solid reference for future studies.

6.2 Future work

While the fundamental aspects of DC FRT have been thoroughly examined throughout this research, certain dimensions were either omitted or addressed superficially. For instance, the modelling of the various AC grids was simplified, as noted in the introductory and concluding remarks. On the onshore side, the AC system lacked dynamic elements; this limitation precluded the identification of potential control interactions and AC-side phenomena, such as interarea oscillations between synchronous generator and GFM converters. Regarding the offshore side, the detailed behavior of OWFs was not fully modelled, providing only high-level guidelines of expected performance. Furthermore, the optimal sizing, and strategic placement of energy storage systems warrant

more rigorous analysis. As well, different embedment levels of the MTDC system with a bulk AC system could be analyzed, as done in other efforts within the HVDC-wise project. These areas represent important paths for future research.

Appendix A

Appendix A: VSM characteristic equation derivation

Given the lack of documented references regarding the characteristic equation for the GFM control approach used in this study, i.e., the VSM approach, this appendix is dedicated to deriving equation (2.9) based on the block diagram in Figure 2.9.

The block diagram in Figure 2.9 can be used to obtain the relationship between input and output of the GFM control, by means of the control transfer functions [143]. Thus, the model of the linear system can be described in a generic manner as (A.1).

$$P_{ac} = G_1(s)\ \tilde{\omega}_g\ +\ G_2(s)\ P^*_{ac} \tag{A.1}$$

Block-diagram algebra can be used to manipulate the block diagram and derive the required equation. Furthermore, as it is a linear system and the block diagram presents two input signals which follow equivalent paths through the linearized system, the control's characteristic equation can be obtained by setting one of the two inputs equal to zero, and the resulting transfer function should be equal in both cases.

A.0.1 Setting P^*_{ac} equal to zero

By setting to zero P^*_{ac} on the VSM block diagram in Figure 2.9, the block diagram in Figure A.1 is obtained.

Appendix A. Appendix A: VSM characteristic equation derivation

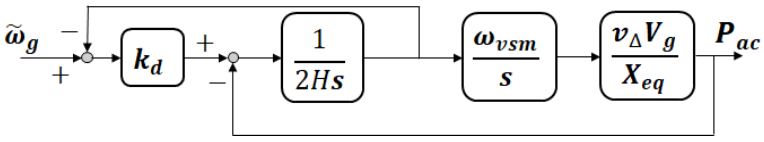


Figure A.1: P^*_{ac} set to zero - Step 1

Shifting the damping coefficient k_d before the difference between the estimated frequency by the PLL, $\tilde{\omega}_g$, and the VSM calculated frequency, ω_{vsm} the block diagram in Figure A.2 is obtained.

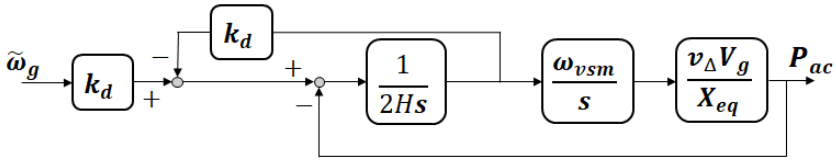


Figure A.2: P^*_{ac} set to zero - Step 2

Doing a change of variable for convenience as given in (A.2).

$$Q = \frac{\omega_{vsm0}}{s}\frac{v_\Delta V_g}{X_{eq}} \tag{A.2}$$

Substituting (A.2) in the block diagram of Figure A.2, block diagram of Figure A.3 is obtained.

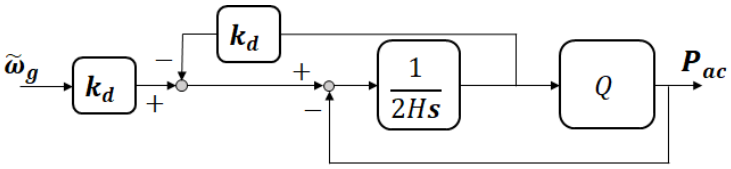


Figure A.3: P^*_{ac} set to zero - Step 3

Shifting Q back before the feedback loop of the damping term implies the division by Q in the same loop, resulting in the block diagram of Figure A.4.

Appendix A. Appendix A: VSM characteristic equation derivation

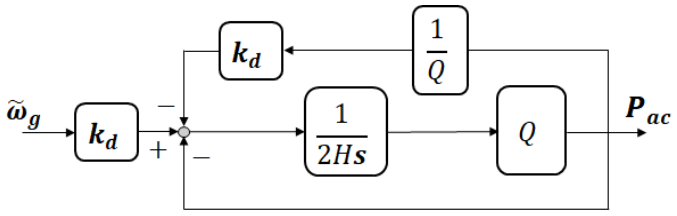


Figure A.4: P_{ac}^* set to zero - Step 4

Now both the damping loop and the power output, P_{ac}, feedback loops can be added, resulting on the block diagram of Figure A.5.

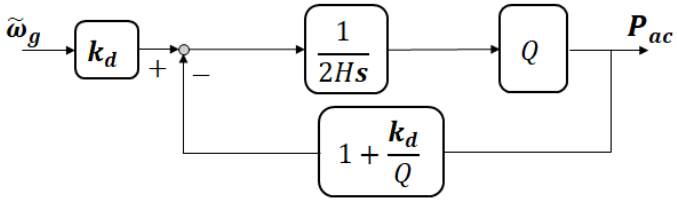


Figure A.5: P_{ac}^* set to zero - Step 5

Obtaining the closed-loop transfer function of the block diagram in Figure A.5 results in (A.3).

$$\frac{P_{ac}}{\tilde{\omega}_g} = \frac{k_d \frac{1}{2H\ s}\ Q}{1 + \frac{Q}{2H\ s}\ (1 + \frac{k_d}{Q})} \tag{A.3}$$

Manipulating the characteristic equation of (A.3) results in (A.4).

$$2H\ s\ +\ Q\ +\ k_d = 0 \tag{A.4}$$

Substituting (A.2) in (A.4) results in A.5.

$$2H\ s\ +\ \frac{\omega_{vsm0}}{s}\frac{v_\Delta V_g}{X_{eq}}\ +\ k_d = 0 \tag{A.5}$$

Doing further algebraic manipulation in (A.5) results in the VSM characteristic equation (A.6), which is used in this research effort.

$$s^2\ +\frac{k_d}{2H}\ s + \frac{v_\Delta V_g\ \omega_{vsm0}}{2H\ X_{eq}} = 0 \tag{A.6}$$

A.0.2 Setting $\tilde{\omega}_g$ equal to zero

The same principles as in previous subsection are used in this subsection. Accordingly, the change of variable (A.2) is used in the block diagram of Figure 2.9.

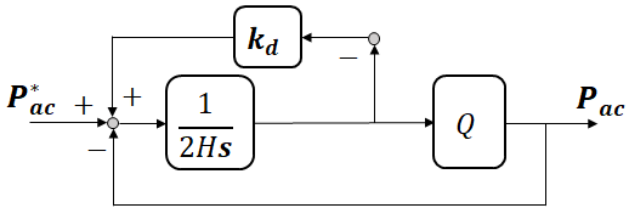


Figure A.6: $\tilde{\omega}_g$ set to zero - Step 1

Separating the first node in the block diagram of Figure A.6 for convenience, the block diagram in Figure A.7 is obtained.

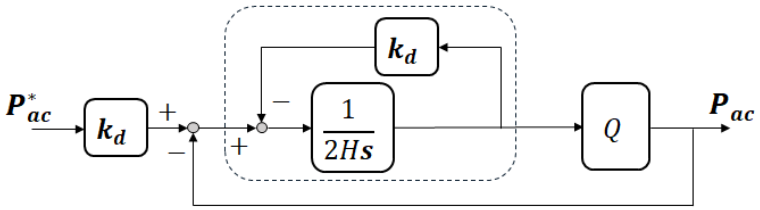


Figure A.7: $\tilde{\omega}_g$ set to zero - Step 2

For convenience, the blocks within the dashed perimeter are isolated and presented in the block diagram of Figure A.8.

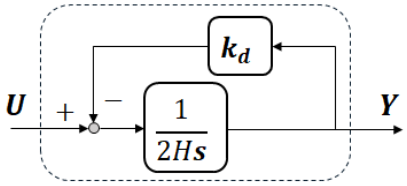


Figure A.8: $\tilde{\omega}_g$ set to zero - Step 2.1

The open-loop transfer function of the block diagram in Figure A.8 is now derived. Its open-loop output is given by (A.7).

Appendix A. Appendix A: VSM characteristic equation derivation

$$Y = \frac{1}{2H\ s}(U\ -\ k_d\ Y) \tag{A.7}$$

Solving for U (A.8) is obtained.

$$Y\ (1 + k_d) = U \tag{A.8}$$

Dividing the open-loop control output by the input signal the open-loop transfer function (A.9) is obtained.

$$\frac{Y}{U} = \frac{1}{2H\ s\ +\ k_d} \tag{A.9}$$

Substituting the obtained open-loop transfer function (A.9) of the excerpted block diagram in Figure A.7.

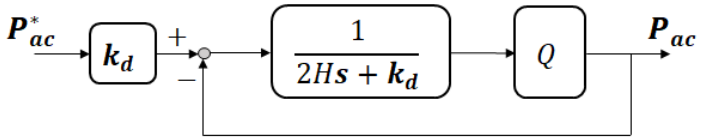


Figure A.9: $\tilde{\omega}_g$ set to zero - Step 3

Obtaining the closed-loop transfer function of block diagram in Figure A.9.

$$\frac{P_{ac}}{P^*_{ac}} = \frac{k_d\ \frac{Q}{2H\ s\ +\ k_d}}{1 + \frac{Q}{2H\ s\ +\ k_d}} \tag{A.10}$$

Manipulating the characteristic equation of A.10.

$$2H\ s\ +\ k_d\ +\ Q = 0 \tag{A.11}$$

Substituting (A.2) in (A.11).

$$2H\ s\ +\ k_d\ +\ \frac{\omega_{vsm0}}{s}\frac{v_\Delta V_g}{2H\ X_{eq}} = 0 \tag{A.12}$$

By doing further algebraic manipulation of (A.12), (A.13) is obtained.

$$s^2 + \frac{k_d}{2H}\, s + \frac{v_\Delta V_g\, \omega_{vsm0}}{2H\, X_{eq}} = 0 \tag{A.13}$$

Q.E.D.

As expected, given the linearity of the modelled system, the obtained characteristic equation when setting the input signal $\tilde{\omega}_g$ to zero is equal to the one obtained in previous subsection (A.6), when setting P^*_{ac} to zero.

Appendix A. Appendix A: VSM characteristic equation derivation

References

[1] M. Panteli and P. Mancarella, "Influence of extreme weather and climate change on the resilience of power systems: Impacts and possible mitigation strategies," *Electric Power Systems Research*, vol. 127, pp. 259–270, 2015.

[2] I. E. A. (IEA). "The middle east and global energy markets. "[Online]. Available: https://www.iea.org/topics/the-middle-east-and-global-energy-markets. (accessed: 28.03.2026).

[3] I. E. A. (IEA). "Climate change. "[Online]. Available: https://www.iea.org/topics/climate-change. (accessed: 28.03.2026).

[4] Eliagroup. "Elia group eu. "[Online]. Available: https://www.eliagroup.eu/#. (accessed: 28.03.2026).

[5] Tennet. "Tennet. "[Online]. Available: https://www.tennet.eu/energy-transition. (accessed: 28.03.2026).

[6] Rte. "France's network development plan (sddr). "[Online]. Available: https://www.rte-france.com/en/data-publications/strategic-plans/ten-year-network-development-plan#Leschema2025. (accessed: 28.03.2026).

[7] N. Grid. "Enable the ongoing transition to the energy system. "[Online]. Available: https://www.nationalgrid.com/electricity-transmission/who-we-are/riio-t2-performance/enable-ongoing-transition. (accessed: 28.03.2026).

[8] CFE. "Con la cfe, avanza la transición energética en méxico. "[Online]. Available: https://app.cfe.mx/cdn/2019/Imagenes/Boletines/Publicaciones/Suple_CFE-26feb24Final.pdf. (accessed: 28.03.2026).

[9] I. R. E. A. (IRENA). "The energy transition in africa. "[Online]. Available: https://www.irena.org/Publications/2024/Apr/The-energy-transition-in-Africa-Opportunities-for-international-collaboration-with-a-focus-on-the-G7. (accessed: 28.03.2026).

[10] I. R. E. A. (IRENA). "China's renewable energy boom has its own challenges. here's what we can learn. "[Online]. Available: https://www.weforum.org/stories/2025/12/china-adding-more-renewables-to-grid/. (accessed: 28.03.2026).

[11] E. PARLIAMENT and T. C. O. T. E. UNION. "European climate law. "[Online]. Available: https://eur-lex.europa.eu/legal-content/EN/TXT/?uri=CELEX:32021R1119. (accessed: 05.04.2026).

[12] E. Comission. "The european green deal. "[Online]. Available: https://commission.europa.eu/strategy-and-policy/priorities-2019-2024/european-green-deal_en. (accessed: 05.04.2026).

[13] C. C. C. (CCC). "The sixth carbon budget electricity generation. "[Online]. Available: https://www.theccc.org.uk/wp-content/uploads/2020/12/Sector-summary-Electricity-generation.pdf. (accessed: 05.04.2026).

[14] Tennet. "The 2gw program. "[Online]. Available: https://www.tennet.eu/2gw-program. (accessed: 28.03.2026).

[15] S. Energy. "High-voltage direct current hvdc plus®. our cutting-edge hvdc solution based on mmc technology. "[Online]. Available: https://www.siemens-energy.com/global/en/home/products-services/product-offerings/high-voltage-direct-current-transmission-solutions.html. (accessed: 06.04.2026).

[16] C. France, "Impacts of energy transition on the power system. ensuring grid stability in the era of renewable integration - the italian energy transition: Priorities and challenges for the power system," *Conférence du Comité National Français - La transition Energétique - INSA Lyon*, 2025.

[17] R. A. Bjarne and L. N. Stig, "High voltage dc transmission systems," 2025.

[18] B. Badrzadeh and Z. Emin, "Power system dynamic modelling and analysis in evolving networks," 2024.

[19] Epexspot. "Power market. "[Online]. Available: https://www.epexspot.com/en/basicspowermarket. (accessed: 28.03.2026).

[20] H. Ergun, "Grid planning for the future grid: Optimizing topology and technology considering spatial and temporal effects," *Leuven: Doctoral Disertation, KU Leuven*, 2015.

[21] HVDC-wise. "Hvdc-wise project. "[Online]. Available: https://hvdc-wise.eu/. (accessed: 28.03.2026).

[22] H. wise. "Project description. "[Online]. Available: https://hvdc-wise.eu/project-description/. (accessed: 06.04.2026).

[23] T. CIGRE, "881; electromagnetic transient simulation models for large-scale system impact studies in power systems having a high penetration of inverter-connected generation," *WG C4*, vol. 56, 2022.

[24] G. Chaspierre. "Ensuring eu power system stability: Why updated national connection requirements are essential. "[Online]. Available: https://gilleschaspiere.substack.com/p/ensuring-eu-power-system-stability. (accessed: 06.04.2026).

[25] E. E. "28 april 2025 blackout. "[Online]. Available: https://www.entsoe.eu/publications/blackout/28-april-2025-iberian-blackout/. (accessed: 06.04.2026).

[26] HVDC-wise, "Deliverable 2.1 appendix 3 survey of existing and planned dc grids," *Deliverable 2.1*, 2023.

[27] A. Europe, "Hvdc quo vadis," *Webinar slides*, 2026.

[28] A. Bangar, N. Belda, A. Kumar, and et.al., "±525 kv 2 gw bipole vsc-hvdc offshore transmission (tennet projects) - key design aspects," in *CIGRE, 10523, B4 DC SYSTEMS POWER ELECTRONICS, PS1 DC Equipment and Systems, Paris session*, 2024.

[29] S. D. Tavakoli, M. G. Dozein, V. A. Lacerda, M. C. Mañe, E. Prieto-Araujo, P. Mancarella, and O. Gomis-Bellmunt, "Grid-forming services from hydrogen electrolyzers," *IEEE transactions on sustainable energy*, vol. 14, no. 4, pp. 2205–2219, 2023.

[30] C. H. Appel A. Dähling C., "Grid-serving integration of electrolizers," *VDE Discussion Paper*, vol. 1, pp. 1–8, 2022.

[31] G. Chaspiere, "Evolution of the load and impact on power systems stability," *GridStab News*, vol. 1, 2025.

[32] G. Chaspiere, "Real-case examples of battery energy storage systems in grid forming mode," *GridStab News*, vol. 1, 2025.

[33] T. CIGRE, "739; protection and local control of hvdc-grids," *Joined WG B4/B5.59*, 2018.

[34] M. Wang, "Multi-vendor protection systems for meshed hvdc grids," *Leuven: Doctoral Disertation, KU Leuven*, 2020.

[35] HVDC-wise, "Identification of (suitable) ac/dc grid architectures," *Deliverable 3.3*, 2024.

[36] M. Brignone, D. Mestriner, P. Molfino, M. Nervi, M. Marzinotto, and S. Patti, "The mitigation of interference on underground power lines caused by the hvdc electrode," *Energies*, vol. 16, no. 23, p. 7769, 2023.

[37] H. Rosenberg, "Electric power hvdc from land to off-shore structures utilizing sea-electrodes for return current concerns and precautions with regard to environment and corrosion," in *Proceedings of the International Gas Union Research Conference, Copenhagen, Denmark*, 2014, pp. 17–19.

[38] R. Walling, M. Sublich, D. Lorden, and S. Doe, "Simultaneous pole and neutral faults on an hvdc line with a dedicated metallic return," *IEEE transactions on power delivery*, vol. 5, no. 2, pp. 1129–1136, 1990.

[39] T. CIGRE, "531; cable systems electrical characteristics," *WG B1.30*, 2013.

[40] G. Chen, M. Hao, Z. Xu, A. Vaughan, J. Cao, and H. Wang, "Review of high voltage direct current cables," *CSEE Journal of Power and Energy Systems*, vol. 1, no. 2, pp. 9–21, 2015.

[41] G. Mazzanti, "High voltage direct current transmission cables to help decarbonisation in europe: Recent achievements and issues," *High Voltage*, vol. 7, no. 4, pp. 633–644, 2022.

[42] A. Stan, S. Costinaș, and G. Ion, "Overview and assessment of hvdc current applications and future trends," *Energies*, vol. 15, no. 3, p. 1193, 2022.

[43] T. CIGRE, "533; hvdc grid feasibility study," *WG B4.52*, 2013.

[44] M. Goertz, S. Wenig, S. Beckler, C. Hirsching, M. Suriyah, and T. Leibfried, "Analysis of cable overvoltages in symmetrical monopolar and rigid bipolar hvdc configuration," *IEEE transactions on power delivery*, vol. 35, no. 4, pp. 2097–2107, 2019.

[45] T. CIGRE, "610; offshore generation cable connections," *WG B1.40*, 2015.

[46] J. Castellanos, "Assessment of a double-ended traveling-wave differential algorithm for cable linked vsc hvdc systems," *Master's Thesis. Leuven: Faculty of Engineering Science, KU Leuven*, 2023.

[47] Ø. Sagosen, A. Craig, R. Poole, and R. Paradine, "Need, design and business case for building the north sea link," in *Proc. CIGRE gen. meeting*, 2018, pp. 1–9.

[48] S. Rahman, I. Khan, H. I. Alkhammash, and M. F. Nadeem, "A comparison review on transmission mode for onshore integration of offshore wind farms: Hvdc or hvac," *Electronics*, vol. 10, no. 12, p. 1489, 2021.

[49] R. Electrica, "Blackout in spanish peninsular electrical system the 28th of april 2025," vol. 1, pp. 1–15, 2025.

[50] A. Gasparella, D. Koolen, A. Zucker, et al., "The merit order and price-setting dynamics in european electricity markets," 2023.

[51] N. A. E. R. Corporation, "Characteristics and risks of emerging large loads," *Large Loads Task Force White Paper*, vol. 1, pp. 1–50, 2025.

[52] G. Chaspiere, "Gridstab news: Regular posts to demystify power system dynamics and stability," *GridStab News*, vol. 1, 2024.

[53] P. Kundur, "Power system stability," *Power system stability and control*, vol. 10, no. 1, pp. 7–1, 2007.

[54] X. He and H. Geng, "Synchronization stability analysis and enhancement of grid-tied multi-converter systems," in *2020 IEEE Industry Applications Society Annual Meeting*, IEEE, 2020, pp. 1–8.

[55] X. Wang, M. G. Taul, H. Wu, Y. Liao, F. Blaabjerg, and L. Harnefors, "Grid-synchronization stability of converter-based resources—an overview," *IEEE Open Journal of Industry Applications*, vol. 1, pp. 115–134, 2020.

[56] B. Hu, C. Zhao, S. Sahoo, C. Wu, L. Chen, H. Nian, and F. Blaabjerg, "Synchronization stability enhancement of grid-following converter under inductive power grid," *IEEE Transactions on Energy Conversion*, vol. 38, no. 2, pp. 1485–1488, 2023.

[57] X. Li, C. Zhang, L. Zhu, Z. Wang, and L. Guo, "A pll-equivalent model for low-frequency stability analysis of voltage source converter connected to weak grid," *IET Energy Systems Integration*, vol. 5, no. 2, pp. 180–191, 2023.

[58] T. Qoria, "Grid-forming control to achieve a 100% power electronics interfaced power transmission systems," *ÉCOLE DOCTORALE SCIENCES ET MÉTIERS DE L'INGENIEUR, L2EP - Campus Lille*, 2020.

[59] B. Li, Q. Li, Y. Wang, W. Wen, B. Li, and L. Xu, "A novel method to determine droop coefficients of dc voltage control for vsc-mtdc system," *IEEE Transactions on Power Delivery*, vol. 35, no. 5, pp. 2196–2211, 2020.

[60] J. Beerten, D. Van Hertem, and R. Belmans, "Vsc mtdc systems with a distributed dc voltage control-a power flow approach," in *2011 IEEE Trondheim PowerTech*, IEEE, 2011, pp. 1–6.

[61] S. Samimi, F. Gruson, P. Delarue, and X. Guillaud, "Synthesis of different types of energy based controllers for a modular multilevel converter integrated in an hvdc link," in *11th IET International Conference on AC and DC Power Transmission*, IET, 2015, pp. 1–7.

[62] E. Sánchez-Sánchez, E. Prieto-Araujo, and O. Gomis-Bellmunt, "The role of the internal energy in mmcs operating in grid-forming mode," *IEEE Journal of Emerging and Selected Topics in Power Electronics*, vol. 8, no. 2, pp. 949–962, 2019.

[63] M. A. Perez, S. Ceballos, G. Konstantinou, J. Pou, and R. P. Aguilera, "Modular multilevel converters: Recent achievements and challenges," *IEEE Open Journal of the Industrial Electronics Society*, vol. 2, pp. 224–239, 2021. DOI: 10.1109/OJIES.2021.3060791.

[64] S. energy. "Hvdc plus. "[Online]. Available: https://www.siemens-energy.com/us/en/home/products-services/product/hvdc-plus.html#Modular-Multilevel-Converter-(MMC)-tab-0. (accessed: 20.08.2025).

[65] N. Mohan, T. M. Undeland, and W. P. Robbins, *Power electronics: converters, applications, and design*. John wiley & sons, 2003.

[66] S. Debnath, J. Qin, B. Bahrani, M. Saeedifard, and P. Barbosa, "Operation, control, and applications of the modular multilevel converter: A review," *IEEE transactions on power electronics*, vol. 30, no. 1, pp. 37–53, 2014.

[67] K. Sharifabadi, L. Harnefors, H.-P. Nee, S. Norrga, and R. Teodorescu, *Design, control, and application of modular multilevel converters for HVDC transmission systems*. John Wiley & Sons, 2016.

[68] K. Shinoda, A. Benchaib, and J. Dai, "A new energy management control of modular multilevel converters for coping with voltage stress on sub-modules," in *CIGRE-IEC 2019 Conference on EHV and UHV (AC DC)*, CIGRE-IEC, 2019, Hakodate, Hokkaido.

[69] Q. Tu, Z. Xu, and L. Xu, "Reduced switching-frequency modulation and circulating current suppression for modular multilevel converters," *IEEE transactions on power delivery*, vol. 26, no. 3, pp. 2009–2017, 2011.

[70] H. Saad, X. Guillaud, J. Mahseredjian, S. Dennetiere, and S. Nguefeu, "Mmc capacitor voltage decoupling and balancing controls," *IEEE Transactions on Power Delivery*, vol. 30, no. 2, pp. 704–712, 2014.

[71] J. M. H. Saad and D. S., "Vsc-mmc station models. modular multilevel converter," *EMTP-VR*, 2014.

[72] Y. Gim, Z. Li, J. Meng, Z. Deng, and Q. Song, "Analysis of submodule capacitor overvoltage during dc-side fault in hybrid mmc-based hvdc system," in *2019 10th International Conference on Power Electronics and ECCE Asia (ICPE 2019-ECCE Asia)*, IEEE, 2019, pp. 2794–2799.

[73] B. Andersen, L. Xu, P. Horton, and P. Cartwright, "Topologies for vsc transmission," *Power Engineer*, vol. 16, no. 3, pp. 142–150, 2002.

[74] P. Blaszczyk, K. Koska, and P. Klimczak, "Energy balancing in modular multilevel converter systems," *Bulletin of the Polish Academy of Sciences: Technical Sciences*, no. 5, 2017.

[75] E. Sánchez-Sánchez, E. Prieto-Araujo, A. Junyent-Ferré, and O. Gomis-Bellmunt, "Analysis of mmc energy-based control structures for vsc-hvdc links," *IEEE journal of emerging and selected topics in power electronics*, vol. 6, no. 3, pp. 1065–1076, 2018.

[76] H. Bekkouri, A. Benchaib, F. Morel, P. Rault, J.-C. Gonzalez-Torres, and F. Errigo, "Energy-based and non-energy-based control strategies for modular multilevel converters with embedded energy storage," in *2023 25th European Conference on Power Electronics and Applications (EPE'23 ECCE Europe)*, IEEE, 2023, pp. 1–10.

[77] R. Marquardt, "A new modular voltage source inverter topology," in *Conf. Rec. EPE 2003*, 2003.

[78] Q. Tu, Z. Xu, and J. Zhang, "Circulating current suppressing controller in modular multilevel converter," in *IECON 2010-36th Annual Conference on IEEE Industrial Electronics Society*, IEEE, 2010, pp. 3198–3202.

[79] G. Bergna, J. A. Suul, and S. D'Arco, "State-space modelling of modular multilevel converters for constant variables in steady-state," in *2016 IEEE 17th Workshop on Control and Modeling for Power Electronics (COMPEL)*, IEEE, 2016, pp. 1–9.

[80] E. S. Sánchez, "Energy-based control schemes of modular multilevel converters for hvdc applications," Ph.D. dissertation, Universitat Politècnica de Catalunya, 2020.

[81] K. Shinoda, A. Benchaib, J. Dai, and X. Guillaud, "Virtual capacitor control for stability improvement of hvdc system comprising dc reactors," in *15th IET International Conference on AC and DC Power Transmission (ACDC 2019)*, IET, 2019.

[82] H. Saad, X. Guillaud, J. Mahseredjian, S. Dennetiere, and S. Nguefeu, "Mmc capacitor voltage decoupling and balancing controls," *IEEE Transactions on Power Delivery*, vol. 30, no. 2, pp. 704–712, 2014.

[83] K. Shinoda, A. Benchaib, J. Dai, and X. Guillaud, "Virtual capacitor control: Mitigation of dc voltage fluctuations in mmc-based hvdc systems," *IEEE Transactions on Power Delivery*, vol. 33, no. 1, pp. 455–465, 2017.

[84] S. Golestan, J. M. Guerrero, and J. C. Vasquez, "Three-phase plls: A review of recent advances," *IEEE Transactions on Power Electronics*, vol. 32, no. 3, pp. 1894–1907, 2016.

[85] T. Qoria, "Grid-forming control to achieve a 100% power electronics interfaced power," *HESAM Université*, 2020.

[86] K. Shinoda, "Control and energy management of mmc-based multi-terminal hvdc grids," Ph.D. dissertation, Ecole Centrale de Lille, 2017.

[87] S. Akkari, "Control of a multi-terminal hvdc (mtdc) system and study of the interactions between the mtdc and the ac grids.," Ph.D. dissertation, Universite Paris Saclay (COmUE), 2016.

[88] T. Qoria, E. Rokrok, A. Bruyere, B. François, and X. Guillaud, "A pll-free grid-forming control with decoupled functionalities for high-power transmission system applications," *IEEE access*, vol. 8, pp. 197 363–197 378, 2020.

[89] M. Tozak, S. Taskin, I. Sengor, and B. P. Hayes, "Modelling and control of grid forming converters: A systematic review," *IEEE Access*, 2024.

[90] F. G. Puricelli and J. Beerten, "Bipolar vsc-hvdc links with grid-forming converters–dynamic performance and small-signal stability assessment," 2025.

[91] E. Rokrok, "Grid-forming control strategies of power electronic converters in transmission grids: Application to hvdc link," Ph.D. dissertation, Centrale Lille Institut, 2022.

[92] H. energy. "Half bridge mmc. "[Online]. Available: `https://www.hitachienergy.com/ch/it/products-and-solutions/semiconductors/semis-models/semis10`. (accessed: 10.02.2026).

[93] L. Shi, G. P. Adam, R. Li, and L. Xu, "Enhanced control of offshore wind farms connected to mtdc network using partially selective dc fault protection," *IEEE Journal of Emerging and Selected Topics in Power Electronics*, vol. 9, no. 3, pp. 2926–2935, 2020.

[94] X. Liu, P. Judge, G. Chaffey, W. Leterme, and D. Van Hertem, "Impact of current limiter implementation in mmc control on ac fault-ride-through and system distance protection," in *2024 Energy Conversion Congress Expo Europe (ECCE Europe)*, 2024, pp. 1–7. DOI: `10.1109/ECCEEurope62508.2024.10752070`.

[95] T. Qoria, F. Gruson, F. Colas, G. Denis, T. Prevost, and X. Guillaud, "Critical clearing time determination and enhancement of grid-forming converters embedding virtual impedance as current limitation algorithm," *IEEE Journal of Emerging and Selected Topics in Power Electronics*, vol. 8, no. 2, pp. 1050–1061, 2019.

[96] T. Qoria, F. Gruson, F. Colas, X. Kestelyn, and X. Guillaud, "Current limiting algorithms and transient stability analysis of grid-forming vscs," *Electric Power Systems Research*, vol. 189, p. 106 726, 2020.

[97] K. Friedrich, "Modern hvdc plus application of vsc in modular multilevel converter topology," in *2010 IEEE International Symposium on Industrial Electronics*, IEEE, 2010, pp. 3807–3810.

[98] L. Yang, Y. Xu, Q. Yu, Y. Zhou, and M. Zhu, "Study on characteristics and application of bypass-protected thyristor in vsc valve," in *2022 Annual Meeting of CSEE Study Committee of HVDC and Power Electronics (HVDC 2022)*, IET, vol. 2022, 2022, pp. 72–77.

[99] Q. Xiao, Y. Jin, H. Jia, Y. Tang, A. F. Cupertino, Y. Mu, R. Teodorescu, F. Blaabjerg, and J. Pou, "Review of fault diagnosis and fault-tolerant control methods of the modular multilevel converter under submodule failure," *IEEE Transactions on Power Electronics*, vol. 38, no. 10, pp. 12 059–12 077, 2023.

[100] W. Leterme and D. Van Hertem, "Classification of fault clearing strategies for hvdc grids," in *CIGRE, Date: 2015/05/27-2015/05/28, Location: Lund*, 2015.

[101] G. Dantas de Freitas et al., "Développement d'une méthodologie de comparaison des stratégies de protection pour les reseaux dc," Ph.D. dissertation, Université Grenoble Alpes (ComUE), 2019.

[102] InterOPERA, "Functional requirements for hvdc grid systems and subsystems," *Deliverable D2.1*, 2025.

[103] B. Jacobson, "Vsc-hvdc transmission with cascaded two-level converters," in *Cigre Conference, Paris, France, 2010*, 2010.

[104] A. Zama, A. Bertinato, P. Torwelle, and et.al., "North sea wind power hub feasibility study: Methodology for protection design (part ii)," in *2022 International Conference on Renewable Energies and Smart Technologies (REST)*, IEEE, vol. 1, 2022, pp. 1–5.

[105] T. CIGRE, "683; technical requirements and specifications of state-of-the-art hvdc switching equipment," *Joined WG A3/B4.34*, 2017.

[106] T. CIGRE, "604; guide for the development of models for hvdc converters in a hvdc grid," *WG B4.57*, 2014.

[107] R. Li and L. Xu, "Review of dc fault protection for hvdc grids," *Wiley Interdisciplinary Reviews: Energy and Environment*, vol. 7, no. 2, e278, 2018.

[108] M. Ahmad, M. Shafiullah, M. Y. Worku, M. S. Alam, and M. Khalid, "An overview of vsc-hvdc systems and challenges to harvest wind energy potential considering south asian region as a case study," *International Journal of Energy Research*, vol. 2025, no. 1, p. 8 644 219, 2025.

[109] PROMOTioN, "Deliverable 10.7: Full test setup and documentation," *Document on Test Result Analysis*, 2017.

[110] PROMOTioN, "Deliverable 4.2: Broad comparison of fault clearing strategies for dc grids. progress on meshed hvdc offshore transmission networks," *Deliverable 4.2*, 2017.

[111] E. Union. "Promotion - progress on meshed hvdc offshore transmission networks. "[Online]. Available: `https://www.promotion-offshore.net/`. (accessed: 28.08.2025).

[112] Siemens-Energy. "Direct current circuit breakers make power grids more robust. "[Online]. Available: `https://www.siemens-energy.com/global/en/home/stories/innovating-grid-technology.html`. (accessed: 26.04.2026).

[113] M. Electric. "Progress in hvdc grid protection. mitsubishi electric europe for the national hvdc centre. "[Online]. Available: `https://www.hvdccentre.com/wp-content/uploads/2019/07/Operators_Forum_2019_Subramanian_Kunjumuhammed.pdf`. (accessed: 26.04.2026).

[114] A. L. Courts, J. Vithayathil, N. Hingorani, J. Porter, J. Gorman, and C. Kimblin, "A new dc breaker used as metallic return transfer breaker," *IEEE Transactions on Power Apparatus and Systems*, no. 10, pp. 4112–4121, 1982.

[115] C. M. Franck, "Hvdc circuit breakers: A review identifying future research needs," *IEEE transactions on power delivery*, vol. 26, no. 2, pp. 998–1007, 2011.

[116] P. M. Anderson, *Power system protection*. John Wiley & Sons, 1999.

[117] G. Chaffey, "The impact of fault blocking converters on hvdc protection," Ph.D. dissertation, Imperial College London, 2017.

[118] D. Pinzan, S. Mart, and S. Raza, "Hvdc switching station technology review: An analysis for offshore mpi projects," in *2024 59th International Universities Power Engineering Conference (UPEC)*, IEEE, 2024, pp. 1–4.

[119] M. Panteli, P. Mancarella, D. N. Trakas, E. Kyriakides, and N. D. Hatziargyriou, "Metrics and quantification of operational and infrastructure resilience in power systems," *IEEE Transactions on Power Systems*, vol. 32, no. 6, pp. 4732–4742, 2017.

[120] S. H. A. Niaki, Z. Chen, B. Bak-Jensen, K. Sharifabadi, Z. Liu, and S. Hu, "On systematic dc fault-ride-through of multi-terminal mmc-hvdc grids," in *2021 56th International Universities Power Engineering Conference (UPEC)*, IEEE, 2021, pp. 1–6.

[121] J. Castellanos, F. Perez, A. Zama, A. Benchaib, and L. Xu, "Dc grid re-energization analysis during dc fault ride-through of bipolar mtdc systems with energy-based mmc control in grid-following," *Powering Net Zero conference, Glasgow*, 2025.

[122] M. Abedrabbo, M. Wang, P. Tielens, F. Z. Dejene, W. Leterme, J. Beerten, and D. Van Hertem, "Impact of dc grid contingencies on ac system stability," in *13th IET international conference on AC and DC power transmission (ACDC 2017)*, IET, 2017, p. 25.

[123] J. C. Gonzalez-Torres, V. Costan, G. Damm, A. Benchaib, A. Bertinato, S. Poullain, B. Luscan, and F. Lamnabhi-Lagarrigue, "Hvdc protection criteria for transient stability of ac systems with embedded hvdc links," *The Journal of Engineering*, vol. 2018, no. 15, pp. 956–960, 2018.

[124] P. Mitra, L. Sundaresh, and D. Ramasubramanian, "Stability of inverter-based resource (ibr) dominated systems with different types of local loads," *CIGRE Science & Engineering*, vol. 28, pp. 1–20, 2023.

[125] A. Saeed, M. Jensen, M. J. Reno, A. Bidram, and A. Zamani, "Utilities perspective on protection challenges with high ibr penetration," Pacific Gas and Electric, Tech. Rep., 2024.

[126] J. N. Sakamuri, Ö. Göksu, A. Bidadfar, O. Saborío-Romano, A. Jain, and N. A. Cutululis, "Black start by hvdc-connected offshore wind power plants," in *IECON 2019-45th Annual Conference of the IEEE Industrial Electronics Society*, IEEE, vol. 1, 2019, pp. 7045–7050.

[127] P. Torwelle, A. Bertinato, W. Grieshaber, Y. Yang, B. Raison, T. D. Le, and M. Petit, "Pre-energization concept for overhead lines in mtdc grids using dccb internal capacitor," *IEEE Transactions on Power Delivery*, vol. 37, no. 1, pp. 155–164, 2021.

[128] Q. Zhang, Z. Liu, and Z. Chen, "Restoration of a meshed hvdc grid with non-selective protection strategy," in *2019 IEEE Innovative Smart Grid Technologies-Asia (ISGT Asia)*, IEEE, 2019, pp. 2422–2427.

[129] M. Chandorkar, D. Divan, and R. Adapa, "Control of parallel connected inverters in standalone ac supply systems," *IEEE Transactions on Industry Applications*, vol. 29, no. 1, pp. 136–143, 1993. DOI: 10.1109/28.195899.

[130] W. Leterme, M. Abedrabbo, G. Chaffey, et al., "Impact of hvdc grid protection on dc cable transients," in *Proceedings Jicable-HVDC'21-International Symposium on HVDC cable systems*, JiCable, 2021.

[131] Y. Yu, Y. Guan, W. Kang, J. C. Vasquez, and J. M. Guerrero, "A generic inertial-response preserved active-damping control for grid-forming inverters emulating synchronous machines," *IEEE Transactions on Industrial Electronics*, 2024.

[132] R. Eriksson, J. Beerten, M. Ghandhari, and R. Belmans, "Optimizing dc voltage droop settings for ac/dc system interactions," *IEEE Transactions on Power Delivery*, vol. 29, no. 1, pp. 362–369, 2013.

[133] C. Larsson, "Hvdc a "firewall" against disturbances in high-voltage grids," *Sustainability ABB Newsletter*, vol. 3, pp. 42–46, 2005.

[134] F. J. Cifuentes Garcia, J. Kircheis, E. Avdiaj, and J. Beerten, "Mmc current controller design: Differences between uncompensated and compensated modulation," in *IET Conference Proceedings CP918*, IET, vol. 2025, 2025, pp. 290–294.

[135] B. Loyal Vivian, *Traveling Waves on Transmission Systems*. John Wiley Sons, 1993.

[136] HVDC-wise, "Protection concepts for ac/dc architectures," *Deliverable 3.3*, 2024.

[137] M. Abedrabbo, W. Leterme, and D. Van Hertem, "Systematic approach to hvdc circuit breaker sizing," *IEEE transactions on power delivery*, vol. 35, no. 1, pp. 288–300, 2019.

[138] W. Leterme, "Communication-less protection algorithms for meshed vsc hvdc cable grids," *Leuven: Doctoral Disertation, KU Leuven*, 2016.

[139] I. Hamdan and O. Noureldeen, "An overview of control method with various crowbar techniques of wind turbines during power system faults," *SVU-International Journal of Engineering Sciences and Applications*, vol. 2, no. 1, pp. 35–45, 2021.

[140] R. Gasch, J. Twele, P. Bade, W. Conrad, C. Heilmann, K. Kaiser, R. Kortenkamp, M. Kühn, W. Langreder, J. Liersch, et al., *Windkraftanlagen: Grundlagen, Entwurf, Planung und Betrieb*. Springer-Verlag, 2013.

[141] B. Jacobson, B. Jiang-Hafner, Y. Rey, P. Asplund, J. G, M. Gustafsson, and M. Bergkvist, "Hvdc with voltage source converters and extruded cables for up to±300 kv and 1000 mw," in *CIGRE, B4-105 Procedure*, 2006.

[142] A. M. Gross, K.-N. Malamaki, M. Barragán-Villarejo, G. C. Kryonidis, F. J. Matas-Díaz, S. I. Gkavanoudis, J. M. Mauricio, J. M. Maza-Ortega, and C. S. Demoulias, "Energy management in converter-interfaced renewable energy sources through ultracapacitors for provision of ancillary services," *Sustainable Energy, Grids and Networks*, vol. 32, p. 100 911, 2022.

[143] G. Franklin, J. D. Powell, and A. Emami-Naeini, "Feedback control of dynamic systems," in *Pearson*, American Society of Mechanical Engineers, vol. Global Edition, 2020, Eighth Edition.